THE UNIVERSITY OF CHICAGO

THEORETICAL AND COMPUTATIONAL METHODS FOR SLOW MOLECULAR

KINETIC PROCESSES

A DISSERTATION SUBMITTED TO

THE FACULTY OF THE DIVISION OF THE PHYSICAL SCIENCES

IN CANDIDACY FOR THE DEGREE OF

DOCTOR OF PHILOSOPHY

DEPARTMENT OF CHEMISTRY

BY

ZIWEI HE

CHICAGO, ILLINOIS

AUGUST 2022

To my family

TABLE OF CONTENTS

iv

LIST OF FIGURES

LIST OF TABLES

ACKNOWLEDGMENTS

This dissertation would not have been possible without the guidance and support from many people in my life. Firstly, I would like to thank my advisor, Professor Benoît Roux, for his mentorship throughout my graduate career. Without his encouragement, understanding nature, deep insight, as well as boundless enthusiasm for my projects, none of this work would have been possible. I would like to thank Fabian Paul for all of his helpful discussions and advice, as well as Rachael, Donghyuk, Matt, Angela, and Nabil who have been not only amazing group members to work with but also wonderful friends during my time here. I would also like to thank all other the Roux group members whom I had the privilege to work with: Jing, Younghoon, Trayder, Jonathan, Huan, Spencer, Chetan, Brian, Raj, Rong, Ying, Lydia, Yiling, Chris, Kevin, Aiman, Ahmed, Andrew, Ramon, and Flo.

I would like to thank my committee members Professor Aaron Dinner and Professor Suri Vaikuntanathan for their scientific discussions and for checking on my progress over the years. I also would like to thank Professor Chris Chipot for his collaboration on my projects and insightful discussions. Many thanks to Melinda and Vera in the Chemistry Department who make sure everything runs smoothly for the graduate students.

I would also like to thank the friends I have met during graduate school for making this experience funner and even more worth it: Yining, Kade, Memo, Becca, Erik S, and Erik T. I would like to thank my three my oldest friends, Miesha, Kristin, and Berky, whom I have known since middle school and who have always been very supportive and encouraging.

I would like to thank my family for their incredible love, encouragement, and support over the years. I am truly grateful to my parents, Chuan He and Lei Wang, who sparked my interest in science when I was a young child. I would like to thank my late dog, Jing Jing, for his unconditional love. Finally, I would like to thank my husband, Jaehyeok, for his encouragement, scientific discussions, and unconditional love throughout every step of the way.

ABSTRACT

Understanding the kinetic behavior of complex systems is crucial for the study of physical, chemical, and biological phenomena. While conventional methods such as molecular dynamics or enhanced sampling have been successful in characterizing the dynamics for a variety of systems, the computational cost to explore the configuration space is prohibitive and becomes infeasible for more complex systems with transition events that happen on longer timescales. Here, I will explore two powerful computational methodologies built upon statistical analysis and statistical mechanical frameworks to efficiently and accurately extract the kinetics, as well as other important observables for thermodynamics or transition pathways. First, I will construct Markov state models to study the binding and unbinding of a protein-protein complex. I will demonstrate the robustness of this methodology under various parameters and simulation conditions, and then I will propose an improved approach using a sensitivity analysis on the observables for the addition of biased simulations. Next, I will present a novel string method algorithm that allows for finding an optimal transition pathway on the free energy surface by taking into account the reactive probability. Drawing upon concepts from transition path sampling, the present framework aims to variationally minimize the steady state flux by way of the committor probability and notably can predict slow kinetic pathways for anisotropic systems, which are ubiquitous in biology and chemistry. Both of these proposed approaches allow the estimation of dynamic observables in a more efficient and more accurate manner.

CHAPTER 1

INTRODUCTION

The dynamics of complex molecular systems with long-lived states is a central area of study in computational chemistry and biophysics. Rare transitions between these so-called metastable states govern biological processes such as conformational changes [1], protein folding [2,3], and ligand binding [4]. At the very essence of the problem, we can consider a two-state kinetic model,

$$A \underset{k_{BA}}{\overset{k_{AB}}{\rightleftharpoons}} B \tag{1.1}$$

with reactant state A and product B. Of particular interest is the ability to accurately estimate the transitions rates k_{AB} and k_{BA}, the global relaxation time $\tau = (k_{AB} + k_{BA})^{-1}$, and equilibrium probabilities $p_A = k_{BA}/(k_{AB} + k_{BA})$ and $p_B = k_{AB}/(k_{AB} + k_{BA})$.

Traditional molecular dynamics simulations extracts dynamical information using an observational approach in which the state of a system is observed at some time t, then observed again at time $t + 1$, and so on. This purely brute-force approach has seen limited success in probing the kinetics and thermodynamics of relatively small molecules [5–7]. However, as we delve into more complex systems, we are presented with one of the major obstacles plaguing computational studies: the sampling problem. As the length and timescales of transition events increase with system complexity, on the order of milliseconds or longer for biological processes [8], the computational ability to adequately sample the full configurational space decreases. While enhanced sampling methods such as umbrella sampling [9], replica exchange molecular dynamics [10], and adaptive biasing force method [11,12], allow improved sampling of the state space by biasing simulations along a desired set of degrees of freedom, or collective variables (CV), the dynamical information becomes unreliable as a result of biasing the system away from equilibrium. This dissertation proposes theoretical frameworks and computational strategies to help extract kinetic information more accurately

and effectively.

There are two fundamental directions we may take to characterize the dynamics of slow molecular processes. The first direction considers the global timescales, which consists of forward and backward transitions that represent the natural kinetics of a system. This approach involves performing spectral decomposition analysis of a dynamical propagator, e.g., Markov state models. Alternatively, we may consider the net forward reactive flux J_{AB} that ascribes a unidirectional transition from state A to B in order to focus on the specific transition region of interest. The current Introduction chapter presents an overview of the existing theories and concepts crucial for the later chapters of the dissertation: Markov state models (MSMs), reactive flux, committor probability, and the string method. Chapter 2 describes the robustness of the MSM methodology under various input parameters and proposes a strategy to improve the accuracy and efficiency of MSMs when incorporating biased simulations. Chapter 3 presents a novel string method where the transition pathway is variationally optimized by minimizing a committor-correlation function. Chapter 4 concludes this dissertation and discusses future outlooks in these lines of works.

1.1   Markov State Models

An MSM can describe the full dynamics of a system of interest by constructing a network model that maps a system's state (e.g., a molecule's structure) to its free energy landscape, where these mappings can be used to predict transitions between states to provide an overall picture of the kinetics and thermodynamics [13–16]. MSMs have gained popularity in recent years since, compared to conventional molecular dynamics simulations, this powerful technique is less sensitive to undersampling by estimating long-time kinetic information from shorter simulations and allows a direct comparison of observables and statistical uncertainties with experimental results.

1.1.1 Continuous Space

Consider a state space Ω that consists of all possible dynamical conformations of a molecular system in equilibrium. We can denote $\mathbf{z}(t) \in \Omega$ as the state of the system at time t for a Markov process and assume ergodicity and detailed balance, i.e., is reversible. The probability density of the system at time t belonging to state $\mathbf{z}$ can be expressed as $\rho_t(\mathbf{z})$. We can then propagate the continuous Markovian dynamics from state $\mathbf{z}$ at time t to state $\mathbf{z}'$ at a later time $t + \tau$ as follows:

$$\rho_{t+\tau}(\mathbf{z}') = \int_\Omega d\mathbf{z} \; \mathcal{P}_\tau(\mathbf{z}, \mathbf{z}') \; \rho_t(\mathbf{z}), \tag{1.2}$$

where the propagator $\mathcal{P}_\tau$ satisfies the Chapman-Kolmogorov equation

$$\rho_{t+n\tau}(\mathbf{z}) = (\mathcal{P}_\tau)^n \; \rho_t(\mathbf{z}). \tag{1.3}$$

In other words, taking n number of steps of length τ (the lag time) with a Markov process is equivalent to a Markov process with a lag time of $n\tau$.

Spectral decomposition of the dynamical propagator is necessary for analyzing the dynamics of a Markovian system [17]. $\mathcal{P}_\tau$ consists of eigenfunctions $\psi_i^L(\mathbf{z})$ and $\psi_i^R(\mathbf{z})$, and the corresponding eigenvalues λ_i:

$$\lambda_i \psi_i^L(\mathbf{z}') = \int d\mathbf{z} \; \psi_i^L(\mathbf{z}) \; \mathcal{P}_\tau(\mathbf{z}, \mathbf{z}') \tag{1.4}$$

$$\lambda_i \psi_i^R(\mathbf{z}) = \int d\mathbf{z}' \; \mathcal{P}_\tau(\mathbf{z}, \mathbf{z}') \; \psi_i^R(\mathbf{z}'). \tag{1.5}$$

In the discrete state space (Section 1.1.2), ψ_i^L and ψ_i^R are approximated by the left and right eigenvectors, respectively, of the reversible transition probability matrix. λ_i is ordered from the slowest to fastest processes with $\lambda_1 = 1 > \lambda_2 \geq \lambda_3 \geq ... \geq \lambda_k$ for k degrees of freedom chosen with the CV space. $\lambda_1 = 1$ corresponds to the first left eigenvector ψ_1^L, which is the

invariant equilibrium distribution $\pi(\mathbf{z})$. The first few eigenvectors associated with the slowest degrees of freedom determine the metastable states of the system, where we can observe states with negative eigenvector components transition to states with positive eigenvector components, and the magnitude of the components is proportional to population of the state. In addition, the left and right eigenvectors are related by a factor of the equilibrium distribution:

$$\psi_i^L(\mathbf{z}) = \pi_i \psi_i^R(\mathbf{z}). \tag{1.6}$$

Finally, the relaxation times t_i can be computed as a function of the eigenvalues:

$$t_i = \frac{\tau}{\ln\lambda_i}. \tag{1.7}$$

To ensure Markovian behavior, an appropriate lag time τ must be chosen to satisfy the Chapman-Kolmogorov relation in Eq. 1.3.

1.1.2 Discrete Space

While we can formally describe the propagation of dynamics in a fully continuous space, in practice, the space space must be discretized from finite simulation data in order to make the construction and estimation of a Markov model computationally feasible. Discretization involves dividing the state space into sections, typically based on some geometric criteria such as the CVs [17]. For n discrete states of the partitioned space $S = \{S_1, ..., S_n\}$, we can define the MSM as a row-stochastic transition probability matrix $\mathbf{T}(\tau) \in \mathbb{R}^{n \times n}$ that describes the probability of transitioning from one state S_i at time t to another state S_j at a later time $t + \tau$. Fig. 1.1 illustrates a Markov process involving three discrete states and the transition probabilities between each pair of states.

In practice, $\mathbf{T}(\tau)$ is estimated from a maximum likelihood estimate of the number of
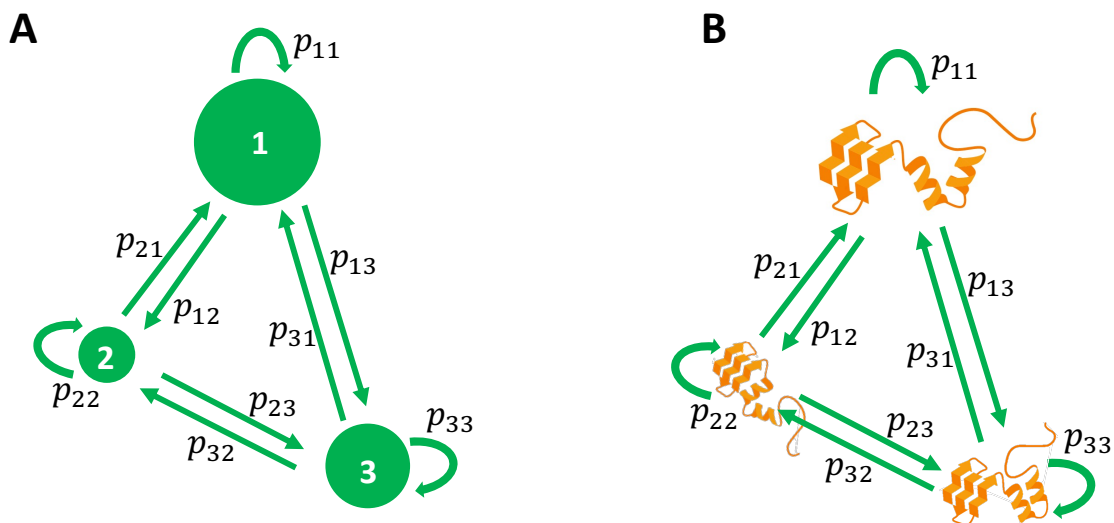
Figure 1.1: Schematic diagram of a Markov process. (A) MSM with three discrete states and their transition probabilities. (B) When applied to real systems of interest such as proteins, the discrete states become the different possible conformations a protein might adopt throughout a simulation.

counts on a transition count matrix between each pair of states i and j:

$$T_{ij}(\tau) = \arg \max \prod_{i,j=1}^{n} p_{ij}^{c_{ij}}, \tag{1.8}$$

where c_{ij} is number of transition counts from between states i and j, and p_{ij} is the transition probability.

1.2   Steady State Reactive Flux and Committor Probability

For higher dimensional systems that exhibit multiple long-lived states, one may wish to focus on specific transition regions of interest by analyzing dynamics from the perspective of a net steady-state reactive flux. This approach involves defining boundary states, for example reactant A and product B for a two-state system, and then investigating the A

5
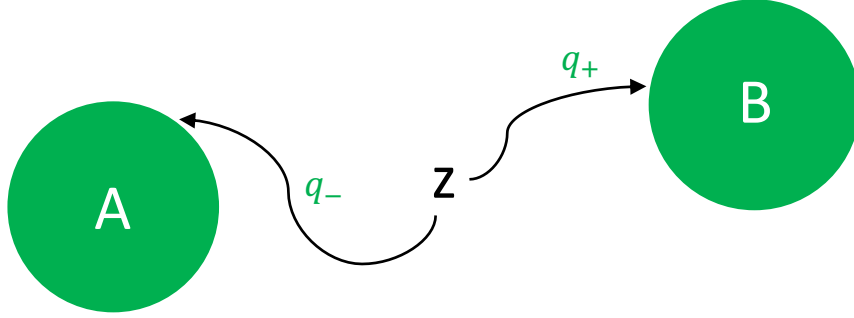
Figure 1.2: The committor gives the probability of reaching state A or B when starting from the state z. We can define a forward committor q_+ as the probability of reaching B before A, or a backward committor q_- as the probability of reaching A before B.

to B transition. This idea lies at the heart of transition path sampling (TPS) [18–22] and transition path theory (TPT) [23, 24] and has the advantage in circumventing issues from spectral decomposition, where some slow degrees of freedom are not directly correlated with the transition of interest.

In the TPT framework, the committor probability, first proposed by Onsager [25], is a critical element in estimating the reactive flux and drawing a reactive current path between metastable states A and B. In particular, we can think of the forward committor $q_+(\mathbf{z})$ as the probability of reaching state B before reaching state A when starting from $\mathbf{z}$ in the configuration space (Fig. 1.2)

$$
q_+(\mathbf{z}) = \begin{cases} 0, & \mathbf{z} \in A \\ f(\mathbf{z}), & \mathbf{z} \notin A \cup B \\ 1, & \mathbf{z} \in B \end{cases} , \tag{1.9}
$$

where we define $q_+(\mathbf{z})$ to be 0 if $\mathbf{z}$ happens to be in state A, 1 if $\mathbf{z}$ is in state B, and a value between 0 and 1 given by $f(\mathbf{z})$ in an intermediate region not belonging to A or B. Without loss of generality, for the rest of this dissertation, we will study the forward committor and denote it simply as $q(\mathbf{z})$. In practice, $f(\mathbf{z})$ can be computed by choosing $\mathbf{z}$ to be a set of CVs

along a 1-dimensional reaction coordinate space and defining well-guessed functions to best represent the system of study, for example by fitting an error function-like equation along $\mathbf{z}$ or assuming a linear combination of selected basis functions in the CV space [26–31]. For cases where we can project high-dimensional spaces onto 1-dimensional reaction coordinates, the committor probability then becomes

$$q(z) = \frac{\int_a^z e^{\ \beta W(z')} dz'}{\int_a^b e^{\ \beta W(z')} dz'},\tag{1.10}$$

where $\beta = 1/k_B T$, k_B is Boltzmann's constant, T is the temperature, $W(z)$ is the free energy profile along z, and a and b are the boundary cutoffs for states A and B, respectively.

Under steady-state conditions, the reactive flux can be expressed in terms of the committor [32]

$$\mathbf{J}_{AB}(\mathbf{z}) = \frac{1}{\tau} \int_{\mathbf{z} \in A} d\mathbf{z} \int_{\mathbf{z}' \in B} d\mathbf{z}' \ (q(\mathbf{z}) - q(\mathbf{z}')) \ \mathcal{P}_\tau(\mathbf{z}, \mathbf{z}') \rho_{eq}(\mathbf{z}),\tag{1.11}$$

and the rates can be estimated as

$$k_{AB} = \mathbf{J}_{AB}/p_A,\tag{1.12}$$

$$k_{BA} = \mathbf{J}_{AB}/p_B,\tag{1.13}$$

for populations p_A and p_B in states A and B, respectively.

1.3   The String Method

A natural consequence of analyzing the lines of reactive probability flux is to be able to find an optimal path that follows the dominant current between states A and B. The string method [33–35] attempts to find a reactive tube that contains the highest probability current connecting the two metastable states. In practice, the string method is performed in the

7
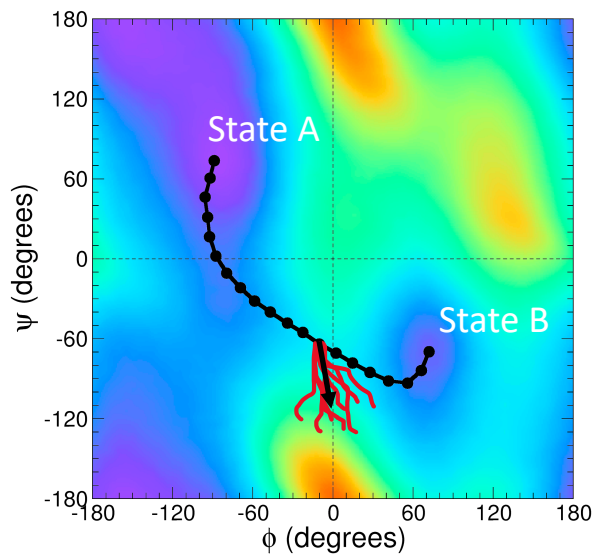
Figure 1.3: Illustration of the string method with swarms of trajectories. Many independent simulations (red curves) are launched from discrete positions, or images, along the string between states A and B. The image positions are updated following the mean drift vector (black arrow).

subspace of a set of CVs [36] and produces a curvilinear free energy pathway along the reaction coordinate $\mathbf{z}$ composed of the CVs.

The string method with swarms of trajectories was proposed by Roux and coworkers [37] as a computationally efficient approach for optimizing a reactive pathway. Fig. 1.3 illustrates this approach, where many short, unbiased trajectories are launched at various positions, or images, along an initial path. The PMF and string shown are adapted from Ref. [38]. The string is then iteratively evolved by updating the position of each image by the average drift of its trajectory swarm until converged. Given M discrete images $\{\mathbf{z}_1, \mathbf{z}_2, ..., \mathbf{z}_M\}$ along the string, we can compute the mean drifts as an average over noise for each of the ensemble swarm of trajectories

$$\Delta \mathbf{z} = \mathbf{z}(\tau) - \mathbf{z}(0) = \tau\beta\mathbf{DF} + \tau\boldsymbol{\nabla}\mathbf{D}, \tag{1.14}$$

8

where $\mathbf{D}$ is the diffusion tensor evaluated at $\mathbf{z}(0)$, and $\mathbf{F} = -\nabla W(\mathbf{z}(0))$ is the mean force. Then, the steady state flux can be related to the diffusive system [39] as follows

$$\mathbf{J}_{AB}(\mathbf{z}) = \int d\mathbf{z} \ \nabla q(\mathbf{z}) \ \mathbf{D} \ \rho_{eq}(\mathbf{z}) \ \nabla q(\mathbf{z}). \tag{1.15}$$

From this expression, we observe that the direction of the flux depends on both ∇q and $\mathbf{D}$. In Chapter 3 of the dissertation, we will compare the string method with swarms of trajectories and a novel formulation of the string method that benefits from following the direction of ∇q.

CHAPTER 2

MARKOV STATE MODEL TREATMENTS OF PROTEIN–PROTEIN ASSOCIATION USING COARSE-GRAINED SIMULATIONS

The material from this chapter is reproduced from Z. He, F. Paul, B. Roux, A critical perspective on Markov state model treatments of protein-protein association using coarse-grained simulations. *J. Chem. Phys.*, **154**, 084101 (2021), with the permission of AIP Publishing.

2.1   Introduction

One of the most important questions in biology is how living cells communicate and respond to the flow of information at the molecule level. To decipher the molecular basis of cellular communication, one must explain the specific interactions governing protein-protein recognition in terms of structure and dynamics [40–42]. While the protein-protein equilibrium binding affinity and specificity are certainly important, a characterization of the kinetic aspects of association and dissociation is perhaps of even greater significance to understand the time-course of biological processes [43]. In principle, atomic-level information is essential to study protein complexes in terms of structure and dynamics. However, the long timescales and high dimensionality present outstanding computational challenges in computer simulations of rare events [44].

Markov state models (MSMs) provide a powerful framework for characterizing the kinetics of complex molecular systems [14, 15, 17, 45–47]. MSMs are discrete state and discrete time stochastic master equation models. Building an MSM involves defining a set of discrete microstates within a subspace of collective variables (features), and then estimating the hopping transition probabilities between such states at a fixed lag-time interval from the

information generated by detailed dynamical simulations [48]. Assuming that the resulting MSM thus constructed is indeed representative of the system of interest, the framework can then be used as a generator to predict any equilibrium or long-time kinetic properties at low computational cost.

The overall accuracy and usefulness of MSM analysis is typically burdened by two opposing problems. The first problem arise from the need to achieve Markovian dynamics. An MSM must satisfy ergodicity, but often important transitions are not sampled due to computational limits and are missing in the MSM. Also, the evolution of the system monitored at a given lag-time interval exhibits non-Markovian correlated dynamics when the trajectories are mapped onto a set of coarsely defined microstates. Immediate remedies to reduce such non-Markovian effects are to choose a longer lag-time or refine the definition of the microstates by using a featurization space of higher dimensionality with more collective variables. However, as the lag-time and the number of microstates are increased, the finite amount of information from the detailed simulations becomes rapidly insufficient to determine the larger number of transition probabilities accurately. Thus, as we try to address the first problem–achieving Markovian dynamics, the statistical accuracy of the MSM breaks down, causing the second problem.

Different strategies have been devised to mitigate these two contradictory problems by trying to efficiently identify the smallest number of most relevant features expected to display the least amount of non-Markovian dynamics. One such method is the time-lagged independent component analysis (TICA) [49, 50] which was proposed to process high-dimensional data without the loss of kinetically relevant information. Unfortunately, the optimal selection of input features and the process of discretization to define the microstates are often unclear, and there are various different ways one can construct an MSM for the same system [15, 17]. Furthermore, the accuracy of the MSM relies quite heavily on having a well-sampled configurational space. Despite the recent advances in computational modeling and achievements

in MSMs applied to large biomolecular systems [51, 52], the construction of robust and well converged MSM from full atomistic simulations still remains a highly demanding feat. By itself, the MSM framework does not directly help improve the exploration of rare events and (high free energy) configurations. Sampling issues must be tackled indirectly through sensitivity analysis and adaptive strategies. Different methodological aspects may be brought to bear on the problem to ensure an optimal outcome, including featurization, enhanced sampling techniques [52, 53], and sensitivity analysis [54–57].

Our principal goal is to test the robustness and reliability of the methodology, by exploring different strategies for the efficient construction of MSMs. To maintain complete control over the convergence of the present analysis and circumvent the statistical uncertainties caused by sampling issues, a simplified coarse-grained (CG) model of the barnase-barstar protein complex was used for all the simulations. Several MSMs were built from different sets of features as well as combinations of biased and unbiased simulations to understand how these inputs may affect the resultant thermodynamic and kinetic observables. We then re-examine the transition-based reweighting analysis method (TRAM) [53]. Using an approach similar to the eigenvalue-based sampling [58–60], we propose a sensitivity analysis [54–57] that can identify regions of undersampling and efficiently add in biased simulations only where necessary.

2.2   Methods

2.2.1   Coarse-Grained System

The barnase-barstar system is taken from the crystal structure 1BRS Protein Data Base ID [61]. Chain B is selected for barnase and chain D for barstar. The CG representation is constructed by mapping each amino acid residue as a single bead with its mass and position corresponding to the Cα. We designed our CG potential as a Gō-like model [62, 63],
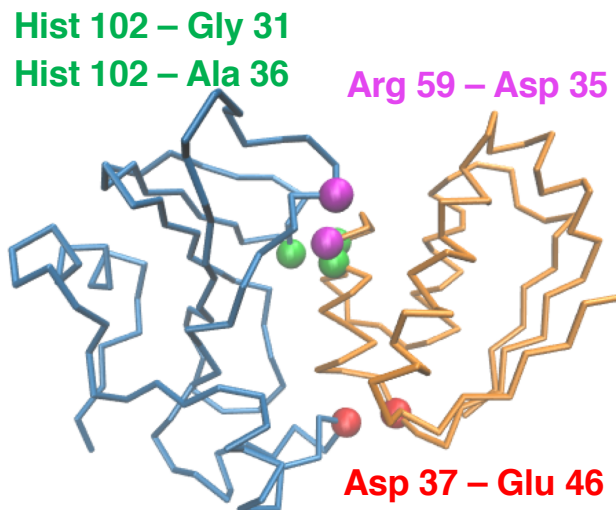
Figure 2.1: The barnase-barstar protein complex with one coarse-grained (CG) particle per residue. In order to model the interactions in the simplified protein complex, four Lennard-Jones potentials between key non-bonded particles, corresponding to the important residues involved in binding, were chosen to simulate association in the correct native bound state. The key pairwise residues are depicted as CG beads.

using attractive potentials to represent the pairwise contacts of the native complex. Four Lennard-Jones 6-12 potentials with a well depth of 3.0 kcal/mol were introduced between the non-bonded beads of barnase and barstar (Fig. 2.1) to accurately simulate the association in the native bound state. The four Gō-like contact pairs, listed in Table 2.1, were selected due to their importance for binding as reported in literature [64–66].

Table 2.1: Gō-like contact pairs chosen from key amino acid residue pairs on barnase and barstar with minimum distances $R_{\min}$.

Barnase	Barstar	$R_{\min}$ (Å)
Asp 37	Glu 46	4.96
Arg 59	Asp 35	5.65
Hist 102	Gly 31	4.82
Hist 102	Ala 36	5.83

In addition, root-mean-square deviation (RMSD) restraints were applied to each protein to maintain their folded conformation. The complex was enclosed in a finite spherical volume with a radius of 73.46 Å using a flat-bottom potential, yielding an effective concentration of

Table 2.2: MSMs constructed from different featurization and simulation methods.

Model Name	Features	Simulation	Microstates
MSM-6D	4 TICA components from long-lived pairwise contacts, RMSD with respect to the native bound state, COM distances	MD	550
TRAM-6D	4 TICA components from long-lived pairwise contacts, RMSD with respect to the native bound state, COM distances	MD + US	100
TRAM-1D	COM distances	MD + US	100
TRAM-1D-inv	Squared inverse COM distance	MD + US	100

Models were estimated at a lag time of 12 ns.

1 μM. The barnase was restrained at the origin in position and orientation, while barstar was allowed to freely diffuse in the cavity. Because the protein complex is invariant by translation and rotation, this does not affect the equilibrium features of the system. 25 independent, unbiased Langevin molecular dynamic (MD) simulations were performed at 300 K with a damping constant of 1 ps^{-1} and time step of 1 fs, for a total aggregate simulation time of 25 μs. Umbrella sampling (US) simulations were carried out using harmonic biasing potentials chosen along the distance between the center-of-mass (COM) of barnase and the COM of barstar, with spring constants of 1 kcal/mol. 70 windows were assigned along the reaction coordinate from 4 to 73 Å at 1 Å intervals, yielding 200 ns of simulation time per window at a 5 fs time step. All simulations were performed using the NAMD program [67] with the CHARMM [68] force field parameter file to choose non-bonded pairs for implementing Gō contacts. The visualization program VMD [69] was used to render the barnase-barstar complex.

2.2.2 Markov State Model Construction

We construct four MSMs using different combinations of biased and unbiased trajectories and different choices in featurization. These selections account for the limitations MSMs often face due to (1) undersampling and (2) non-optimal selection of features due to the

many possible reaction pathways that arise from the simulation of huge biomolecules. We evaluate the performances of the MSMs by comparing them with the properties calculated from the raw trajectories of the MD and US simulations. The MSMs and their construction input parameters are summarized in Table 2.2. Detailed discussions of the models follow in Sec. 2.3.

MSM-6D is a traditional MSM built from unbiased MD trajectories using 6 features corresponding to the four slowest linear combinations of pairwise contacts computed from TICA, the minimum RMSD of the complex with respect to the native bound state, and the COM distances between the barnase protein and the barstar protein. We will treat MSM-6D as the reference MSM, since it is a traditionally constructed MSM using only unbiased simulations and has a relatively long aggregate simulation time of 25 μs with many observed association and dissociation events. TRAM-6D was built using the same approach as MSM-6D with the addition of biased US trajectories. TRAM-1D was generated using only the COM protein distances from the MD and US trajectories. Lastly, TRAM-1D-inv was build upon the squared inverse COM distances as features to consider an indirect reaction coordinate. Clustering was performed using k-means [70, 71], and the number of microstates was determined by the elbow method [72], which optimizes the minimization of the intra-cluster variance. The models were constructed with lag times of 12 ns. The MDTraj [73] software was used for trajectory analysis. The PyEMMA [74] software and a few functionalities of the msmtools package were used to construct the MSMs and perform several analyses. Figures were rendered using Matplotlib [75].

For MSM-6D and TRAM-6D, which rely on a larger set of features, a number of methods were employed to make the MSM construction feasible despite the large volume of data. Given the 110 residue beads on barnase and 89 on barstar, we would have to work with $110 \times 89 = 9790$ pairwise distances. In order to reduce the computational effort in such a high dimension, we considered only the pairwise distances that were deemed kinetically

relevant. Employing a similar strategy used by Plattner et al. with their hidden MSM built upon the full atomistic simulations of the barnase-barstar complex [51], we obtained 817 long-lived pairwise contacts that were within a distance of 12 Å and bound for at least 1 ns.

TICA was utilized to further reduce dimensionality. TICA is a powerful dimensionality reduction algorithm that extracts the most kinetically-relevant linear combinations of the long-lived pairwise contact distances. Briefly, TICA first computes the time-lagged covariance matrices $\mathbf{C}(\tau)$ from a given set of mean-free input data $r(t)$ (e.g., the long-lived pairwise distances) at time t with elements

$$c_{ij}(\tau) = \langle r_i(t)r_j(t+\tau)\rangle \tag{2.1}$$

$$= \frac{1}{N-\tau-1}\sum_{t=1}^{N-\tau} r_i(t)r_j(t+\tau), \tag{2.2}$$

where τ is the lag time and N is the size of the data. Then, solving for the generalized eigenvalue problem gives

$$\mathbf{C}(\tau)\mathbf{U} = \mathbf{C}(0)\mathbf{U}\mathbf{\Lambda}, \tag{2.3}$$

where $\mathbf{U}$ is an eigenvector matrix consisting of time-lagged independent components (ICs) as the columns, and $\mathbf{\Lambda}$ is a diagonal eigenvalue matrix. The data set $\mathbf{r}(t)$ is then projected onto the TICA space that maximizes the autocorrelation of the transformed coordinates

$$\mathbf{z}^\top(t) = \mathbf{r}^\top(t)\mathbf{U}. \tag{2.4}$$

We reduced down to the desired number of dimensions by choosing a subspace of only the first few columns of $\mathbf{U}$. A more detailed discussion of TICA can be found in References [49, 50].

For this study, we kept the four slowest ICs from TICA that had noticeably slower timescales compared to the rest of the ICs, as demonstrated in Fig. 2.2. Then, the RMSD

16

and COM distances were added as additional features to include physical observables that are more intuitively understandable. Clustering was performed on this six-dimensional feature
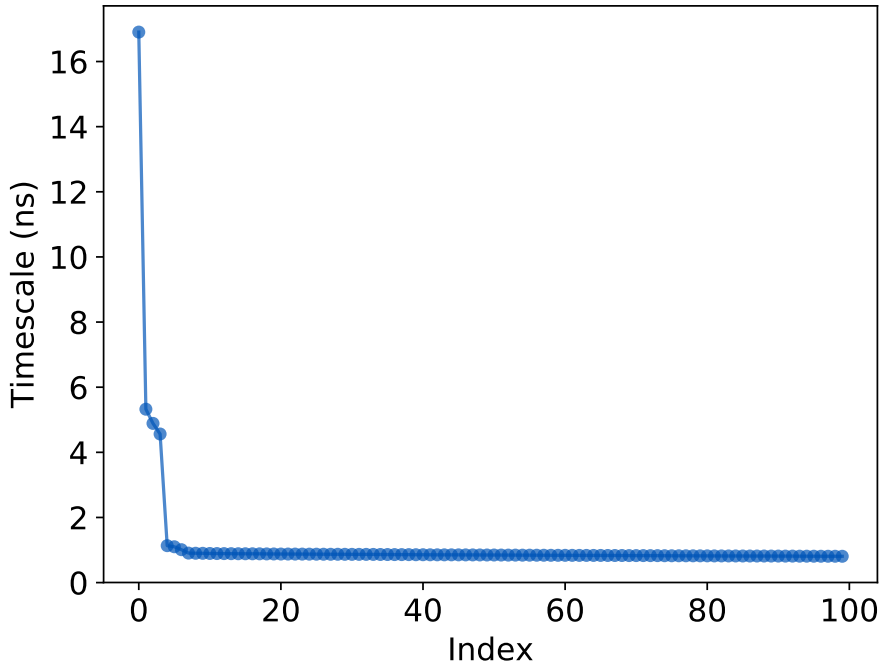
Figure 2.2: The timescales of TICA. Ther first four dimensions with noticeably slower timescales were used as part of the set of features for MSM and TRAM construction.

space. This feature selection is similar to the hidden MSM of the all-atom barnase-barstar reported by Plattner et al. [51]. Hence, we can avoid any uncertainty underlying the number of dimensions during the MSM construction by employing a similar feature selection for the CG descriptions (MSM-6D and TRAM-6D) that is based on the atomistic MSM. We note that selecting the six features and other MSM hyperparameters for MSM-6D and TRAM-6D manually was straightforward for the present CG complex. However, for more complicated systems, the Generalized Matrix Rayleigh Quotient (GMRQ) [76–79] and the variational approach for Markov processes (VAMP) score [80, 81] would provide useful tools for systematically determining the optimal features and MSM hyperparameters.

2.2.3 Determination of the Optimal Cutoff Distance

For the purpose of comparing the kinetic rates and binding constants of the MSMs with those calculated from the raw analyses of the trajectories, we first have to choose a cutoff distance that clearly delineates between the bound and unbound states in the simulations. For r_{cut} values that are much smaller or larger than an optimal r_{cut}, there will be faster fluctuations and numerous rapid recrossings on a short timescale. We want to determine the r_{cut} for which the influence of such rapid fluctuations is minimized. Here, for r_{cut} in the range of 25 to 35 Å along the COM distance, an indicator state function $h(t)$ was assigned to equal to 0 when unbound and 1 when bound

$$
h(t) = \begin{cases} 0, & \text{if unbound,} \\[2mm] 1, & \text{if bound.} \end{cases} \tag{2.5}
$$

Then, the time-correlation function, averaged from the aggregate trajectories, was calculated for each r_{cut} value

$$
C = \langle h(0)h(\tau)\rangle, \tag{2.6}
$$

where τ is the lag time. Normalizing the time-correlation function, we can rewrite Eq. (2.6) as

$$
C = \frac{\sum_{i=1}^{N-\tau}(h_i - \tilde{h})(h_{i+\tau} - \tilde{h})}{\sum_{i=1}^{N}(h_i - \tilde{h})^2}, \tag{2.7}
$$

where N is the total simulation time length, and $\tilde{h}$ is the averaged data. In order to determine the relaxation lag time, the correlations were fitted (Fig. 2.3), using biexponential decaying
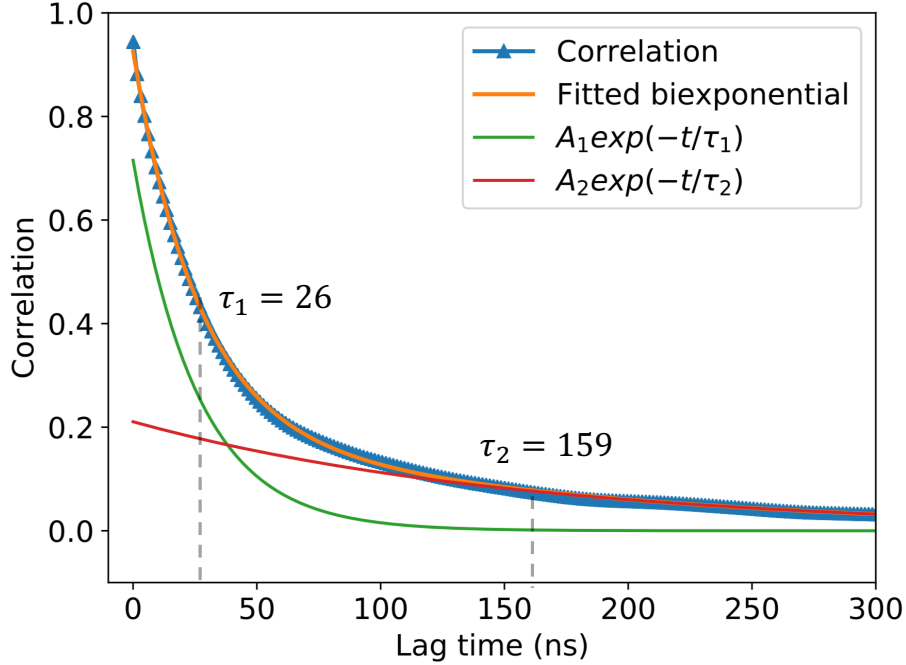
Figure 2.3: Autocorrelation of the bound state indicator (blue triangles) for $r_{\text{cut}} = 29$ Å. A biexponential decay curve was fitted (orange) to the autocorrelation using two exponential functions $A_1 e^{-t/\tau_1}$ and $A_2 e^{-t/\tau_2}$ (red and green, respectively), where $A_1 = 0.715, \tau_1 = 26.1$ ns, $A_2 = 0.211$, and $\tau_2 = 159.4$ ns.

functions of the form

$$A(t) = A_1 e^{-t/\tau_1} + A_2 e^{-t/\tau_2}. \tag{2.8}$$

Upon fitting, the r_{cut} values were adjusted until the relaxation time in the correlation function was the longest (i.e. when the biexponential τ's were the longest). As demonstrated in Fig. 2.4, the optimal value of r_{cut} yielding the largest relaxation times is 29 Å, although we note that the results are fairly similar for a COM distance varying between 25 and 35 Å. Appendix Table 2.4 lists the r_{cut} values and the corresponding biexponential lag times, τ_1

19
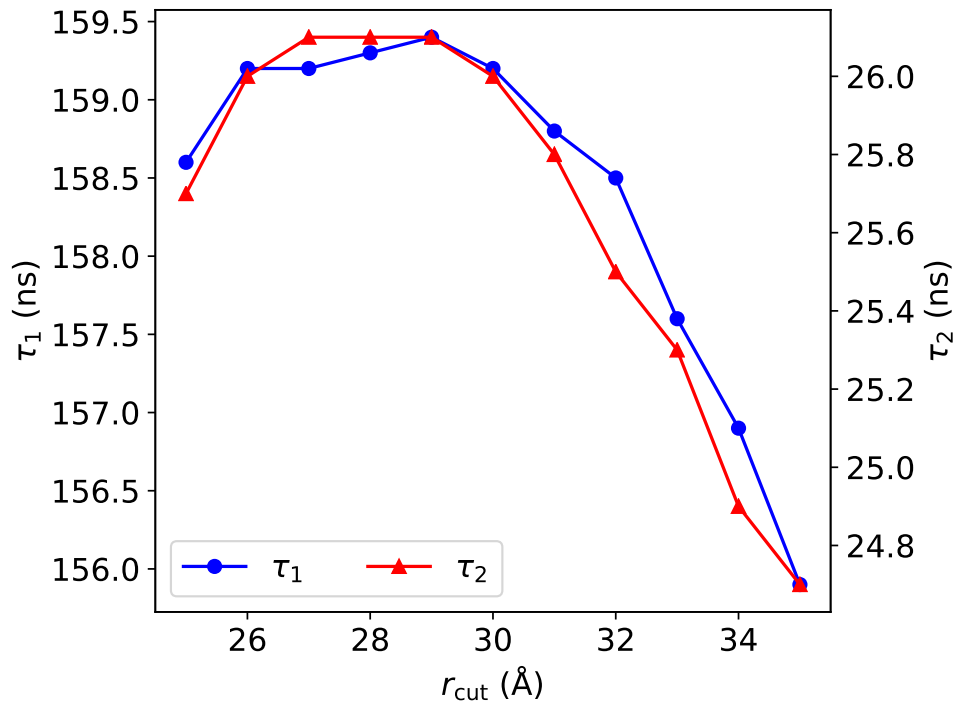
Figure 2.4: Relaxation times as a function of r_{cut}. The lag times τ_1 and τ_2 peak at an r_{cut} of 29 Å, and we choose this r_{cut} value as the bound state cutoff to minimize any statistical fluctuations in our trajectory analyses.

and τ_2. Accordingly, we define the bound and unbound states as

$$
\text{state} =
\begin{cases}
\text{bound}, & \text{if } r \leq r_{cut}, \\[2mm]
\text{unbound}, & \text{if } r > r_{cut},
\end{cases}
\tag{2.9}
$$

where a bound state is defined as having a COM distance between barnase and barstar that is within 29 Å and an unbound state is defined as having a COM distance greater than 29 Å. Since the complex has been reported to go through a loosely bound state before reaching the final native bound state [51,82], a τ_1 of 26 ns can be thought of as the timescale to achieve the loosely bound state while a τ_2 of 159 ns can be taken as the average lifetime of the fully bound state. This r_{cut} value was employed for analysis of the MD and US trajectories in Table 2.3 of Section 2.3.

20

Table 2.3: Equilibrium binding constants and kinetic rates obtained from the five different MSMs.

Model name	$K_{\mathrm{eq}}^{\mathrm{PMF}}$ $(\times 10^5 \mathrm{\mathring{A}}^3)$	$K_{\mathrm{eq}}^{\mathrm{Pbound}}$ $(\times 10^5 \mathrm{\mathring{A}}^3)$	k_{on} $(\times 10^{13} \mathrm{\mathring{A}}^3 \mathrm{s}^{-1})$	k_{off} $(\times 10^7 \mathrm{s}^{-1})$
MD	9.24	8.86	2.67	2.98
US	9.04	...	...	...
MSM-6D	...	8.83 ± 0.17	2.31 ± 0.04	2.70 ± 0.03
TRAM-6D	...	8.72 ± 0.17	2.37 ± 0.04	2.75 ± 0.03
MSM-1D	...	8.72 ± 0.20	2.50 ± 0.03	2.86 ± 0.04
TRAM-1D	...	8.67 ± 0.16	2.44 ± 0.03	2.89 ± 0.04
TRAM-1D-inv	...	8.66 ± 0.20	2.43 ± 0.04	2.88 ± 0.04

2.2.4 Calculation of Thermodynamic and Kinetic Properties from MSMs

In order to understand protein-protein interactions by means of MSMs, we must be able to calculate thermodynamic and kinetic quantities from them. The equilibrium binding constant and the ΔG_{b} of binding, can be obtained from the stationary distribution, π, which gives the equilibrium probability distribution by the first left eigenvector from the MSM transition matrix, $\mathbf{T}$, as follows:

$$\pi = \pi \, \mathbf{T}. \tag{2.10}$$

We can then calculate the binding constant from the ratio of the probabilities of the bound to unbound states given by π,

$$K_{\mathrm{eq}} C = \frac{P_{\mathrm{bound}}}{P_{\mathrm{unbound}}}, \tag{2.11}$$

where $C = V^{-1}$ is the concentration, and V is the volume corresponding to the "bulk" region,

$$V = \frac{4}{3} \pi (r_{\mathrm{cavity}}^3 - r_{\mathrm{cut}}^3). \tag{2.12}$$

An r_{cavity} equal to 73.46 Å is the radius of the spherical cavity used to enclose the protein complex during simulation, and r_{cut} equal to 29 Å represents the cutoff distance used to delineate between the bound and unbound states. The volume of the bulk region yields a concentration of 1 μM. The binding free energy can be defined as

$$\Delta G_{\text{b}} := -k_{\text{B}}T \ \ln\left(\frac{P_{\text{bound}}}{P_{\text{unbound}}}\right). \tag{2.13}$$

The binding constant can also be calculated by integrating over the radial potential of mean force (PMF),

$$K_{\text{eq}} = \int_0^{r_{\text{cut}}} dr \ 4\pi r^2 \, e^{-\beta W(r)}, \tag{2.14}$$

where $\beta = 1/k_{\text{B}}T$, $k_{\text{B}}T = 0.596$ kcal/mol. Here, it is assumed that the PMF has been offset to have $\lim_{r \to \infty} W(r) = 0$.

Perron-cluster cluster analysis (PCCA) is a method that clusters eigenvectors in order to define metastable, or long-lived, states in an MSM [83,84]. We performed the PCCA++ method implemented in PyEMMA to define two metastable states, the bound state and the unbound state, in order to obtain the mean first passage times (MFPT) between these two states. Kinetic rates of association and dissociation can be calculated accordingly,

$$k_{\text{on}} = \frac{1}{\text{MFPT}_{\text{on}} \, C}, \tag{2.15}$$

$$k_{\text{off}} = \frac{1}{\text{MFPT}_{\text{off}}}. \tag{2.16}$$

2.3   Results

In this section, we now discuss the results obtained from the four MSMs described in Table 2.2. Fig. 2.5 compares the free energy profiles of a one-dimensional MSM (25 μs MD simula-
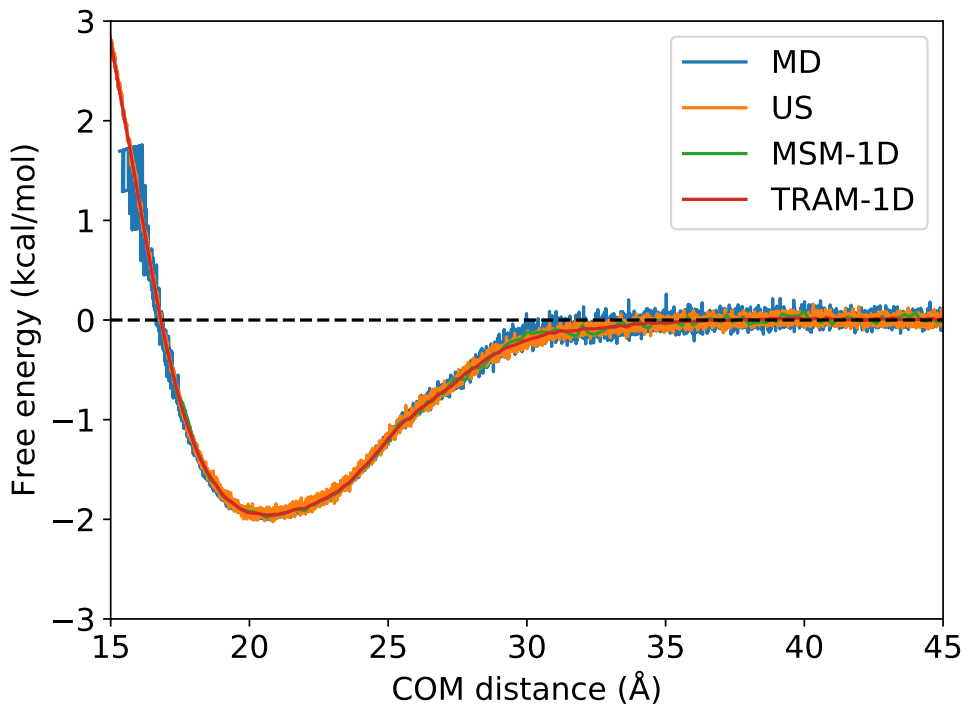
Figure 2.5: Free energy profiles of the raw trajectories, MSM, and TRAM. The free energy profiles obtained from a raw MD trajectory of 25 μs aggregate simulation time (blue), the PMF of a US simulation of 200 ns per window (orange), a one-dimensional traditional MSM from COM distance feature and and 25 μs aggregate simulation time (green), and TRAM-1D (red) show near identical agreement, proving the robustness of the MSM methodology even when using only one feature.

tion) and TRAM-1D (25 μs MD simulation and 200 ns per window US simulation) with the PMFs from the raw MD and US trajectories. The free energies, MFPTs, and resultant binding constants and rates are within agreement, indicating that using just the one-dimensional COM distance can adequately capture the binding process of this protein complex. Table 2.3 summarizes the thermodynamic and kinetic properties calculated from the MSMs. The kinetic rates and binding constants were calculated from the MSMs and demonstrate that the MSM methodology is robust and consistent. Notably, even stripping the features down to only one dimension seems to produce MSMs that can recapitulate the thermodynamics and kinetics.

Calculations were also performed for the raw unbiased (MD) and biased (US) simulations

for comparison with the MSMs. The binding constants obtained by integrating the free energy profiles from 0 to r_{cut} (Eq. (2.14)) are listed under $K_{\text{eq}}^{\text{PMF}}$, and the binding constants obtained by calculating the probability ratios of bound and unbound states (Eq. (2.11)) are listed under $K_{\text{eq}}^{\text{Pbound}}$. The association and dissociation rate constants are listed under k_{on} and k_{off}, respectively. We will describe each of the MSMs in more detail in Secs 2.3.1 and 2.3.2.

2.3.1   High-Dimensional Markov State Models

We start off by examining MSM-6D, which is a conventional MSM using a set of high-dimensional features from unbiased trajectories. As illustrated in Fig. 2.6, MSM-6D can clearly distinguish the bound and unbound configurations. The free energy landscape along the two slowest TICA components, or independent components (IC) 1 and 2, reveal a free energy well corresponding to the bound configurations and another well for completely dissociated structures. The 550 centroids in Fig. 2.6 are colored based on the COM distance between barnase and barstar.

The first IC corresponding to the slowest degree of freedom represents the binding pathway along the COM distance, while the second, third, and fourth ICs can be interpreted as the orientational changes during association and dissociation. Although the free energy landscape along ICs 2, 3, and 4 do not change as drastically as that for IC 1, these slow modes are still important for association. Since the rate-limiting step involves a partially bonded conformation where some of the pairwise contacts are formed while others are not, the orientation of the proteins may change even though the COM distance between them remains the same. In other words, by including the four ICs from TICA, our six-dimensional MSM effectively encodes both translational and orientational contributions in the course of protein association. The full relationship among the four ICs is depicted in Fig. 2.17 of the Appendix.
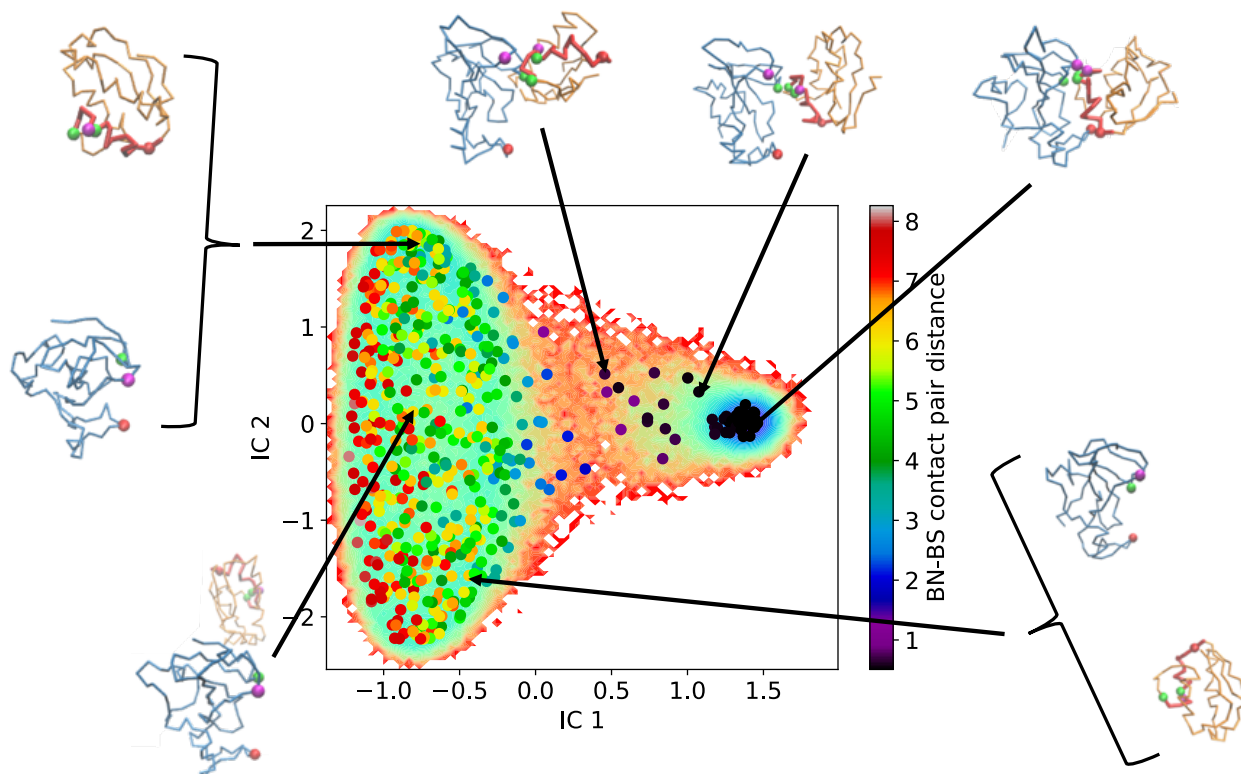
Figure 2.6: Representative structures of the MSM-6D microstates. The centroids from k-means clustering are colored by the COM distance of the complex and plotted on top of the free energy landscape along the two slowest modes of TICA. Representative structures are taken from each of the centroids to give a better idea of the microstate assignment. Starting from the the top right and going counterclockwise, we have clusters representing the bound state, an intermediate state where one LJ pair is separated, an intermediate state where two LJ pairs are separated, and three dissociated states.

The MSM-6D timescales plotted in Fig. 2.7 indicate two much slower timescales at 17 ns and 19 ns and another relatively slower timescale at 10 ns, suggesting that there should be at least three or four important metastable states. Then, carrying out PCCA with four states, as illustrated in Fig. 2.8, we generated one metastable state where the complex is primarily in the bound state, a metastable state consisting of intermediate states and loosely bound states, and two metastable states with where the complex is completely dissociated. The dissociated conformations in metastable states 3 and 4 are distinguished by the orientational position of barstar with respect to barnase. It should be noted that the PCCA metastable assignment uses fuzzy clustering. For example, the metastable state 1 corresponding to the bound state
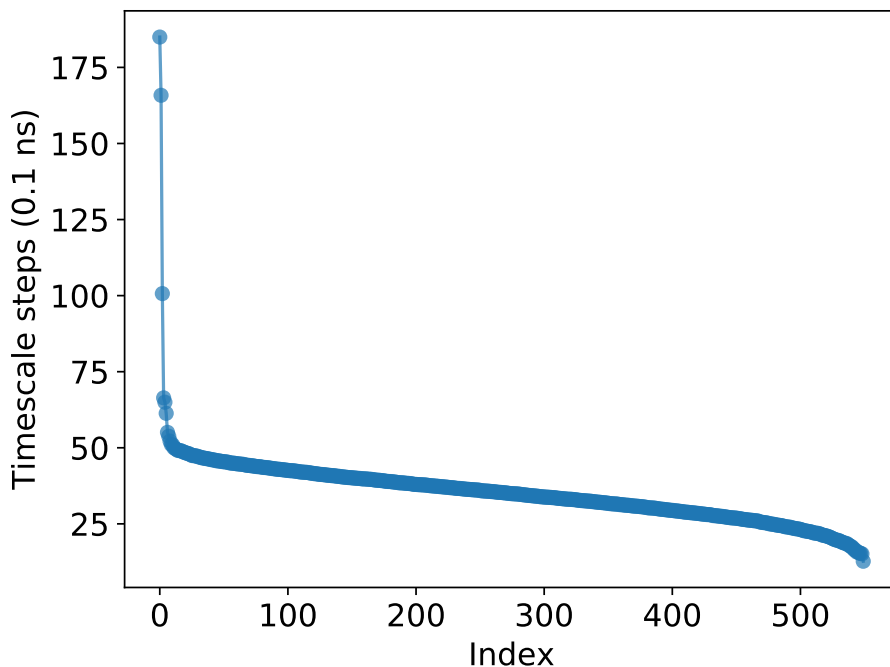
Figure 2.7: Timescales of MSM-6D with 550 microstates. There are two timescales lasting longer than 15 ns and one lasting around 10 ns, indicating that there should be three or more long-lived, or metastable, states.

still contains a few structures that clearly correspond to dissociated states. We can perform a crisper assignment by manually selecting the set of states, which is fairly straightforward, but we choose PCCA here because it is more generally applicable for systems with reaction coordinates that are not so readily straightforward. For the purpose of obtaining the MFPTs of the bound and unbound states in order to calculate the kinetic rates listed in Table 2.3, we generated a two-state PCCA.

2.3.2 Markov State Models from Biased Simulations

TRAM allows the estimation of MSMs by stitching together the different thermodynamic and kinetic information from the biased and unbiased simulations [84]. As we ultimately want to take advantage of both biased and unbiased data, in the following subsections, we examine

26
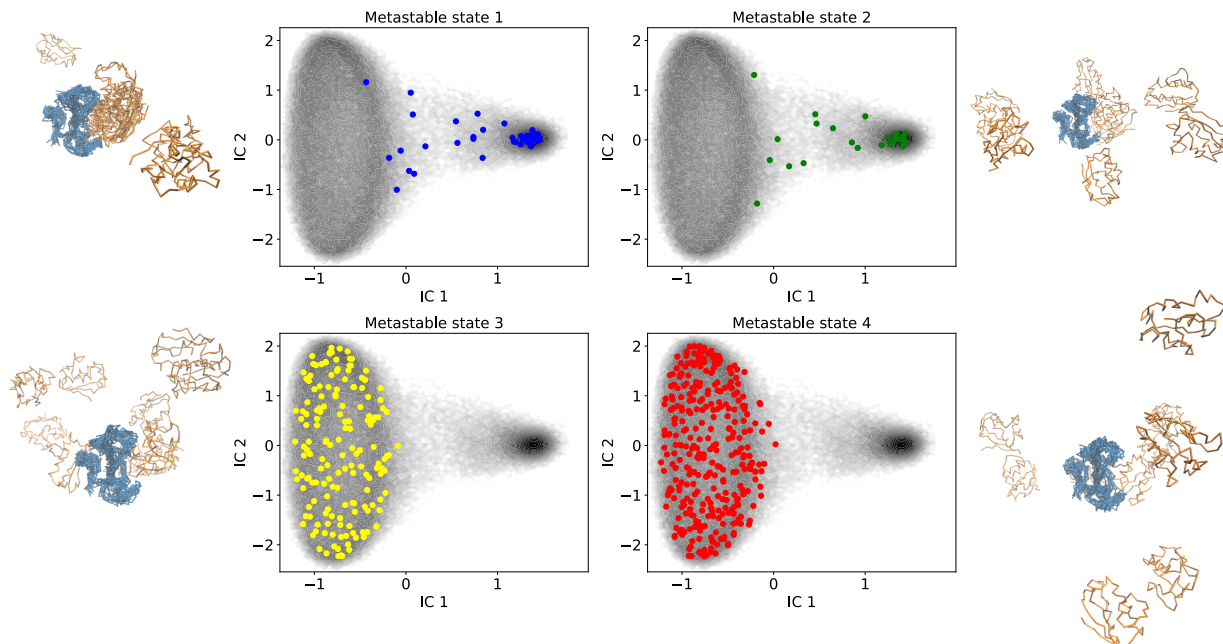
Figure 2.8: Four metastable states of MSM-6D determined by PCCA. Metastable state 1 consists of primarily bound states. Metastable state 2 consists of intermediate or loosely bound states. Metastable states 3 and 4 consist of completely dissociated complexes. PCCA assignments use fuzzy clustering, while a crisp assignment is employed to visualize how the 550 microstates map to each of the metastable states. The gray shading is the same free energy landscape shown in Fig. 2.6.

MSMs built from biased trajectories in addition to unbiased trajectories. In particular, we show that incorporating a sensitivity analysis into the TRAM construction can efficiently improve results.

1-Dimensional Biased Markov State Models

Given an undersampled and relatively short 5 μs MD trajectory, the MSM built from it using a one dimensional feature space, in this case the COM, is quite inaccurate, as shown by the MSM free energy profile in Fig. 2.9. However, adding minimal biased US data to an MSM built from undersampled MD simulation can recapitulate the same free energy profiles as an MSM from long simulations of 25 μs. The addition of only 3 ns (per window) of US simulation drastically improves upon the MSM via reweighting of the thermodynamics
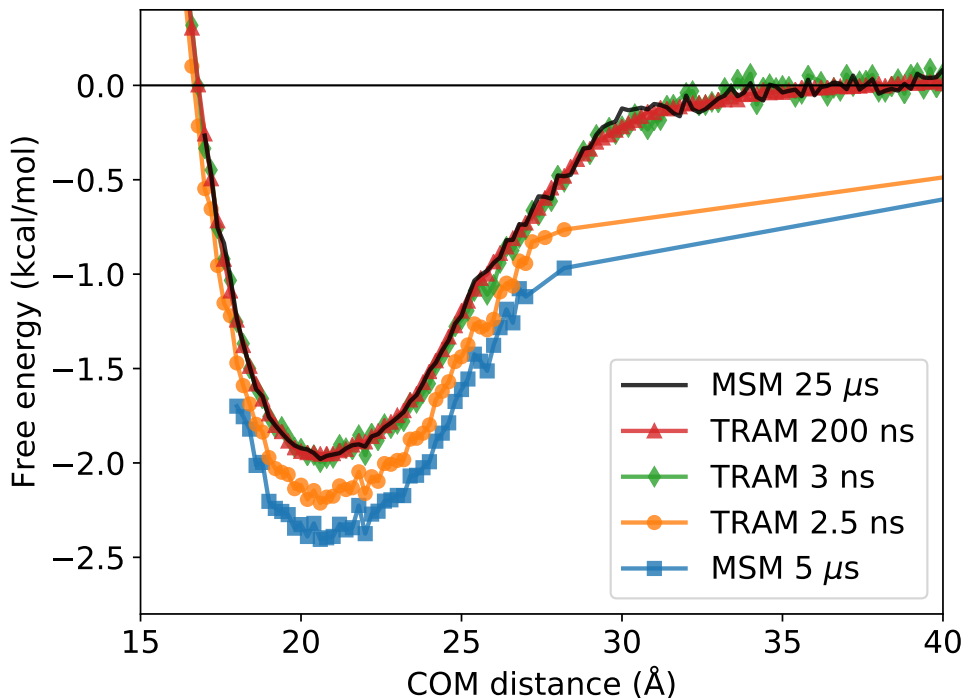
Figure 2.9: Efficiency of TRAM. The MSM from short MD trajectories of only 5 μs of simulation time (blue square) does not recover as agreeable of a free energy profile as the TRAM models constructed from a) 5 μs of MD simulation and 2.5 ns per window US simulation (orange dot), b) 3 ns per window US simulation (green diamond), and c) 200 ns per window US simulation (red triangle, TRAM-1D in Table 2.3). With the addition of only 3 ns of US simulation, TRAM is within near agreement to the reference MSM estimated from a long MD simulation time of 25 μs (black).

with TRAM. Compared to the MSM-6D from very long simulations, the MSM from short simulations yields a binding constant and rates that are vastly different. The addition of biased trajectories by way of TRAM recuperates the thermodynamics and kinetics seen from MSM-6D. The TRAM-1D model in Table 2.3 corresponds to TRAM model with 200 μs of biased simulations in Fig. 2.9. Fig. 2.10 demonstrates that PCCA assignment is able to clearly distinguish between the bound and unbound states along this feature.

Even though the bound and unbound states can be straightforwardly distinguished by the COM distances in the present model, large biomolecules often exhibit ambiguous binding pathways that involve various internal degrees of freedom and determining a correct

28
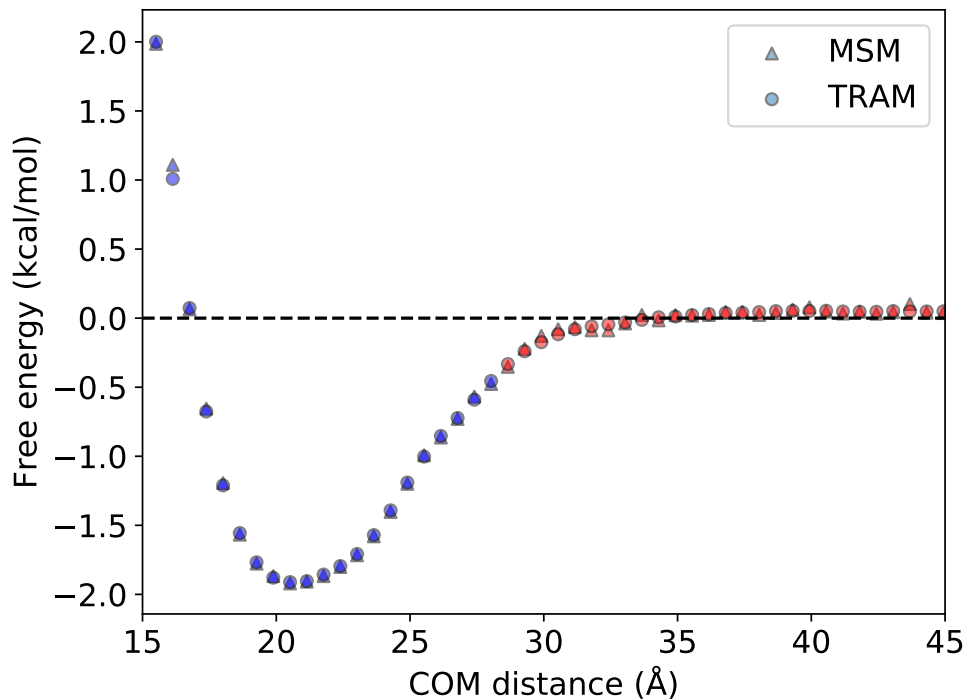
Figure 2.10: PCCA metastable states of MSM-1D and TRAM-1D. The bound (blue) and unbound (red) states are able to be clearly distinguished when using COM distances as the only feature.

reaction coordinate may be highly challenging. Still, a desired MSM model should be able to extract important binding properties using indirect reaction coordinates. We choose the squared inverse COM distances as features for TRAM-1D-inv to examine how well it can still capture the binding process and whether this less direct feature may introduce any instability near the short-range binding distance, compared with the direct COM distances. Remarkably, Fig. 2.11 shows that the free energy profile of TRAM-1D-inv is in near identical agreement with the unbiased MSM, and the thermodynamic and kinetic properties are also well-reproduced. Even though it is not a direct reaction coordinate of the binding pathway, this type of feature can resolve the bound and unbound states. Error estimation was performed using bootstrapping by sampling blocks of trajectories, but the error bars of the PMFs in Figs. 2.10 and 2.11 are three orders of magnitudes smaller and, thus, too small to
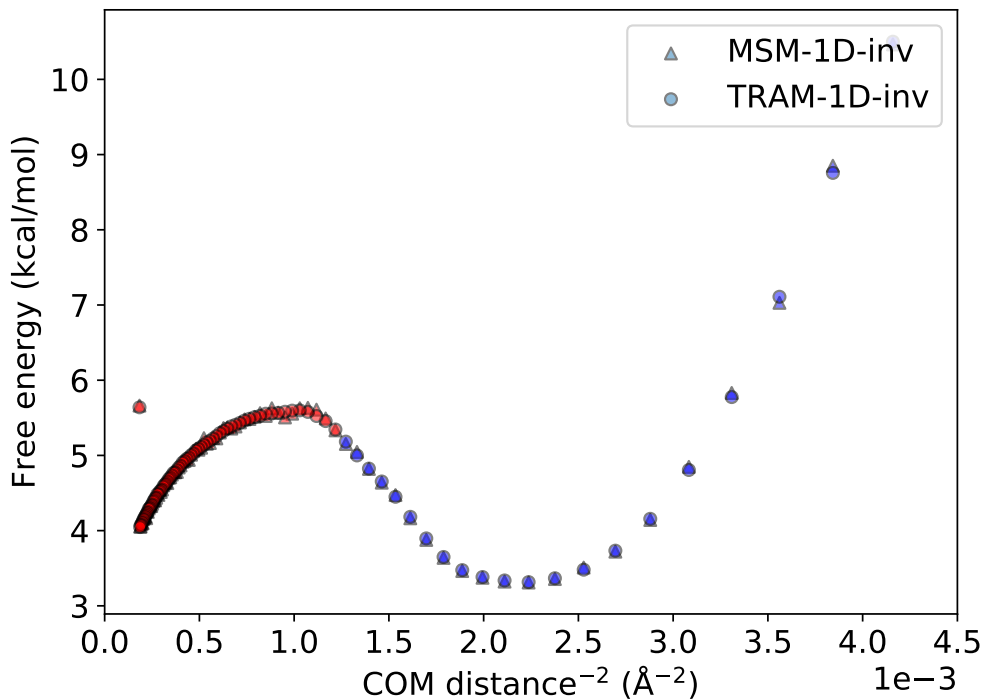
Figure 2.11: PCCA metastable sets generated from MSM and TRAM using $1/\text{COM}^2$ as the feature. The bound (blue) and unbound (red) states are still able to be clearly distinguished when using this indirect feature.

be visualized.

It is interesting to note that these one-dimensional models are able to faithfully recapitulate the thermodynamics and kinetics just as well as the more computationally expensive models, MSM-6D and TRAM-6D. This can be understood from the timescales of TICA shown in Fig. 2.2, where the first timescale is predominately larger than the other timescales by an order of magnitude. This suggests that the COM distance is the most crucial collective variable for understanding the current system, even though some orientation and internal motions are also present and should be important in order to fully understand the overall processes. Therefore, from these one-dimensional models, we conclude that the binding pathway may be accurately described using only a few well-chosen collective variables, which could prove to be extremely useful for MSMs of large protein complexes in which the binding

pathway is not completely unambiguous. Future work may involve examining such MSMs by employing features such as the dihedral angles of residues that are not explicitly related to the COM distances or any other inherently intuitive distance criteria for the binding process.

High-Dimensional Biased Markov State Models: Sensitivity Analysis to Optimize the Construction

Since a major challenge in MD studies is to obtain enough sampling, we often end up with undersampled unbiased data that has high statistical uncertainty. Earlier work involving eigenvalue-based sampling have attempted to the improve accuracy of MSMs by starting simulations from the states that present the most uncertainties in their eigenvalues or kinetics. While a few error analysis methods have been proposed in literature for use with adaptive sampling [58], here we apply a simple sensitivity analysis in order to pinpoint the discretized microstates of an MSM that contribute the most error. Then, the problematic microstates are mapped back to their corresponding subset of features (i.e., COM distance between the proteins) in order to add biased simulations for TRAM only where the additional windows will provide the most benefit. In this section, we will demonstrate that this idea is rather straightforward and easy to implement.

The relationship between the sensitivity and the complex configuration is depicted in Fig. 2.12. The highly sensitive microstates correspond to the bound states and the loosely-bound intermediate states, which is expected since these states are the key players in the binding process. We note that while this may seem readily apparent here for our CG system, it may not be as straightforward for larger and more complex biomolecular systems that have multiple different binding pathways. For such highly complicated cases, the sensitivity analysis can be even more advantageous for pinpointing regions of undersampling.

To employ this sensitivity analysis approach, we first construct a traditional MSM. A

local sensitivity matrix can be computed for each element from the transition matrix,

$$S_{ij} = \left(\frac{\partial f(\mathbf{T})}{\partial T_{ij}} \right), \tag{2.17}$$

where $f(\mathbf{T})$ is the observable of interest, and $\mathbf{T}$ is the MSM transition matrix [54, 55]. In the present case, the observable of interest is the equilibrium distribution of the states $\pi_i(\mathbf{T})$ defined by the transition matrix of the MSM.
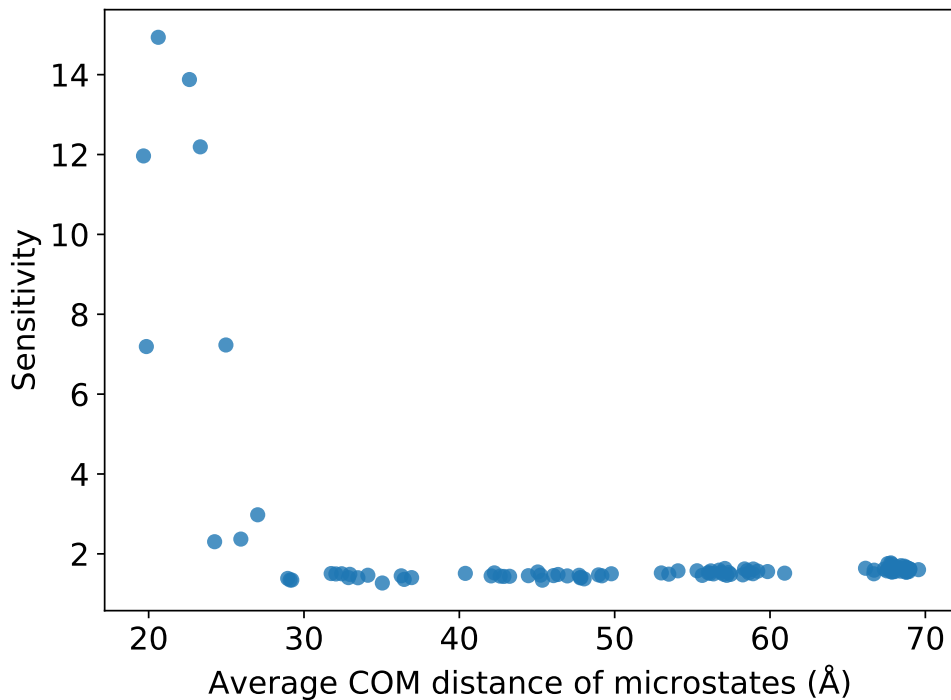
Figure 2.12: The π global sensitivity as a function of the average COM of each MSM microstate. Higher π sensitivities correspond to the microstates with shorter averaged COM distances that belong to the bound or intermediate states.

A variance-based sensitivity analysis, also known as the Sobol method [56, 85], was used to obtain the global sensitivities as follows:

$$S_{\text{global}} = \sum_{ijkl} S_{ji} \, \text{cov}[T_{ij}, T_{kl}] \, S_{kl}, \tag{2.18}$$

where S_{ji} and S_{kl} are the local sensitivity matrix elements defined from Eq. (2.17), and cov$[T_{ij}, T_{kl}]$ is the covariance of T_{ij} and T_{kl}.

The local sensitivity matrices for each of the 100 stationary distribution elements are plotted in Fig. 2.13. We can immediately see a trend where the same few microstates contribute toward the most error in all of the observables. Fig. 2.14 shows the global sensitivity of the stationary distribution observable, illustrating how the same several microstates have significantly higher sensitivity. To have a better picture of microstate sensitivity in relation to local sensitivity, Fig. 2.18 in the Appendix shows the element values of the sensitivity matrix for several other observables of a preliminary MSM built from short MD trajectories of 1 μs simulation time.

Fig. 2.15 compares the binding free energy, ΔG_{b}, from a six-dimensional traditional MSM and a six-dimensional traditional TRAM over a range of simulation time lengths. The MSM was constructed using the 25 μs aggregate MD simulations. The sensitivity analysis identified 14 US windows out of 70 total windows to be the most important for addition into TRAM, allowing for a much more computationally efficient estimation. Therefore, the following inputs were used to perform reweighting with TRAM: (1) the 25 μs aggregate MD simulations and (2) the US simulations of 200 ns per window with 14 windows biased along a COM distance of 13 Å$-$26 Å. Bootstrapping was performed to estimate the observable errors and to obtain the error bars in Fig. 2.15. The ΔG_{b} of the MSM fluctuates wildly when we have shorter trajectories and only stabilizes when we have 4 μs of aggregate simulation time. In contrast, TRAM starts to generate much more consistent results after only 1 μs of simulation time. While the error bars are relatively large for both the MSM and TRAM estimated with shorter trajectory blocks, which is also observed in general for MSMs of full atomistic simulations [51], it is encouraging to observe that the average ΔG_{b} converges considerably faster to the reference value for TRAM than for the MSM, and TRAM also generally shows lower error. As shown in Fig. 2.15(b), TRAM converges to the reference
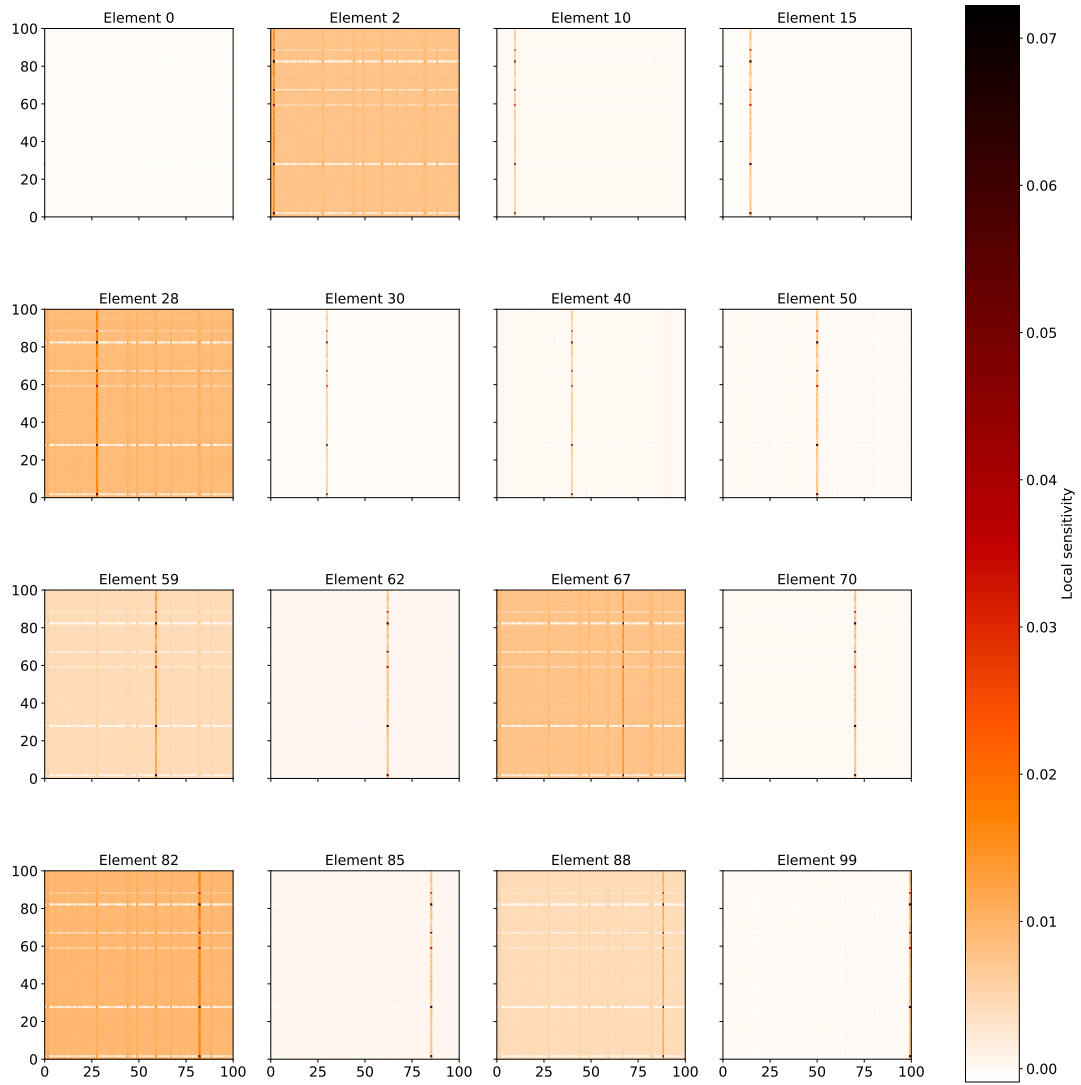
Figure 2.13: Local sensitivity matrices computed for a few selected elements of the stationary distribution. Elements 2, 28, 59, 67, 82, and 88 show the highest sensitivities, while the other elements have relatively low sensitivities.
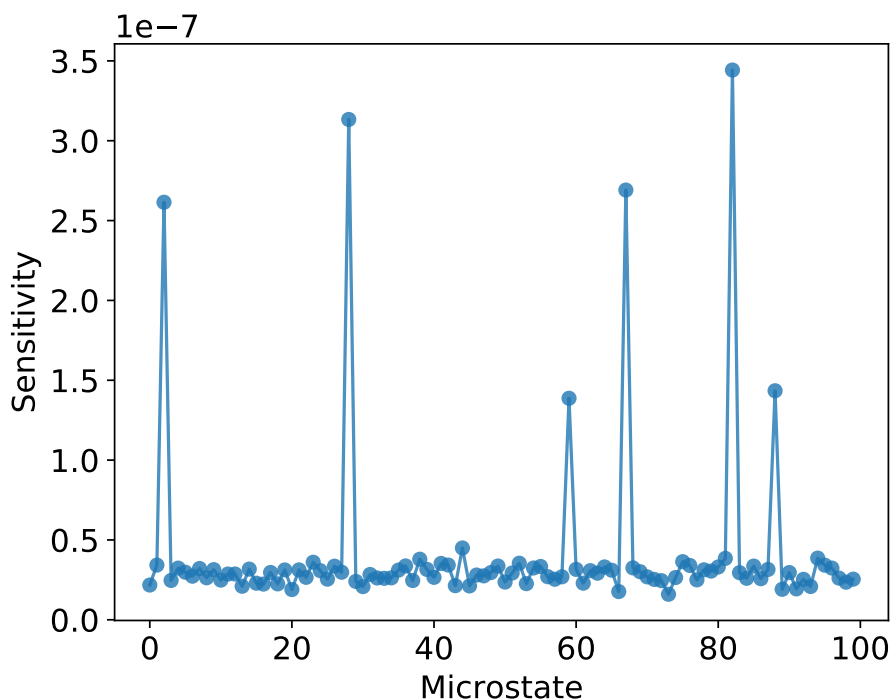
Figure 2.14: Global sensitivity analysis of the stationary distribution.

value after 3.75 μs with an error of 18.6% whereas the MSM still has not fully converged with an error of 23.1%. It is interesting to note that when less than 3 μs of MD simulation time was used to build the MSM/TRAM, we observe very high error. This can be explained due to the presence of absorbing states, of which TRAM is also susceptible. When such an absorbing state is reached, the state cannot be left within the timescale of the short simulation. Fig. 2.16 highlights this absorbing state case: for very short trajectories, we may see little to no transition events to build a reasonable MSM. The properties calculated for TRAM-6D in Table 2.3 is taken from the TRAM model built upon the full 25 μs of MD simulations and 200 ns per window of US simulations.

These results show that the presented protocol combining the adaptive TRAM scheme with the sensitivity analysis can further facilitate the construction of more accurate models while reducing the computational cost by potentially orders of magnitudes. By helping to achieve accurate statistical sampling while keeping the magnitude of the computational
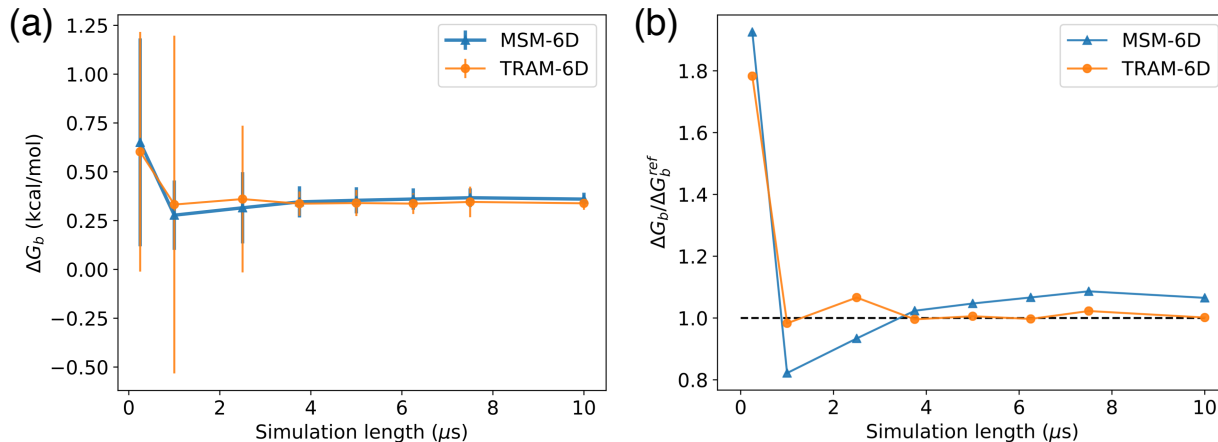
Figure 2.15: Comparison of MSM and TRAM in 6 dimensions. (a) Binding free energy ΔG_{b} from MSM and TRAM as a function of the MD simulation time. Blocks of trajectories used in the estimation are taken from the 25 μs aggregate MD simulations. For TRAM, the input also included the US trajectories of 200 ns per window with 14 windows biased along a COM distance of 13 Å$-$26 Å. These 14 US windows were identified by the sensitivity analysis to be the most important windows out of 70 total windows for addition into TRAM. (b) Convergence of ΔG_{b} compared to the reference value from MSM-6D built using the full 25 μs of simulation time. After 3.75 μs, TRAM has converged with an error of 18.6% while MSM has not with a relatively larger error of 23.1%.

effort under control, this focused TRAM approach should be especially advantageous in the construction of MSMs for large biomolecular systems.

2.4   Conclusion

To obtain accurate thermodynamics and kinetic properties of large systems such as biomolecules and protein complexes, MSMs are generally constructed and then judged on the basis of on dynamical criteria. However, the overall construction process may become inefficient and even ambiguous when the wide range of possibilities for the numerous methodological aspects of MSMs (featurization, discretization, lag-time) are further compounded by sampling limitations.

In this work, we seek to illustrate the conditions under which MSMs may be able to perform consistently by exploring how models constructed from different features and sim-
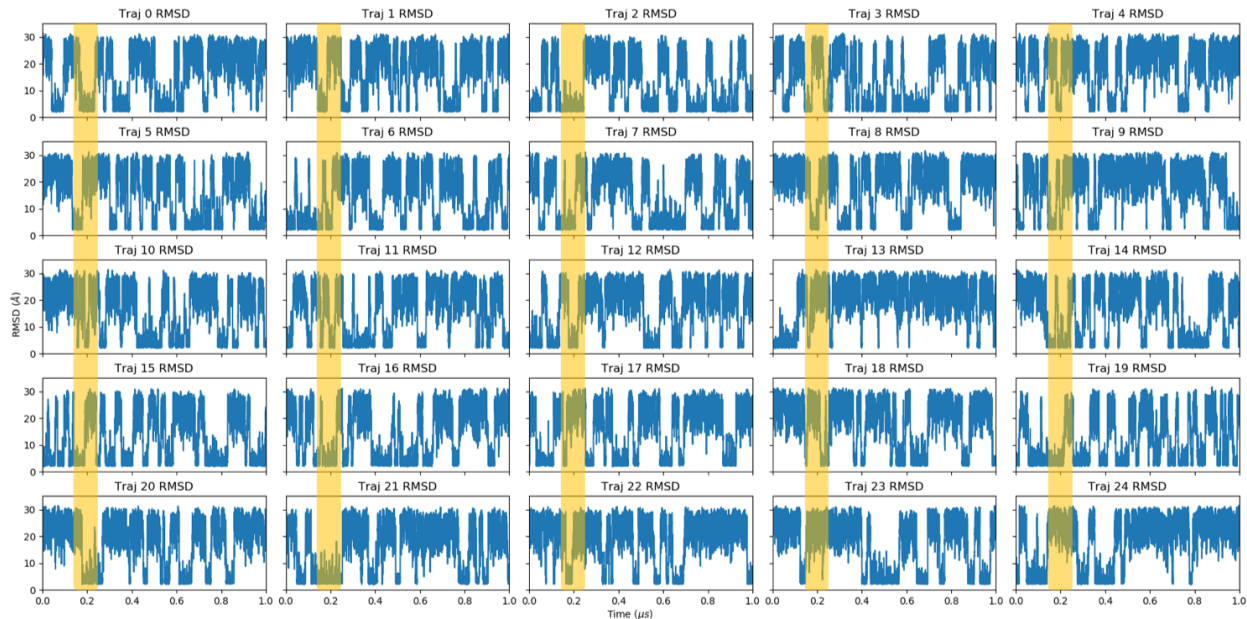
Figure 2.16: MSMs built upon shorter simulations have high errors due to absorbing states. Once the MSM enters the state, it cannot then leave. For each long independent trajectory (blue), if we choose sample block frames of 500 ns or shorter, then it is highly likely that we will observe absorbing states (yellow) or too few transitions between states to make an accurate MSM.

ulations at different thermodynamic states are able to capture the binding process and produce observables in good agreement with each other. While simulation data from an all-atom model would yield more accurate and realistic information, full atomistic simulations of large biosystems are highly demanding. In this work, we constructed the MSMs based on the CG representation of the barnase-barstar protein complex, where the simplified nature of the model allows for efficiently constructing and evaluating many different MSMs under different conditions.

Taking advantage of the sensitivity analysis, we showed that one can pinpoint precisely where to add these biased simulations with the help of TRAM in order to improve sampling and reduce computational effort. For large protein complexes requiring extensive computations, the ability to incorporate a small set of well-chosen biased simulations in MSMs is expected to be of tremendous value. The next step will be to implement the MSM-based

strategy proposed here to process and analyze the results of an all-atom simulation of the barstar-barnase complex with explicit solvent. Using similar features such as the Cα's to create a bottom-up CG model, the strategy is expected to impart a more accurate MSM estimation at lower computational costs. This work is underway.

We conclude by noting that the MSMs in this work are quite robust and seem to be invariant to the complexity of input data, even when the number of features is highly reduced. From our CG protein complex, the MSMs are able to resolve the binding process very well. Notably, the stripping the features down to one dimension, as discussed in Section 2.3.2, does not seem to affect the MSM, and the observables remain in agreement to those from higher dimensional MSMs. This could prove to be especially applicable for large proteins, of which we could build CG designs and construct their MSMs from a minimal set of features. Given the success of CG modeling for biomolecules [86–88], this work serves as a stepping stone for introducing MSM analysis to more rigorously-designed reduced models of interest in order to not only accurately but also efficiently reproduce dynamics. Future work includes qualitatively recapitulating the thermodynamic and kinetic information from the all-atomistic barnase-barstar complex, with a special focus on improving the description of the dissociation process through TRAM. For other more complicated protein-protein interactions, Hamiltonian replica exchange molecular dynamics (H-REMD) [89] may be useful to circumvent sampling issues and aid in the efficiency of TRAM [90].

One end goal of computational biochemistry is to provide accurate free energies that are comparable with the experimental observables, with errors in the order of $k_{\mathrm{B}}T$. While results are certainly limited by force field accuracy, sampling remains problematic due to the enormous computational costs. The strategies presented here can provide insight for the design of more effective all-atom computations to help overcome sampling challenges, progressively moving toward quantitatively reliable computational predictions.

2.5   Appendix

This Appendix section contains supplementary information that are relevant to the results and discussions presented Chapter 2.

Table 2.4: Relaxation times calculated for different bound cutoff distances.

r_{cut} (Å)	τ_1 (ns)	τ_2
25	25.7	158.6
26	26.0	159.2
27	26.1	159.2
28	26.1	159.3
29	**26.1**	**159.4**
30	26.0	159.2
31	25.8	158.8
32	25.5	158.5
33	25.2	157.6
34	24.9	156.9
35	24.7	155.9
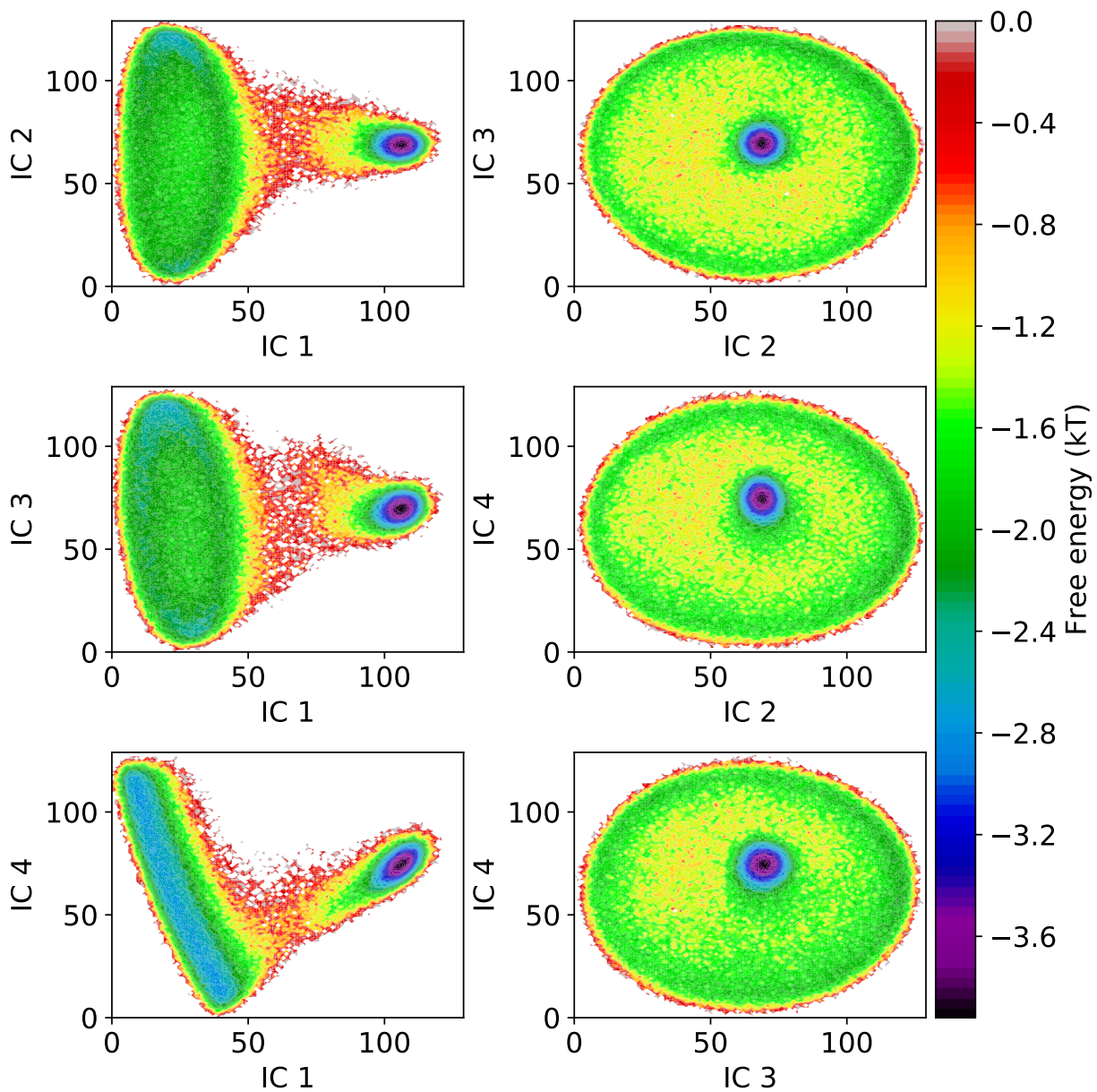
Figure 2.17: The free energy histogram in the TICA space. The relationship between the four slowest independent components (IC) are shown. IC 1 is the slowest degree of freedom and corresponds to the COM distance between the two proteins in the complex. IC 2, 3, and 4 represent the orientation angles between the proteins.
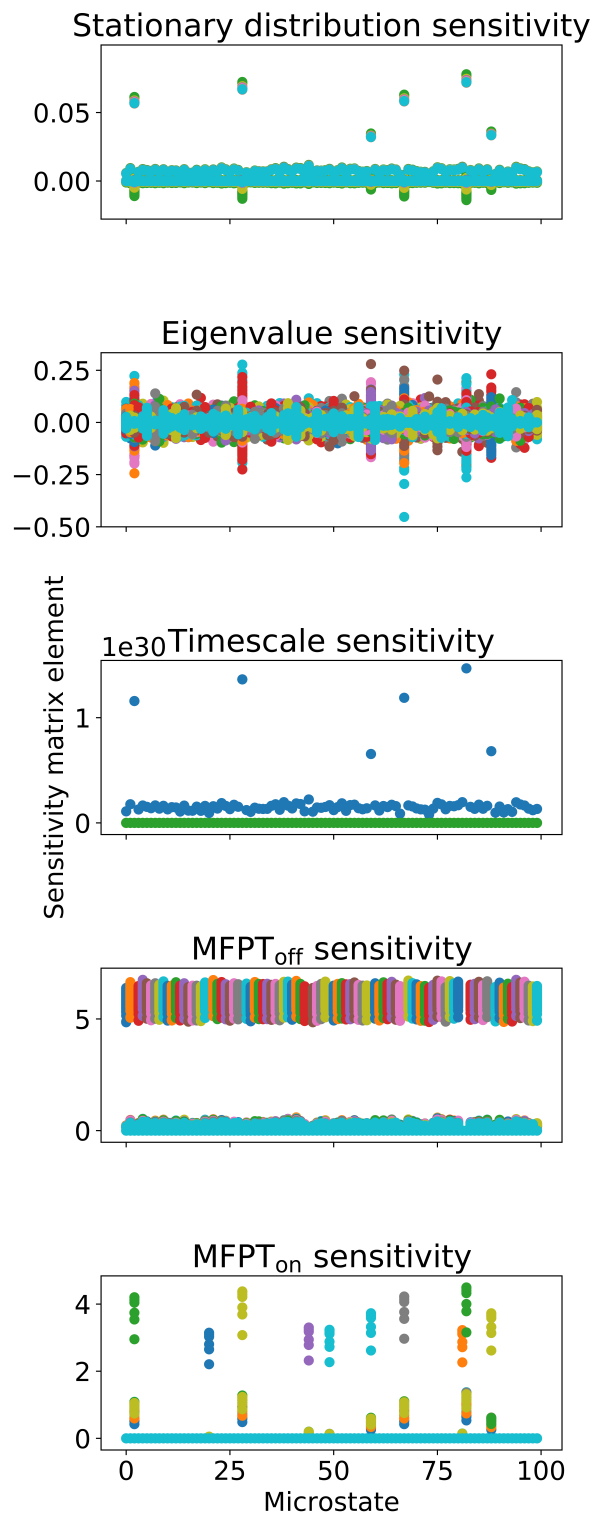
Figure 2.18: Values of the local sensitivity matrix elements for the stationary distribution, eigenvalue, MSM timescale, MFPT$_{\text{off}}$, and MFPT$_{\text{on}}$.

CHAPTER 3

COMMITTOR-CONSISTENT VARIATIONAL STRING

METHOD

The material from this chapter is adapted from the following manuscript submitted for peer review publication: Z. He, C. Chipot, B. Roux, Committor-Consistent Variational String Method.

3.1 Introduction

One of the major challenges in computational studies of biomolecular systems is the characterization of slow conformational transitions between metastable states. This is also an important objective of high biological significance. To understand how these complex "biomolecular machines" work, one must be able to visualize the manner in which they move and change their shape atom-by-atom as a function of time during the biological process. Although static structural information has been rapidly accumulating, in databases [91], there is considerably less data about protein motions. Knowledge of a transition pathway makes it possible to identify and test experimentally transient structures that play key roles near transition states [92–94]. Ultimately, advancing our knowledge of any complex conformational transition is likely to require a combination of both experimental data together with virtual pathways generated via computational approaches.

A wide range of computational methods and strategies have been developed to treat slow transitions in complex molecular systems [19,20,33,36,37,95–105] Considering a prototypical system with two metastable states A and B, an important concept is the committor probability that a trajectory initiated at some configuration will ultimately reach the state B before ever reaching state A, which is thought to represent an optimal one-dimensional reaction coordinate (RC) representing the progress of the slow $A \leftrightarrow B$ transitions [24, 31, 106–109].

Useful strategies to identify the slowest degrees of freedom and potentially discover the RC from a set of user-defined collective variables $\mathbf{z}$ (CVs) are the time-lagged independent component analysis (TICA) [49, 110, 111] of the spectral gap optimization of order parameters (SGOOP) [110, 111]. Increasingly, machine learning (ML) and neural networks (NN) methodologies provide a powerful route to enable the discovery of complex RCs that are nonlinear functions of the CVs [112–115]. This progress notwithstanding, the lack of sampling can undermine the ability of ML methodologies to correctly learn arbitrarily complex RCs from high-dimensional MD data [116, 117]. Inspired by the string method, a powerful and yet simple way to circumvent this issue and incorporate nonlinearity is to represent the RC as a one-dimensional curve, or chain-of-states, embedded in the high-dimensional space of the CVs [36, 37, 101]. According to transition path theory (TPT), the "reaction tube" defined by the string is expected to support most of the reactive probability current governing the long time relaxation from A to B, and this current is largely determined by the variations in the committor [24]. However, present algorithms to determine the string either seek to find the minimum free energy path (MFEP) [36] or a path following the local probability current determined from local mean drifts [30, 37]. While useful in their own rights, these constructs do not directly provide information about the committor probability, and hence, the reactive probability current. Our goal here is to address this issue by introducing a novel algorithm to variationally determine an optimal "committor-consistent" curvilinear string transition pathway in the space of the CVs.

3.2 Theoretical Development

3.2.1 Effective Dynamical Propagator

To reduce the complexity of the problem, one typically seeks to determine the optimal pathway within the subspace of reduced dimension spanned by a subset of collective variables

(CVs), $\tilde{\mathbf{z}}(\mathbf{x}) = (\tilde{z}_1(\mathbf{x}), \ldots, \tilde{z}_N(\mathbf{x}))$, i.e., a vector-valued function that maps every configuration $\mathbf{x}$ of the system on a set of values $\tilde{\mathbf{z}}(\mathbf{x})$. In this context, the string represents the pathway linking the states A and B as a discrete "chain of state", i.e., a collection of M images located at the positions $\{\mathbf{z}^1, \ldots, \mathbf{z}^M\}$ in the subspace of the CVs. To characterize the string pathway, the long-time dynamics of the system within the subspace of the CVs is critical. The probability density of the system at time t is expressed as $\rho(\mathbf{z}; t)$. The forward propagation step $(\mathbf{z} \to \mathbf{z}')$ for the probability density from the time t to the time $t + \tau$ is,

$$\rho(\mathbf{z}'; t + \tau) = \int d\mathbf{z} \, \mathcal{P}_\tau(\mathbf{z}'|\mathbf{z}) \, \rho(\mathbf{z}; t). \tag{3.1}$$

where $\mathcal{P}_\tau(\mathbf{z}'|\mathbf{z})$ is the propagator (also called transfer operator). The dynamics within the reduced subspace of the CVs is assumed to be Markovian with a finite lag-time τ, and that $\mathcal{P}_\tau$ obeys the Chapman-Kolmogorov equation, $\boldsymbol{\rho}(t + n\tau) = \boldsymbol{\mathcal{P}}_{n\tau} \cdot \boldsymbol{\rho}(t)$, with $\boldsymbol{\mathcal{P}}_{n\tau} = (\boldsymbol{\mathcal{P}}_\tau)^n$. The system is also assumed to be in equilibrium and that detailed balance is satisfied, $\mathcal{P}_\tau(\mathbf{z}'|\mathbf{z}) \, \rho_{eq}(\mathbf{z}) = \mathcal{P}_\tau(\mathbf{z}|\mathbf{z}') \, \rho_{eq}(\mathbf{z}')$. Under these conditions, the effective propagator $\boldsymbol{\mathcal{P}}_\tau(\mathbf{z}'|\mathbf{z})$ yields a self-consistent representation of the dynamics of the system within this subspace (closure of the dynamical propagation).

3.2.2 Committor Probabilities for Two Metastable States

Assuming two metastable states A and B, the forward committor $q(\mathbf{z})$ is the sum of the probability over all paths starting at $\mathbf{z}$ that ultimately reach the state B before ever reaching the state A. The probability of each of these paths is expressed as a product of discrete propagation steps $\boldsymbol{\mathcal{P}}_{n\tau} \cdots \boldsymbol{\mathcal{P}}_{n\tau}$ with lag-time τ, under the restriction that the intermediate states resulting from all these steps are $\notin A, B$. Summing over all possible paths, it follows

that $q(\mathbf{z})$ can be written as,

$$q(\mathbf{z}) \;=\; \int d\mathbf{z}'\, q(\mathbf{z}')\, \mathcal{P}_\tau(\mathbf{z}'|\mathbf{z}), \qquad (3.2)$$

with the constraints $q(\mathbf{z}) = 0$ if $\mathbf{z} \in A$, and $q(\mathbf{z}) = 1$ if $\mathbf{z} \in B$, see Eq. (3.18) for details. By construction, $0 \le q(\mathbf{z}) \le 1$. While the equations for the committor probabilities involve only the elementary propagator. $\mathcal{P}_\tau(\mathbf{z}'|\mathbf{z})$ for the lag-time τ, the fundamental validity of these equations is predicated upon the necessity to satisfy Markovity of the dynamics as expressed by the Chapman-Kolmogorov equation, $\boldsymbol{\mathcal{P}}_{n\tau} \equiv (\boldsymbol{\mathcal{P}}_\tau)^n$.

3.2.3   Net Forward Flux from Reactive Pathways

One can express the net forward reactive flux from A to B as [24, 26, 30, 32, 107, 118]

$$J_{AB} = \;=\; \frac{1}{2\tau} \int d\mathbf{z} \int d\mathbf{z}'\, \big(q(\mathbf{z}') - q(\mathbf{z})\big)^2 \mathcal{P}_\tau(\mathbf{z}'|\mathbf{z})\, \rho_{\mathrm{eq}}(\mathbf{z}). \qquad (3.3)$$

See Eq. (3.28) for details. Equivalently, J_{AB} can also be expressed as a time-correlation function,

$$
\begin{aligned}
J_{AB} &= \frac{1}{2\tau} \big\langle \big(q(\tau) - q(0)\big)^2 \big\rangle \\
&= \frac{1}{\tau} \big(\langle q(0)q(0)\rangle - \langle q(\tau)q(0)\rangle\big).
\end{aligned}
\qquad (3.4)
$$

In the following sections, we refer to $\langle q(0)q(0)\rangle - \langle q(\tau)q(0)\rangle = C(\tau)$ as the the committor time-correlation function. While $q(\mathbf{z})$ is a probability, the committor time-correlation function in Eq. (3.4) can be understood by recalling that the set of collective variables is a vector-valued function that maps every microscopic configuration $\mathbf{x}(t)$ of the system onto a set of values $\tilde{\mathbf{z}}[\mathbf{x}(t)]$ along a dynamical trajectory. Assuming that the function $q(\mathbf{z})$ is known, we write $q(\tilde{\mathbf{z}}[\mathbf{x}(t)])$ as $q(t)$ for the sake of simplicity.

3.2.4 Basis Set Expansion of the Committor

The quadratic expression for the reactive flux J_{AB} from Eqs. (3.3), or equivalently Eq. (3.4), can serve as a robust variational principle to optimize a trial committor $q(\mathbf{z}')$. Minimizing the quantity J_{AB} with respect to a trial function $q(\mathbf{z})$, $\delta J_{AB}/\delta q = 0$ recovers Eq. (3.2) that formally defines the committor probability. Minimization of the steady-state flux J_{AB} defined by Eq. (3.4) for a trial function q with the constraints $q(\mathbf{z}) = 0$ if $\mathbf{z} \in A$, and $q(\mathbf{z}) = 1$ if $\mathbf{z} \in B$ yields the correct committor $q(\mathbf{z})$, defined by Eq. (3.2). See Eq. (3.29) for futher details. We seek to express the trial function $q(\mathbf{z})$ in terms of a basis set expansion, which has shown success in the estimation of committors in literature [28, 29]. However, the construction of the trial function requires special care to handle the constraints imposed by the boundary states. For our set of basis functions $f_i(\mathbf{z})$, we choose Voronoi cells supported by a set of M centroids corresponding to the images of a string connecting boundary states A and state B. We write the committor as

$$
\begin{aligned}
q(\tilde{\mathbf{z}}(\mathbf{x})) \;=\; & h_A(\tilde{\mathbf{z}}(\mathbf{x}))\, q_A + h_I(\tilde{\mathbf{z}}(\mathbf{x})) \left(\sum_{i=1}^{M} b_i\, f_i(\tilde{\mathbf{z}}(\mathbf{x})) \right) \\
& + h_B(\tilde{\mathbf{z}}(\mathbf{x}))\, q_B,
\end{aligned}
\tag{3.5}
$$

where $q_A = 0$ and $q_B = 1$, and h_A, h_B, and h_I are indicator functions correspondingly equal to 1 when the system is in the A, B, or the intermediate region, and zero otherwise. By construction, $h_A + h_I + h_B = 1$, and all cross products of indicator functions are identically zero ($h_A h_I = h_A h_B = h_I h_B = 0$) because there is no overlap between the 3 different regions. Using the trial function in Eq. (3.5) we can express the committor time-correlation function

as,

$$\langle q(\tau)\, q(0)\rangle \;=\; \left\langle \left(h_I(\tau)\left(\sum_{i=1}^{M} b_i\, f_i(\tau)\right) + h_B(\tau)\right)\right.$$

$$\left.\left(h_I(0)\left(\sum_{j=1}^{M} b_j\, f_j(0)\right) + h_B(0)\right).\right\rangle \tag{3.6}$$

The committor time-correlation function be expanded as,

$$C(\tau) \;=\; \frac{1}{2}\mathbf{b}^t\left(\mathbf{D}(0) - \mathbf{D}(\tau)\right)\mathbf{b} + \left(\mathbf{g}(0) - \mathbf{g}(\tau)\right)\cdot\mathbf{b}$$

$$+\langle h_B(0)h_B(0)\rangle + \langle h_B(\tau)h_B(0)\rangle, \tag{3.7}$$

where

$$D_{ij}(\tau) \;=\; \langle h_I(0)\, h_I(\tau)\, f_i(0)\, f_j(\tau)\rangle$$

$$+\langle h_I(0)\, h_I(\tau)\, f_j(0)\, f_i(\tau)\rangle, \tag{3.8}$$

and

$$g_i(\tau) = \langle h_I(\tau)\, h_B(0)\, f_i(\tau)\rangle + \langle h_I(0)\, h_B(\tau)\, f_i(0)\rangle. \tag{3.9}$$

Then, taking the derivative with respect to the basis set coefficients yields the linear system of equations, we obtain

$$\left(\mathbf{D}(0) - \mathbf{D}(\tau)\right)\mathbf{b} + \left(\mathbf{g}(0) - \mathbf{g}(\tau)\right) \;=\; 0 \tag{3.10}$$

with the simple solution,

$$\mathbf{b} = -\left(\mathbf{D}(0) - \mathbf{D}(\tau)\right)^{-1}\left(\mathbf{g}(0) - \mathbf{g}(\tau)\right). \tag{3.11}$$

Substituting the M coefficients $\{b_1\}$ determined from Eq. (3.11) into Eq. (3.7) yield the optimized committor time-correlation function $C(\tau)$ for a given basis set. Because of the indicator functions $h_I(0)$ and $h_I(\tau)$ in $\mathbf{D}$, the basis functions must be chosen such that they either fully or at least partially reside in the intermediate region to avoid singularities with the matrix inversion. Eq. (3.11) is a central result of this analysis and enables the optimization of a committor-consistent string pathway.

3.2.5   Global Optimization of the Committor-Consistent String

Using the variational principle with the committor time-correlation function, $C(\tau)$ it is possible to optimize the position of the M images of a string in a committor-consistent manner. Adopting a Voronoi basis set expansion, $C(\tau)$ depends on the M basis set coefficients $\{b_1, \ldots, b_M\}$, and depends also–in a non-linear fashion–on the position of the M centroids $\{\mathbf{z}_1, \ldots, \mathbf{z}_M\}$. Thus, we have the correlation function $C(\tau; \{b_1, \ldots, b_M; \mathbf{z}_1, \ldots, \mathbf{z}_M\})$. To optimize the string according to the variational principle, we must minimize the committor time-correlation function with respect to the position of the M images. To this end, we have adopted an iterative Monte Carlo procedure, by which we first determine the basis set coefficient via Eq. (3.11), and then introduce random changes in the position of the images that are accepted or rejected on the basis of $C(\tau; \{b_1, \ldots, b_M; \mathbf{z}_1, \ldots, \mathbf{z}_M\})$. To achieve a complete optimization of the pathway and obtain a committor-consistent string, these two operations must be repeated iteratively until convergence, i.e., until one cannot further minimize $C(\tau; \{b_1, \ldots, b_M; \mathbf{z}_1, \ldots, \mathbf{z}_M\})$. The optimization process can be initiated with a string constructed either from the mean force [36], or the mean drift calculated from swarms-of-trajectories [37]. Further analysis indicates that the resulting pathway is a 1D line going from A to B that follows the committor gradient $\boldsymbol{\nabla}q(\mathbf{z})$ the space of the CVs $\mathbf{z}$.

3.2.6 Equilibrium Average and Enhanced Sampling

The time-correlation function $C(\tau)$ should be averaged over equilibrium initial conditions. In practice, it is likely that enhanced sampling techniques would be necessary to have an accurate result in the presence of large free energy barriers. An effective strategy to improve the conformational sampling relevant to a slow A-B transition is to introduce a biasing potential along a progress path collective variable (PCV) $\tilde{s}[\mathbf{z}]$ function, expressed as a differentiable function of the CVs $\mathbf{z}$ [101, 119, 120]. Once this enhanced sampling along s is achieved, we can generate unbiased trajectories initiated from specific regions at $t = 0$ according to the value of s. The unbiased time-correlation function $C(\tau)$ can then be expressed as,

$$C(\tau) \;\; = \;\; \int_0^1 ds\, \rho_{eq}(s)\, \langle q(\tau)\, q(0) \rangle_{(s)}, \tag{3.12}$$

where $\langle q(\tau)q(0) \rangle_{(s)}$ is the time-correlation function calculated from an unbiased trajectory initiated with $\tilde{s}[\mathbf{z}(t)] = s$ at $t = 0$, and ρ_{eq} is the equilibrium probability starting of starting at s. See Eqs. (3.40) and (3.41) for details.

3.3 Results and Discussion

3.3.1 Illustration with One-Dimensional Double-Well Potential

We first illustrate the variational framework in the case of a simple one-dimensional double well. A simple set of discrete one-hot indicator functions was used.

The widths of the one-hot indicators were automatically assumed by even spacing across the intermediate region. The result in Figure 3.1 shows that the exact committor is essentially reproduced by solving Eq. (3.11) for the basis functions. An example with Gaussian functions is given in Supp Info (Figure 3.7) to illustrate how basis set and hyperparameter choices affect committor probability.
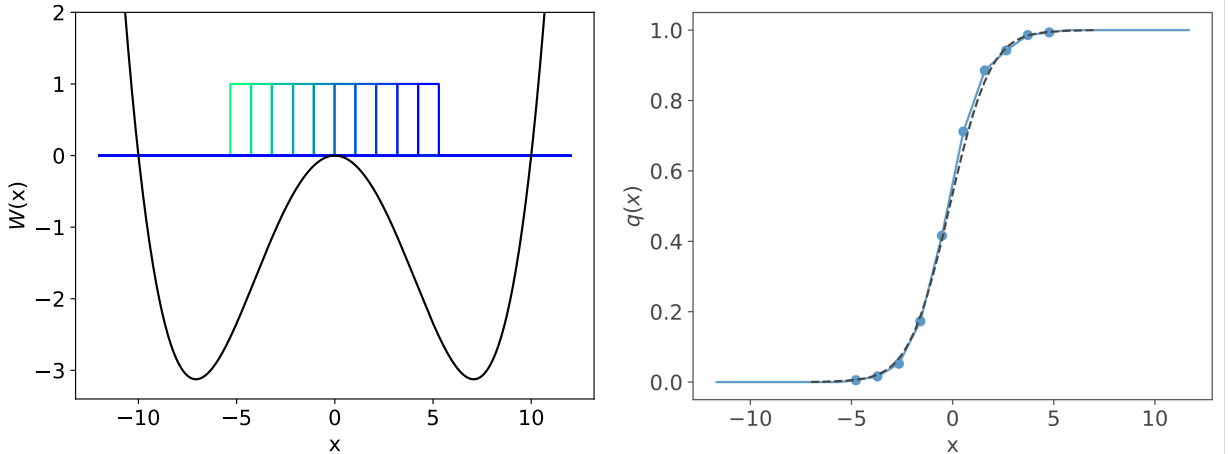
Figure 3.1: Illustration of a one-dimensional double well using using ten one-hot indicator functions and the resulting committor probability. The boundaries near the well minima where $q = 0$ or 1 were defined to be within 1 $k_B T$ of the well depth, or at $x = -5.31$ and $x = 5.31$. The black dashed line is the exact committor calculated numerically from the double well potential.

3.3.2   Illustration with Two-Dimensional Potential

We now illustrate the usefulness of the proposed framework in finding a string that follows the dominant reaction pathway in a multi-dimensional space. As a prototypical two-state system, we used the two-dimensional (2D) potential shown in Figure 3.2 that was previously studied by Berezhkovskii and Szabo to examine the effect of anisotropic diffusion on the reaction rate [106]. This 2D potential, which we will refer to as the 2D-BS potential, was previously used by Tiwary and Berne to illustrate the SGOOP method [121] and by Roux to illustrate the committor variational principle [30]. Here, the string is assumed to be a straight line with one-hot indicator functions evenly spacing across the intermediate region. The amplitude of the basis set coefficients is determined by solving Eq. (3.11).

To demonstrate the effect of anisotropic diffusion, we considered three conditions: $\delta = 0.1$, $\delta = 1$, and $\delta = 10$, where $\delta = D_y/D_x$. In each case, a different optimal reaction direction about the saddle region was discovered (depicted by the dashed lines in Figure 3.2, top left). For analysis and computation of the committors, a lag time τ of 1 time step was selected.

The boundary conditions for where $q = 0$ or 1 were defined by ellipses at the well minima such that the trajectory spends approximately 50% of the time within the ellipses and the other 50% of the time outside of the region
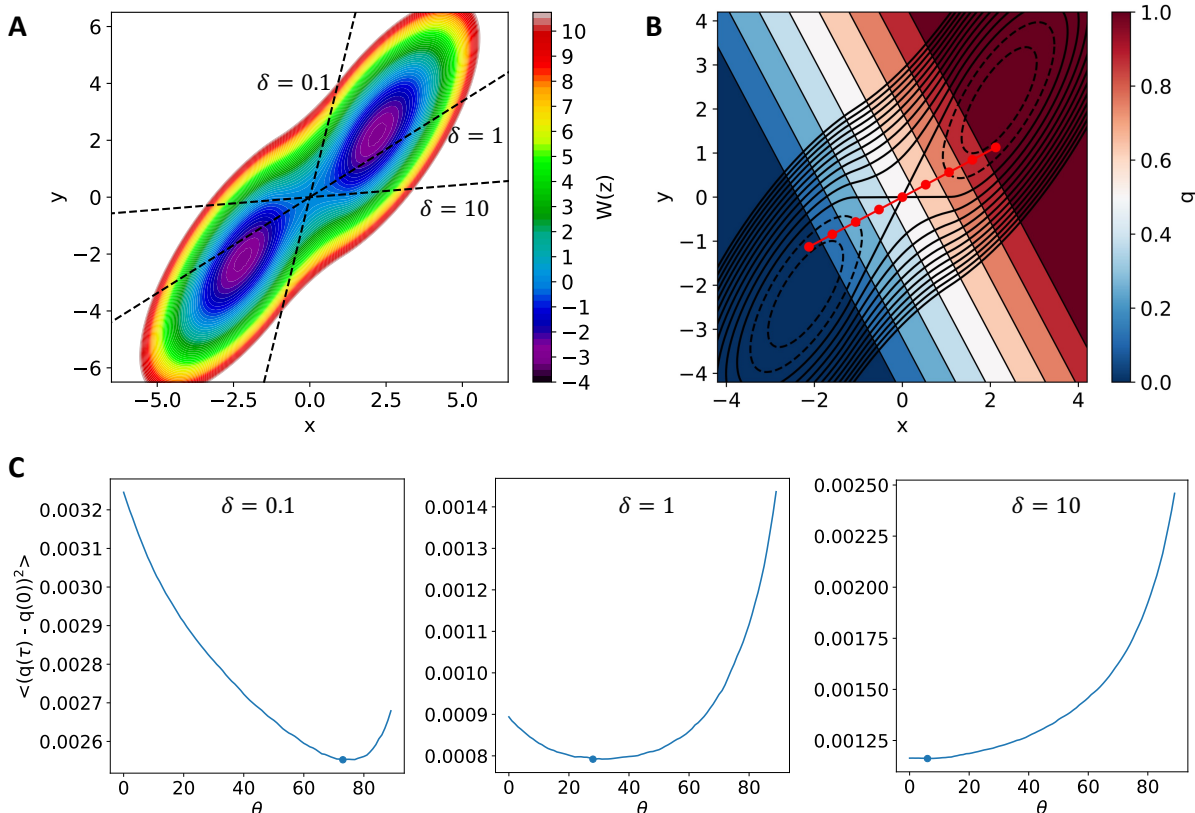
Figure 3.2: Berezhkovskii-Szabo potential and correlation functions. (A) The 2D-BS potential surface with dashed lines showing the angle of the optimal reaction pathway for the diffusion cases obtained using a basis set of 9 Voronoi in the intermediate region: $\theta = 6°$ for $\delta = 10$, $\theta = 28°$ for $\delta = 1$, and $\theta = 73°$ for $\delta = 0.1$. (B) Voronoi tesselation of the straight pathway for $\delta = 1$. The Voronoi cells are colored by the value of the committor, sequentially increasing from $q = 0$ (blue, bottom left) to $q = 0$ (white, middle region) to $q = 1$ (red, top right). (C) Dependence of the time-correlation function on the angle θ for $\delta = 10$ (left), $\delta = 1$ (middle), $\delta = 0.1$ (right). The minimum of the correlation function of each diffusion case is indicated by the blue dot and taken to be the angle of the optimal reaction pathway at the saddle point.

For the sake of simplicity, we first consider a straight reaction pathway for the 2D-BS potential, we optimize the angle of the path. As the angle is varied from 0 to 90° with respect to the x-axis, the committor-correlation function is computed by Eq. (3.7). The minimum

51

correlation function value is taken to be the best angle for the reaction pathway through the saddle point. Assuming a Voronoi tesselation of the 2D space based on the straight pathway, the estimated committor for $\delta = 1$ is shown in Figure 3.2 (top right).

The optimized curvilinear strings for the 3 diffusion cases are shown in Figure 3.3. The positions of the images of the string were optimized by variationally minimizing the committor correlation function using Monte Carlo sampling, solving Eq. (3.11) and evaluating Eq. (3.7) at every iteration. Starting from the string shown by the black curve, a box of size 0.05×0.05 was used to sample around each image position. Here, we refer to one Monte Carlo iteration cycle as moving and then computing the committor-correlation function for every image on the string for up to 1000 moves. Once a move is accepted for a new image position that results in a lower committor-correlation function value, then the Monte Carlo sampling for that image stops and proceeds to the next image. If after 1000 moves none were accepted, then that image in the iteration cycle is assumed to be converged and we proceed to sample for the next image. For $\delta = 0.1$, 1, and 10, the Monte Carlo procedure required 56, 25, and 42 iterations, respectively, to reach convergence. Notably, we observe that the curvilinear string crosses the transition state region differently depending on the parameter δ. The minimum free energy path (MFEP) is shown in black. This path is valid only in the case of isotropic diffusion with $\delta = 1$. In the other cases, the committor-consistent optimized string departs from the MFEP.

The string method aims to determine a 1D curve in the subspace of the collective variables, $\mathbf{z}$ that links state A and B. However, what ought to be the most relevant curve that one should seek to determine is not immediately clear. An analysis of the diffusional motion in the 2D-BS potential is helpful to address this question. Formally, different string pathways can be defined assuming that the local tangent of the curve follows a specific vector at $\mathbf{z}$. We consider four possibilities for the vector used to define the tangent of the string. First, the tangent to the string may follow the mean force (the gradient of the PMF), $-\boldsymbol{\nabla}W(\mathbf{z})$.
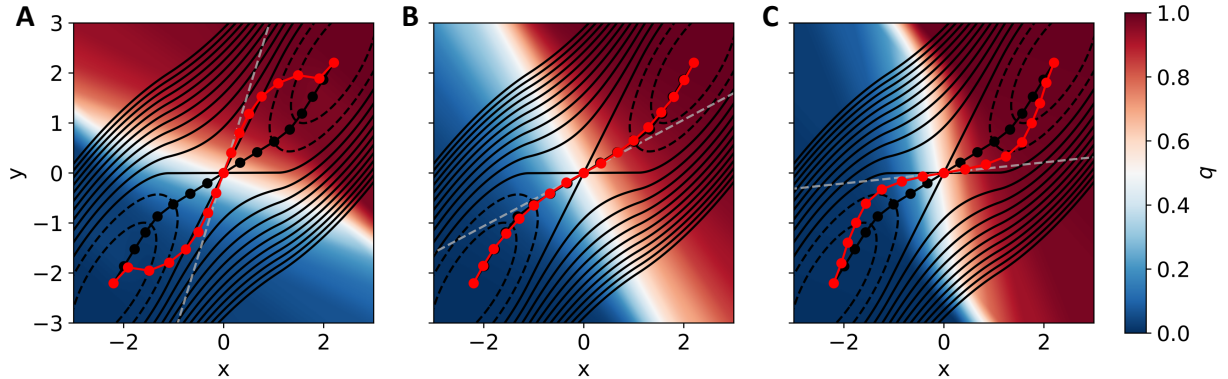
Figure 3.3: String obtained by variationally minimizing the correlation function with Monte Carlo sampling and the resulting committor probability for three diffusion conditions: (A) for $\delta = 0.1$, (B) for $\delta = 1$, and (C) for $\delta = 10$. For all three cases, optimization was performed by starting from the MFEP string shown by the black curve; a box of size 0.05×0.05 was used to sample around each image position in the 2D plane. One Monte Carlo iteration cycle comprises moving the image, and then computing the committor-correlation function. Once a move is accepted for a new image position that results in a lower committor-correlation function value, then the Monte Carlo sampling for that image stops and proceeds to the next image. If after 1000 moves none were accepted, then that image in the iteration cycle is assumed to be converged and we proceed to sample for the next image. For $\delta = 0.1$, 1, and 10, the Monte Carlo procedure required 56, 25, and 42 iterations, respectively, to reach convergence.

This prescription generates the MFEP [36]. Alternatively, the tangent to the string may follow the mean drift from swarms-of-trajectories, [37], In the string method with swarms-of-trajectories the mean displacement is [30], $\langle \Delta \mathbf{z}(\tau) \rangle_{\mathbf{z}} \approx -\mathbf{D}\,\boldsymbol{\nabla} W(\mathbf{z})$, where the diffusion tensor is, $\mathbf{D} = \langle \Delta \mathbf{z}(\tau) : \Delta \mathbf{z}(0) \rangle / 2\tau$. A third prescription is if the tangent follows the reactive flux density $\mathbf{J}_{AB}(\mathbf{z}) = \mathbf{D}\nabla q(\mathbf{z})$ [39]. Finally, the tangent of the curve many simply follow the gradient of the committor $\boldsymbol{\nabla} q(\mathbf{z})$.

It is of interest to be able to relate these different directions to the possible eigenvectors that can be defined at the saddle point of the 2D-BS potential. Let $[\mathbf{H}]_{ij} \equiv H_{ij}$ be the second-derivative (Hessian) matrix at the saddle point. The two principal axis of the potential at the saddle point are determined from the eigenvalue problem,

$$\lambda \mathbf{v} = \mathbf{H} \mathbf{v}, \tag{3.13}$$
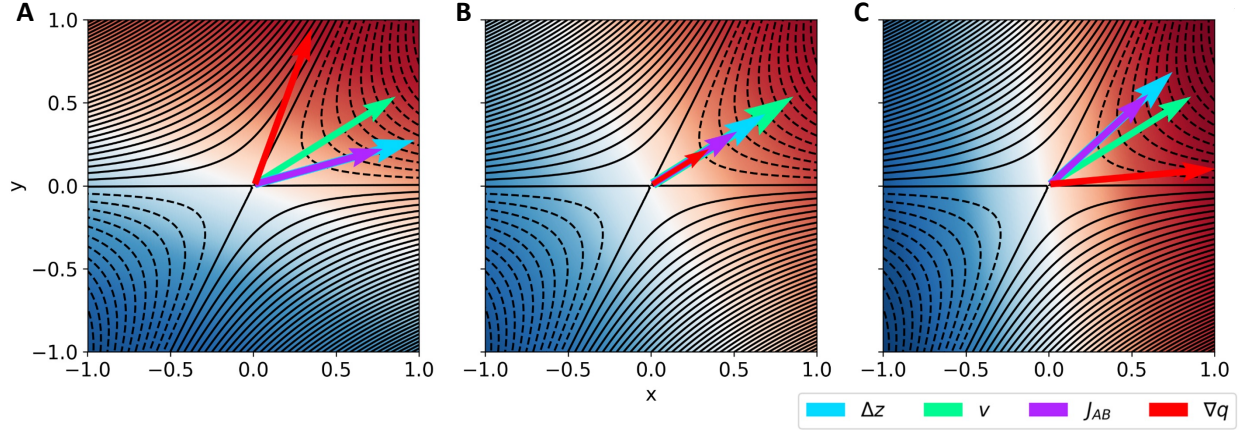
Figure 3.4: Comparison of selected eigenvectors computed from the diffusion matrix and Hessian. (A) $\delta = 0.1$. (B) $\delta = 1$. (C) $\delta = 10$. For each diffusion condition, we show the directions of the principal component of the Hessian matrix $\mathbf{V}$ (green), the overall reactive flux $\mathbf{J}_{AB}$ (purple), the mean drift $\mathbf{z}$ (blue), and $\boldsymbol{\nabla}q$ (red).

where λ is the eigenvalue. One can also define the tangent of a string that would be directed along the mean drift of a swarms-of-trajectory. The drift $\Delta \mathbf{z} = \tau\, \mathbf{DF} k_B T$ where $\mathbf{F}$ is the force. Assuming that the system is slightly displaced from the saddle point, by $\Delta \mathbf{z}$, then we have $\mathbf{F} = -\mathbf{H}\, \Delta \mathbf{z}$. It follows that, in the swarms-of-trajectory string, the tangent of the path is defined by the eigenvalue problem,

$$\mu\, \Delta \mathbf{z} \;=\; \mathbf{D}\,\mathbf{H}\, \Delta \mathbf{z}, \tag{3.14}$$

where μ is the eigenvalue. Finally, the gradient of the committor is defined by the eigenvalue problem,

$$\eta\, \mathbf{e} \;=\; \mathbf{H}\,\mathbf{D}\,\mathbf{e}, \tag{3.15}$$

where η is the eigenvalue. In the case of anisotropic diffusion, we can see that the eigenvectors of the matrices $\mathbf{H}$, $\mathbf{DH}$, and $\mathbf{HD}$ will differ. Fig. 3.4 illustrates the eigenvectors computed from $\mathbf{D}$ and $\mathbf{H}$. The selected eigenvectors shown correspond to meaningful pro-

cesses: $\mathbf{v}$ points in the overall direction of the slow process, $\boldsymbol{\nabla}q$ points in the direction of the committor-consistent optimized string, whereas $\Delta \mathbf{z}$ and $\mathbf{J}_{AB}$ both point along the isocommittor surface. While different constructs can provide useful information about the overall mechanism of a conformation transition pathway, they do not all provide a meaningful reaction coordinates. For instance, Berezhkovskii and Szabo showed that in the case of a multidimensional activated process controlled by diffusion, using a one-dimensional coordinate parallel to the gradient of the committor at the saddle point, $\boldsymbol{\nabla}q(\mathbf{z}^{\dagger})$, yields a result that is consistent with the multidimensional Kramers-Langer theory [106]. Projection onto any other one-dimensional coordinates yields an incorrect result. Furthermore, it was shown recently that $\boldsymbol{\nabla}q(\mathbf{z}^{\dagger})$ indeed represents the best choice to determine the direction of an effective one-dimensional reaction coordinate [31]. Although such formal results are informative, they cannot be trivially translated into a practical algorithm to determine a transition pathway, as the committor is itself a complicated probability requiring *in principle* one to compile the outcome of multiple shooting trajectories initiated from different positions. Ultimately, optimizing a curvilinear path according to the committor variational principle yields the most effective tool to represent the slow transition. See Chapter 3.5.8 of the Appendix for further details.

3.3.3 Alanine Dipeptide and Enhanced Sampling

The simulation used for the study of the 2D-BS potential was sufficiently long to provide an equilibrium sampling. However, this may not always be feasible due to the long-lived timescales of many systems of interest and compounded by the large computational overhead in order to simulate the rare events. Here we apply the committor-consistent string method to the N–acetyl–N–methyl–L–alanylamide molecule, commonly known as the alanine dipeptide (or dialanine), to study the conformational transition between $C_{7\text{eq}}$ and $C_{7\text{ax}}$ in vacuum at room temperature.
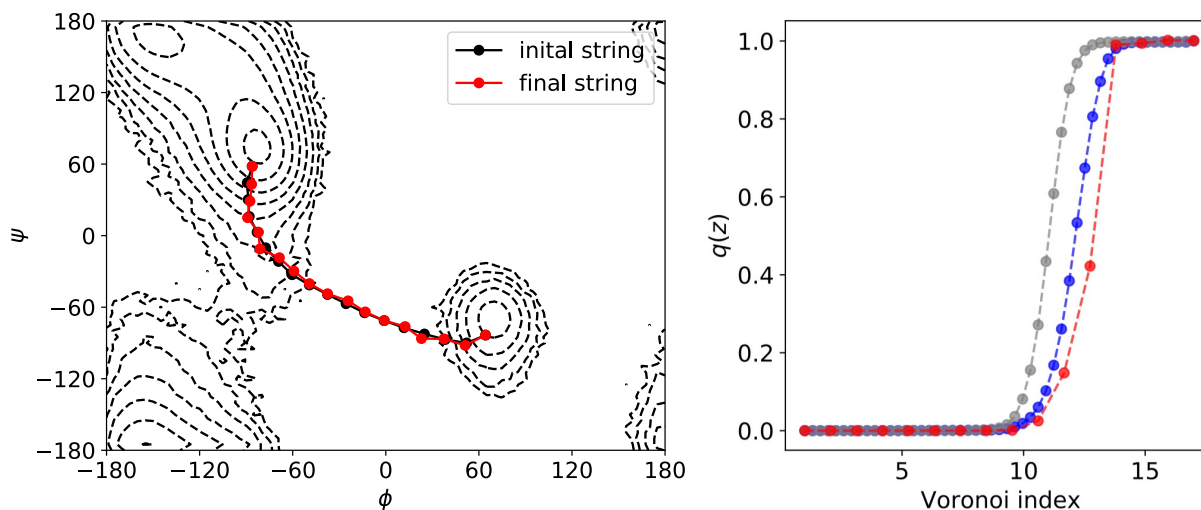
Figure 3.5: Variational string method implemented for the dialanine. The initial string (black) consists of straight paths connecting the local minima while the final string (red) is obtained by variationally minimizing the committor-correlation function. The committor probability of this final string (red) increases from 0 to 1 with a steep curve at the transition barrier. The position of the images was optimized by minimizing the committor time-correlation function using the iterative Monte Carlo procedure with random moves over a box $1.0° \times 1.0°$. The Monte Carlo optimized string and q is compared with results from PCV using a string following the mean force (blue) and string method with swarms of trajectories (gray).

To initiate the pathway optimization, enhanced sampling was performed with an adaptive biasing force acting along an initial string, used to define the progress collective variable (PCV) s [101]. Two different strings were considered to define the PCV in the $\phi - \psi$ plane: the MFEP from a 5 μs unbiased trajectory and the mean drifts from swarms-of-trajectories [37]. Nevertheless, these two strings are fairly similar qualitatively, and also yield similar values of ΔG (2.3 kcal/mol for the black string and 1.9 kcal/mol for the red string shown in Appendix Fig. 3.12). Then, defining the variable s between the strings from the above two methods, a reaction tube of starting points was chosen from the biased trajectories to run additional unbiased simulations for the computation of q (Appendix Fig. 3.13). The optimized string after 20 iterations is shown in Fig. 3.5.

Because of the isotropic nature of ϕ and ψ dihedral angles, the committor-consistent string remained close to the initial MFEP string. The committor $q(\mathbf{z})$ calculated along the optimized string from Eqs. (3.7) and (3.11) is very similar to that calculated from the potential of mean force along the PCV. In particular, the halfway crossing at $q(\mathbf{z}) = 0.5$ agrees relatively well, although with a somewhat steeper slope. Compared to the PCV by the string method with swarms-of-trajectories, the top of the free energy barrier is slightly shifted, which is expected since the initial strings were different.

3.3.4   Coarse-Grained Model of Barstar-Barnase Binding

We have implemented the committor-consistent string method for the binding of the barstar-barnase complex. The coarse-grained (CG) model is the same as in a previous study of the time-dependent kinetic aspects of protein–protein association and dissociation based on the framework of Markov state models (MSM) [122]. Briefly, the CG representation maps each amino acid residue as a single bead with its mass and position corresponding to the Cα carbon atom. Attractive Lennard-Jones 6-12 potentials are used to represent four pair-wise contacts of the native complex to simulate the protein-protein association. Using a long

57
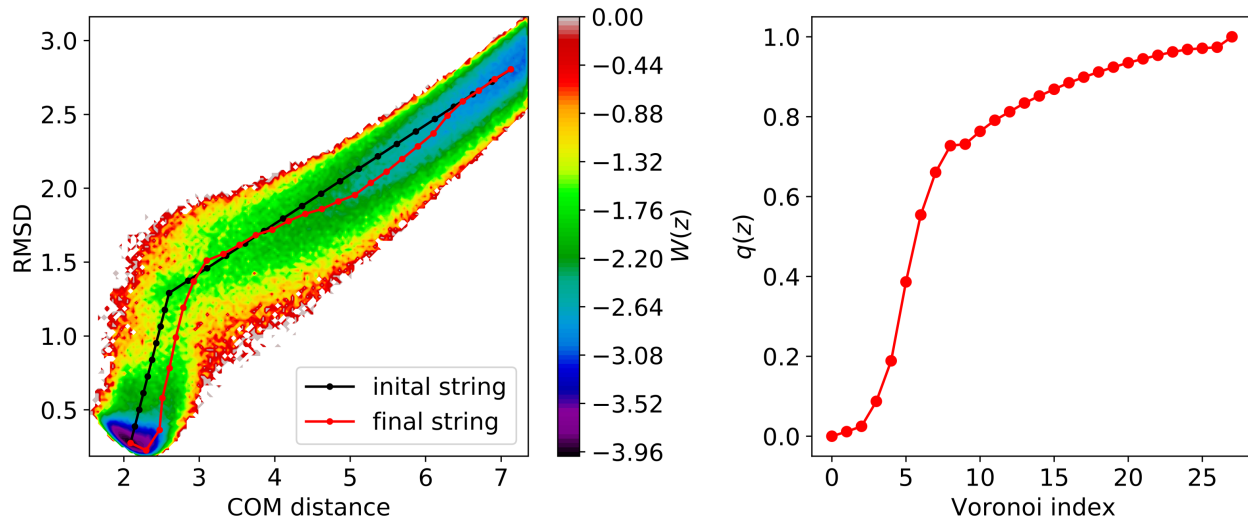
Figure 3.6: Variational string method implemented for the barnase-barstar complex. Left: The initial string (black) consists of straight paths connecting the local minima while the final string (red) is obtained by variationally minimizing the committor-correlation function. Right: The committor probability of the string increases from 0 to 1 relatively smoothly.

Langevin dynamics simulation generated previously [122], the string was optimized within a subspace of two order parameters, namely, the center-of-mass distance and the root-mean-square deviation (RMSD) of the contact residues. The optimization was initiated by starting from a straight path is shown in Fig. 3.6. Monte Carlo with random moves over the two order parameters (0.05×0.05) was carried out for a total of 80 iterations until convergence. Table 3.1 in the Appendix gives the rates of association and dissociation computed for different lag time τ. The rate constants k_{on} and k_{off} estimated from the steady-state reactive flux with the committor-consistent string at a lag time τ of 15 ns are $2.41 \times 10^{13} \mathring{A}^3 s^{-1}$ and $3.47 \times 10^7 s^{-1}$, respectively, which are close to the rates of $2.31 \times 10^{13} \mathring{A}^3 s^{-1}$ and $2.70 \times 10^7 s^{-1}$ from the MSM and Perron-cluster cluster analysis (PCCA) analysis with the six order parameters at the optimal MSM lag time of 12 ns [122]. The k_{on} and k_{off} values here are also close the MSM rates of $2.36 \times 10^{13} \mathring{A}^3 s^{-1}$ and $2.74 \times 10^7 s^{-1}$, respectively, with two order parameters at an optimal lag time of 12 ns.

3.4   Conclusion

An extension of the string method that produces an optimal reaction pathway following the gradient of the committor by variationally minimizing a committor time-correlation function was proposed. By representing the RC as a 1D curvilinear path embedded in the space of the CVs, the string provides a natural framework that simultaneously reduces the high dimensionality of the problem while retaining nonlinearity. By virtue of the Voronoi tessellation, the tangent of the optimized path from the committor-consistent string method follows the gradient of the committor ∇q. The committor probability is broadly viewed as an 'ideal' RC [123]. Furthermore, transition path analysis of two-state systems showed that the ideal 1D RC in a reduced subspace of coordinates is directed along the gradient of the committor ∇q [31], a choice that is also consistent with the multidimensional Kramers-Langer theory [106, 124]. This illustrates the clear advantage of a committor-consistent string over a more conventional MFEP-based string following the local mean force [36]. The images of the committor-consistent curvilinear string can be optimized by a Monte Carlo annealing method. In this algorithm, the string images are moved randomly in the CVs space and accepted or rejected based on the difference in likelihood. The present framework bears some similarities with previous methods [100, 125–129]. It is closest in spirit with the nonlinear RC analysis proposed by Bolhuis and coworkers whereby a string pathway is optimized via a maximum likelihood criterion to model the committor data obtained from a path sampling simulation [105]. It might be possible to combine the two approaches in a unifying framework to determine an optimal committor-based pathway.

A natural future direction would be to extend the approach to higher dimensional spaces. In this context, recent developments in ML techniques could help in choosing the best set of CVs and optimizing the string in their multidimensional space [130–133]. Another possible future work for this approach will be systems with more than two metastable states. Investigations in this direction would address the question as to whether we can predict the

correct order of states through which the string should pass, and whether we can discover more than one important reaction pathway.

3.5 Appendix: Theoretical Development

This Appendix section contains supplementary information and derivations that are relevant to the theory development of the committor-consistent variational string method presented in Chapter 3.

3.5.1 Effective Dynamical Propagator

To reduce the complexity of the problem, one typically seeks to determine the optimal pathway within the subspace of reduced dimension spanned by a subset of collective variables (CVs), $\tilde{\mathbf{z}}(\mathbf{x}) = (\tilde{z}_1(\mathbf{x}), \ldots, \tilde{z}_N(\mathbf{x}))$, i.e. a vector-valued function that maps every configuration $\mathbf{x}$ of the system on a set of values $\tilde{\mathbf{z}}(\mathbf{x})$. In this context, the string represents the pathway linking the states A and B as a discrete "chain of state", i.e., a collection of M images located at the positions $\{\mathbf{z}^1, \ldots, \mathbf{z}^M\}$ in the subspace of the CVs. To characterize the string pathway, the long-time dynamics of the system within the subspace of the CVs is critical. The probability density of the system at time t is expressed as $\rho(\mathbf{z}; t)$. The forward propagation step $(\mathbf{z} \to \mathbf{z}')$ for the probability density from the time t to the time $t + \tau$ is,

$$\rho(\mathbf{z}'; t + \tau) = \int d\mathbf{z} \; \mathcal{P}_\tau(\mathbf{z}'|\mathbf{z}) \; \rho(\mathbf{z}; t) \tag{3.16}$$

It is assumed that the dynamics within the reduced subspace of the CVs is Markovian with a finite lag-time τ, and that the propagator obeys the Chapman-Kolmogorov equation, $\boldsymbol{\rho}(t + n\tau) = \boldsymbol{\mathcal{P}}_{n\tau} \cdot \boldsymbol{\rho}(t)$, with $\boldsymbol{\mathcal{P}}_{n\tau} = (\boldsymbol{\mathcal{P}}_\tau)^n$. It is assumed that the system is in equilibrium and that we have microscopic detailed balance, $\mathcal{P}_\tau(\mathbf{z}'|\mathbf{z}) \, \rho_{eq}(\mathbf{z}) = \mathcal{P}_\tau(\mathbf{z}|\mathbf{z}') \, \rho_{eq}(\mathbf{z}')$. Under these conditions, the effective propagator $\boldsymbol{\mathcal{P}}_\tau(\mathbf{z}'|\mathbf{z})$ yields a self-consistent representation of the dynamics of the system within this subspace (closure of the dynamical propagation).

3.5.2 Committor Probabilities for Two Metastable States

Assuming two metastable states A and B, the forward committor $q(\mathbf{z})$ is the sum of the probability over all paths starting at $\mathbf{z}$ that ultimately reach the state B before ever reaching the state A. The probability of each of these paths is expressed as a product of discrete propagation steps $\boldsymbol{\mathcal{P}}_{n\tau} \cdots \boldsymbol{\mathcal{P}}_{n\tau}$ with lag-time τ, under the restriction that the intermediate states resulting from all these steps are $\notin A, B$. It follows that $q(\mathbf{z})$ is written explicitly as,

$$
\begin{aligned}
q(\mathbf{z}) &= \int_{\in B} d\mathbf{z}'\, \mathcal{P}_\tau(\mathbf{z}'|\mathbf{z}) + \int_{\notin A,B} d\mathbf{z}' \int_{\in B} d\mathbf{z}''\, \mathcal{P}_\tau(\mathbf{z}''|\mathbf{z}')\, \mathcal{P}_\tau(\mathbf{z}'|\mathbf{z}) \\
&\qquad + \int_{\notin A,B} d\mathbf{z}' \int_{\notin A,B} d\mathbf{z}'' \int_{\in B} d\mathbf{z}'''\, \mathcal{P}_\tau(\mathbf{z}'''|\mathbf{z}'')\, \mathcal{P}_\tau(\mathbf{z}''|\mathbf{z}')\, \mathcal{P}_\tau(\mathbf{z}'|\mathbf{z}) \qquad + \ldots \\
&= \int_{\in B} d\mathbf{z}'\, \mathcal{P}_\tau(\mathbf{z}'|\mathbf{z}) + \int_{\notin A,B} d\mathbf{z}' \Bigg\{ \int_{\in B} d\mathbf{z}''\, \mathcal{P}_\tau(\mathbf{z}''|\mathbf{z}') \\
&\qquad + \int_{\notin A,B} d\mathbf{z}'' \int_{\in B} d\mathbf{z}'''\, \mathcal{P}_\tau(\mathbf{z}'''|\mathbf{z}'')\, \mathcal{P}_\tau(\mathbf{z}''|\mathbf{z}') + \ldots \Bigg\} \mathcal{P}_\tau(\mathbf{z}'|\mathbf{z}) \\
&= 0 + \int_{\in B} d\mathbf{z}'\, \mathcal{P}_\tau(\mathbf{z}'|\mathbf{z}) + \int_{\notin A,B} d\mathbf{z}' \left\{ q(\mathbf{z}') \right\} \mathcal{P}_\tau(\mathbf{z}'|\mathbf{z}) \\
&= \int_{\in A} d\mathbf{z}' \left\{ 0 \right\} + \int_{\in B} d\mathbf{z}' \left\{ 1 \right\} \mathcal{P}_\tau(\mathbf{z}'|\mathbf{z}) + \int_{\notin A,B} d\mathbf{z}' \left\{ q(\mathbf{z}') \right\} \mathcal{P}_\tau(\mathbf{z}'|\mathbf{z}) \\
&= \int_{\in A} d\mathbf{z}'\, q(\mathbf{z}') + \int_{\in B} d\mathbf{z}'\, q(\mathbf{z}')\, \mathcal{P}_\tau(\mathbf{z}'|\mathbf{z}) + \int_{\notin A,B} d\mathbf{z}'\, q(\mathbf{z}')\, \mathcal{P}_\tau(\mathbf{z}'|\mathbf{z}) \\
&= \int d\mathbf{z}'\, q(\mathbf{z}')\, \mathbf{P}_\tau(\mathbf{z}'|\mathbf{z})
\end{aligned}
$$

(3.17)

(3.18)

with the constraints $q(\mathbf{z}) = 0$ if $\mathbf{z} \in A$, and $q(\mathbf{z}) = 1$ if $\mathbf{z} \in B$. By construction, $0 \leq q(\mathbf{z}) \leq 1$. While the equations for the committor probabilities involve only the elementary propagator $\mathcal{P}_\tau(\mathbf{z}'|\mathbf{z})$ for the lag-time τ, the fundamental validity of these equations is predicated upon the necessity to satisfy Markovity of the dynamics as expressed by the Chapman-Kolmogorov equation, $\boldsymbol{\mathcal{P}}_{n\tau} \equiv (\boldsymbol{\mathcal{P}}_\tau)^n$.

3.5.3   Net Forward Flux from Reactive Pathways

We deliberately define the boundary states A and B, and we divide the subspace of CVs in a region A' that includes the state A and a region B' that includes the state B. We can express the net forward reactive flux the local transitions $\mathbf{z} \to \mathbf{z}'$ by considering a trajectory $\{\mathbf{z}(t)$ of length T, $[24, 26, 30, 32]$

$$
\begin{aligned}
J_{AB} &= \lim_{T \to \infty} \frac{1}{T} \int_0^T \int_{\mathbf{z} \in A'} d\mathbf{z} \int_{\mathbf{z}' \in B'} d\mathbf{z}' \; \mathbf{1}_{\mathbf{z}(t) \in R} \; \frac{\delta(\mathbf{z}' - \mathbf{z}(t+\tau)) \, \delta(\mathbf{z} - \mathbf{z}(t))}{\tau} \\
&= \int_{\mathbf{z} \in A'} d\mathbf{z} \int_{\mathbf{z}' \in B'} d\mathbf{z}' \; \left\langle j_{AB}^R(\mathbf{z}', \mathbf{z}) \right\rangle
\end{aligned}
\tag{3.19}
$$

where $\mathbf{1}_{\mathbf{z}(t) \in R} = 1$ if at time t, $\mathbf{z}(t)$ belongs to an AB reactive path, and $\mathbf{1}_{\mathbf{z}(t) \in R} = 0$ otherwise, and $\langle j_{AB}^R(\mathbf{z}', \mathbf{z}) \rangle$ represent the mean net number of transition from $\mathbf{z}$ to $\mathbf{z}'$ per unit of time τ contributed by reactive trajectories. To construct $\langle j_{AB}^R(\mathbf{z}', \mathbf{z}) \rangle$, we rely on the committor probability defined in Eq. (3.18) that a trajectory started at $\mathbf{z}$ will go to B before going to A, with the constraints $q(\mathbf{z}) = 0$ when $\mathbf{z} \in A$, and $q(\mathbf{z}) = 1$ when $\mathbf{z} \in B$. The net reactive current $\langle j_{AB}(\mathbf{z}', \mathbf{z}) \rangle$ from $\mathbf{z}$ to $\mathbf{z}'$ is obtained by summing over all reactive trajectories that actually make a transition from A to B. To construct a reactive trajectory that makes a transition from $\ddagger$ to $\ddagger'$, we have to consider the equilibrium probability to be in state $\mathbf{z}$, $\rho_{eq}(\mathbf{z})$, the probability that the piece of trajectory reaching $\mathbf{z}$ came from A, $(1 - q(\mathbf{z}))$, and the probability that the piece of trajectory after leaving $\mathbf{z}'$ will go on to to B, $q(\mathbf{z}')$. This yields $q(\mathbf{z}') \, \mathcal{P}_\tau(\mathbf{z}'|\mathbf{z}) \, (1 - q(\mathbf{z})) \, \rho_{eq}(\mathbf{z})$. To obtain the net flux from $\mathbf{z}$ to $\mathbf{z}'$, we have to subtract the reverse reactive transition from $\mathbf{z}'$ to $\mathbf{z}$, by considering the equilibrium probability to be in $\mathbf{z}'$, $\rho_{eq}(\mathbf{z}')$, the probability that the piece of trajectory reaching $\mathbf{z}'$ came from A, $(1 - q(\mathbf{z}))$, and the probability that the piece of trajectory after leaving $\mathbf{z}$ will lead to B, $q(\mathbf{z})$. This yields, $q(\mathbf{z}) \, \mathcal{P}_\tau(\mathbf{z}|\mathbf{z}') \, (1 - q(\mathbf{z}')) \, \rho_{eq}(\mathbf{z}')$. The resulting net probability current

of the reactive trajectories between $\mathbf{z}$ and $\mathbf{z}'$ is thus,

$$\left\langle j_{AB}^R(\mathbf{z}',\mathbf{z}) \right\rangle = \frac{1}{\tau}\Big[q(\mathbf{z}') \, \mathcal{P}_\tau(\mathbf{z}'|\mathbf{z}) \left(1 - q(\mathbf{z})\right) \rho_{eq}(\mathbf{z}) - q(\mathbf{z}) \, \mathcal{P}_\tau(\mathbf{z}|\mathbf{z}') \left(1 - q(\mathbf{z}')\right) \rho_{eq}(\mathbf{z}') \Big]$$

invoking microscopic detailed balance, we have,

$$\begin{aligned}
\left\langle j_{AB}^R(\mathbf{z}',\mathbf{z}) \right\rangle \tau &= q(\mathbf{z}') \, \mathcal{P}_\tau(\mathbf{z}'|\mathbf{z}) \left(1 - q(\mathbf{z})\right) \rho_{eq}(\mathbf{z}) - q(\mathbf{z}) \, \mathcal{P}_\tau(\mathbf{z}'|\mathbf{z}) \left(1 - q(\mathbf{z}')\right) \rho_{eq}(\mathbf{z}) \\
&= q(\mathbf{z}') \, \mathcal{P}_\tau(\mathbf{z}'|\mathbf{z}) \, \rho_{eq}(\mathbf{z}) - q(\mathbf{z}') \, \mathcal{P}_\tau(\mathbf{z}'|\mathbf{z}) \, q(\mathbf{z}) \, \rho_{eq}(\mathbf{z}) \\
&\qquad + q(\mathbf{z}) \, \mathcal{P}_\tau(\mathbf{z}'|\mathbf{z}) \, q(\mathbf{z}') \, \rho_{eq}(\mathbf{z}) - q(\mathbf{z}) \, \mathcal{P}_\tau(\mathbf{z}'|\mathbf{z}) \, \rho_{eq}(\mathbf{z}) \\
&= q(\mathbf{z}') \, \mathcal{P}_\tau(\mathbf{z}'|\mathbf{z}) \, \rho_{eq}(\mathbf{z}) - q(\mathbf{z}') \, \mathcal{P}_\tau(\mathbf{z}'|\mathbf{z}) \, q(\mathbf{z}) \, \rho_{eq}(\mathbf{z}) \\
&\qquad + q(\mathbf{z}') \, \mathcal{P}_\tau(\mathbf{z}'|\mathbf{z}) \, q(\mathbf{z}) \, \rho_{eq}(\mathbf{z}) - \mathcal{P}_\tau(\mathbf{z}'|\mathbf{z}) \, q(\mathbf{z}) \, \rho_{eq}(\mathbf{z}) \\
&= q(\mathbf{z}') \, \mathcal{P}_\tau(\mathbf{z}'|\mathbf{z}) \, \rho_{eq}(\mathbf{z}) - \mathcal{P}_\tau(\mathbf{z}'|\mathbf{z}) \, q(\mathbf{z}) \, \rho_{eq}(\mathbf{z}) \\
&= \Big(q(\mathbf{z}') - q(\mathbf{z}) \Big) \, \mathcal{P}_\tau(\mathbf{z}'|\mathbf{z}), \rho_{eq}(\mathbf{z}) \qquad (3.20)
\end{aligned}$$

Hence,

$$J_{AB} = \frac{1}{\tau} \int_{\mathbf{z} \in A'} d\mathbf{z} \int_{\mathbf{z}' \in B'} d\mathbf{z}' \, \Big(q(\mathbf{z}') - q(\mathbf{z}) \Big) \, \mathcal{P}_\tau(\mathbf{z}'|\mathbf{z}) \, \rho_{eq}(\mathbf{z}) \qquad (3.21)$$

Equivalently, Eq. (3.21) can also be derived by considering the net unidirectional reactive flux from A to B under non-equilibrium steady-state conditions, [32]

$$\rho_{ss}(\mathbf{z}') = \int d\mathbf{z} \, \mathcal{P}_\tau(\mathbf{z}'|\mathbf{z}) \, \rho_{ss}(\mathbf{z}) \qquad (3.22)$$

with $\rho_{ss}(\mathbf{z}) = \rho_{eq}(\mathbf{z})$ if $\mathbf{z} \in A$ and $\rho_{ss}(\mathbf{z}) = 0$ if $\mathbf{z} \in B$. It can be verified by direct substitution in Eq. (3.22) that the steady-state density can be expressed as, $\rho_{ss}(\mathbf{z}) = \rho_{eq}(\mathbf{z}) \left(1 - q(\mathbf{z})\right)$, where $q(\mathbf{z})$ is the committor probability defined by Eq. (3.18) with the constraints $q = 0$ if

$\mathbf{z} \in A$, and $q = 1$ if $\mathbf{z} \in B$,

$$
\begin{aligned}
\rho_{eq}(\mathbf{z}') \left(1 - q(\mathbf{z}')\right) &= \int d\mathbf{z} \, \mathcal{P}_\tau(\mathbf{z}'|\mathbf{z}) \, \rho_{eq}(\mathbf{z}) \left(1 - q(\mathbf{z})\right) \\
\rho_{eq}(\mathbf{z}') \left(1 - q(\mathbf{z}')\right) &= \rho_{eq}(\mathbf{z}') - \int d\mathbf{z} \, \mathcal{P}_\tau(\mathbf{z}|\mathbf{z}') \, \rho_{eq}(\mathbf{z}') \, q(\mathbf{z}) \\
q(\mathbf{z}') &= \int d\mathbf{z} \, q(\mathbf{z}) \, \mathcal{P}_\tau(\mathbf{z}|\mathbf{z}')
\end{aligned}
\tag{3.23}
$$

where we used microscopic detailed balance.

3.5.4   Steady-State Flux Between the Two Metastable States

The steady-state flux from A to B can be expressed as the net transitions across a dividing surface separating the two sides, recovering Eq. (3.21),

$$
\begin{aligned}
J^{AB} &= \frac{1}{\tau} \int_{\mathbf{z} \in A'} d\mathbf{z} \int_{\mathbf{z}' \in B'} d\mathbf{z}' \left(\mathcal{P}_\tau(\mathbf{z}'|\mathbf{z}) \, \rho_{ss}(\mathbf{z}) - \mathcal{P}_\tau(\mathbf{z}|\mathbf{z}') \, \rho_{ss}(\mathbf{z}') \right) \\
&= \frac{1}{\tau} \int_{\mathbf{z} \in A'} d\mathbf{z} \int_{\mathbf{z}' \in B'} d\mathbf{z}' \left(\mathcal{P}_\tau(\mathbf{z}'|\mathbf{z}) \, \rho_{eq}(\mathbf{z}) \left(1 - q(\mathbf{z})\right) - \mathcal{P}_\tau(\mathbf{z}|\mathbf{z}') \, \rho_{eq}(\mathbf{z}') \left(1 - q(\mathbf{z}')\right) \right) \\
&= \frac{1}{\tau} \int_{\mathbf{z} \in A'} d\mathbf{z} \int_{\mathbf{z}' \in B'} d\mathbf{z}' \left(\mathcal{P}_\tau(\mathbf{z}|\mathbf{z}') \, \rho_{eq}(\mathbf{z}') \, q(\mathbf{z}') - \mathcal{P}_\tau(\mathbf{z}'|\mathbf{z}) \, \rho_{eq}(\mathbf{z}) \, q(\mathbf{z}) \right) \\
&= \frac{1}{\tau} \int_{\mathbf{z} \in A'} d\mathbf{z} \int_{\mathbf{z}' \in B'} d\mathbf{z}' \left(q(\mathbf{z}') - q(\mathbf{z}) \right) \mathcal{P}_\tau(\mathbf{z}'|\mathbf{z}) \, \rho_{eq}(\mathbf{z})
\end{aligned}
\tag{3.24}
$$

which recovers Eq. (3.21). Because the steady-state flux J^{AB} in Eq. (3.21) does not depend on the position of the dividing surface defining the A' and B' regions, it is convenient to choose a dividing surface corresponding to an isocommittor surface of $q(\mathbf{z})$ at some arbitrary value q^*. The flux from A to B can then be written as transitions from the point $\mathbf{z}$ with committor $q(\mathbf{z}) < q*$, to the point $\mathbf{z}'$ with committor $q(\mathbf{z}') > q^*$,

$$
\begin{aligned}
J^{AB}(q^*) &= \frac{1}{\tau} \int d\mathbf{z} \int d\mathbf{z}' \, \theta\big(q(\mathbf{z}') - q^*\big) \, \theta\big(q^* - q(\mathbf{z})\big) \\
&\qquad\qquad \big(q(\mathbf{z}') - q(\mathbf{z})\big) \mathcal{P}_\tau(\mathbf{z}'|\mathbf{z}) \, \rho_{eq}(\mathbf{z})
\end{aligned}
\tag{3.25}
$$

However, one can also write,

$$J^{AB} = \int_0^1 dq^* \, J^{AB}(q^*) \tag{3.26}$$

because the steady-state flux $J^{AB}(q^*)$ does not actually depend on the specific value of q^*, which can be demonstrated by showing that there is no accumulation of probability in the region between the states A and B. [39] Carrying out the integration in the expression above affects only the term,

$$\int_0^1 dq^* \, \theta\big(q(\mathbf{z}') - q^*\big) \, \theta\big(q^* - q(\mathbf{z})\big) \;=\; \Big(q(\mathbf{z}') - q(\mathbf{z})\Big) \, \theta\big(q(\mathbf{z}') - q(\mathbf{z})\big) \tag{3.27}$$

yield the quadratic expression

$$
\begin{aligned}
J^{AB} &= \frac{1}{\tau} \int d\mathbf{z} \int d\mathbf{z}' \, \theta\big(q(\mathbf{z}') - q(\mathbf{z})\big) \Big(q(\mathbf{z}') - q(\mathbf{z})\Big)^2 \mathcal{P}_\tau(\mathbf{z}'|\mathbf{z}) \, \rho_{\mathrm{eq}}(\mathbf{z}) \\
&= \frac{1}{2\tau} \int d\mathbf{z} \int d\mathbf{z}' \, \Big(q(\mathbf{z}') - q(\mathbf{z})\Big)^2 \mathcal{P}_\tau(\mathbf{z}'|\mathbf{z}) \, \rho_{\mathrm{eq}}(\mathbf{z}) \\
&= \frac{1}{2\tau} \big\langle (q(\tau) - q(0))^2 \big\rangle
\end{aligned}
\tag{3.28}
$$

(the factor of 2 is needed when the restriction $q(\mathbf{z}') > q(\mathbf{z})$ is removed). An integration of the step-functions analogous to Eq. (3.27) was previously used by Krivov in a different situation. [107] A similar steady-state flux expression, quadratic in the committor difference, has also appeared in the context of discrete-state Markov models. [118]

3.5.5 Variational Principle and Committor

The quadratic expression for the reactive flux J_{AB} from Eqs. (3.28) can serve as a robust variational principle to optimize a trial committor $q(\mathbf{z}')$. Minimizing the quantity J_{AB} with respect to the trial function $q(\mathbf{z})$ yields,

$$
\begin{aligned}
0 &= \frac{\delta J_{AB}[q]}{\delta q(\mathbf{z''})} \\
0 &= \frac{1}{2\tau} \int d\mathbf{z} \int d\mathbf{z'} \left(q(\mathbf{z'}) - q(\mathbf{z}) \right) \mathcal{P}_\tau(\mathbf{z'}|\mathbf{z}) \, \rho_{\mathrm{eq}}(\mathbf{z}) \left(\delta(\mathbf{z'} - \mathbf{z''}) - \delta(\mathbf{z} - \mathbf{z''}) \right) \\
0 &= \int d\mathbf{z} \left(q(\mathbf{z''}) - q(\mathbf{z}) \right) \mathcal{P}_\tau(\mathbf{z''}|\mathbf{z}) \, \rho_{\mathrm{eq}}(\mathbf{z}) - \int d\mathbf{z'} \left(q(\mathbf{z'}) - q(\mathbf{z''}) \right) \mathcal{P}_\tau(\mathbf{z'}|\mathbf{z''}) \, \rho_{\mathrm{eq}}(\mathbf{z''}) \\
0 &= 2\, \rho_{\mathrm{eq}}(\mathbf{z''}) \int d\mathbf{z} \left(q(\mathbf{z''}) - q(\mathbf{z}) \right) \mathcal{P}_\tau(\mathbf{z}|\mathbf{z''}) \\
0 &= \int d\mathbf{z} \left(q(\mathbf{z''}) - q(\mathbf{z}) \right) \mathcal{P}_\tau(\mathbf{z}|\mathbf{z''}) \quad\quad\quad\quad\quad\quad\quad (3.29)
\end{aligned}
$$

which recovers by Eq. (3.18)

$$
q(\mathbf{z''}) = \int d\mathbf{z}\, q(\mathbf{z}) \, \mathcal{P}_\tau(\mathbf{z}|\mathbf{z''}) \quad\quad\quad\quad\quad\quad\quad (3.30)
$$

that formally defines the committor probability.

3.5.6   Committor Expressed in Terms of a Basis Set Expansion

Minimization of the steady-state flux J_{AB} defined by Eq. (3.28) for a trial function q with the constraints $q(\mathbf{z}) = 0$ if $\mathbf{z} \in A$, and $q(\mathbf{z}) = 1$ if $\mathbf{z} \in B$ yields the correct committor $q(\mathbf{z})$, defined by Eq. (3.30). As with the spectral decomposition, we will seek to express the trial function $q(\mathbf{z})$ in terms of a basis set expansion. However, the construction of the trial function requires special care to handle the constraints imposed by the boundary states. Here, we write the committor as

$$
q(\tilde{\mathbf{z}}(\mathbf{x})) = h_A(\tilde{\mathbf{z}}(\mathbf{x}))\, q_A + h_I(\tilde{\mathbf{z}}(\mathbf{x})) \left(\sum_i b_i\, f_i(\tilde{\mathbf{z}}(\mathbf{x})) \right) + h_B(\tilde{\mathbf{z}}(\mathbf{x}))\, q_B \quad\quad (3.31)
$$

where $q_A = 0$ and $q_B = 1$, and h_A, h_B, and h_I are indicator functions correspondingly equal to 1 when the system in the boundary states A, and B or intermediate region, and zero

otherwise. By construction, $h_A + h_I + h_B = 1$, and all cross product of indicator functions is identically zero ($h_A h_I = h_A h_B = h_I h_B = 0$) because there is no overlap between the 3 different regions. Using the trial function Eq. (3.31) with the time-correlation function,

$$\langle q(\tau)q(0)\rangle = \left\langle \left(h_I(\tau) \left(\sum_i b_i \, f_i(\tau) \right) + h_B(\tau) \right) \left(h_I(0) \left(\sum_j b_j \, f_j(0) \right) + h_B(0) \right) \right\rangle$$

$$= \sum_{ij} b_i \, b_j \, \langle h_I(\tau) \, h_I(0) \, f_i(\tau) \, f_j(0)\rangle + \sum_i b_i \, \langle h_I(\tau) h_B(0) \, f_i(\tau)\rangle$$

$$+ \sum_j b_j \langle h_I(0) \, h_B(\tau) \, f_j(0)\rangle + \langle h_B(\tau) h_B(0)\rangle$$

$$\langle q(0)q(0)\rangle - \langle q(\tau)q(0)\rangle = \frac{1}{2} \mathbf{b}^t \left(\mathbf{D}(0) - \mathbf{D}(\tau) \right) \mathbf{b} + \left(\mathbf{g}(0) - \mathbf{g}(\tau) \right) \cdot \mathbf{b} \tag{3.32}$$

$$+ \left(\langle h_B(0) h_B(0)\rangle - \langle h_B(0) h_B(\tau)\rangle \right) \tag{3.33}$$

where

$$D_{ij}(\tau) = \langle h_I(0) \, h_I(\tau) \, f_i(0) \, f_j(\tau)\rangle + \langle h_I(0) \, h_I(\tau) \, f_j(0) \, f_i(\tau)\rangle \tag{3.34}$$

and

$$g_i(\tau) = \langle h_I(\tau) \, h_B(0) \, f_i(\tau)\rangle + \langle h_I(0) \, h_B(\tau) \, f_i(0)\rangle \tag{3.35}$$

Taking the derivative with respect to the basis set coefficients b_i yields the linear system of equations,

$$\left(\mathbf{D}(0) - \mathbf{D}(\tau) \right) \mathbf{b} + \left(\mathbf{g}(0) - \mathbf{g}(\tau) \right) = 0 \tag{3.36}$$

with the simple solution,

$$\mathbf{b} = - \left(\mathbf{D}(0) - \mathbf{D}(\tau) \right)^{-1} \left(\mathbf{g}(0) - \mathbf{g}(\tau) \right) \tag{3.37}$$

3.5.7   Time-Correlation Functions and Enhanced Sampling

One possible effective strategy to improve the conformational sampling relevant to a slow A-B transition is to introduce a biasing potential along a progress variable (PV) s, expressed as a differentiable function of the CVs $\mathbf{z}$. In principle, the one-dimensional free-energy profile, or PMF, along s reflects the correct equilibrium propability of the configurations. It is important to note that it is not necessary for the function $s(\mathbf{z})$ to be a perfect reaction coordinate to be useful in practice. As long as it reasonable links the two end-states and passes through the kinetic bottleneck or saddle point along the transition pathway, the function $s(\mathbf{z})$ can serve as an effective progress variable to support an enhanced sampling strategy based on biased simulations. In the context of the string method, one example of such expressions has been suggested by Bran et al. [101] in terms of a weighted sum of Gaussian functions centered on the M images along the string.

$$\tilde{s}[\mathbf{z}] = \frac{\displaystyle\sum_{m=0}^{M} \left(\frac{m}{M}\right) \mathrm{e}^{-\lambda(\mathbf{z}-\mathbf{z}_m)^2}}{\displaystyle\sum_{m=0}^{M} \mathrm{e}^{-\lambda(\mathbf{z}-\mathbf{z}_m)^2}} \tag{3.38}$$

and

$$\tilde{\zeta}[\mathbf{z}] = -\frac{1}{\lambda} \ln \sum_{m=0}^{M} \mathrm{e}^{-\lambda(\mathbf{z}-\mathbf{z}_m)^2} \tag{3.39}$$

Other forms have also been considered based on more complicated functional forms. [119,120] If the images are ordered to meaningfully represent the progresss of the transition from A to B, then the variable $s(\mathbf{z};\lambda)$ will smoothly vary from 0 to 1. While the proposed PCV provide a useful tool in simple cases of reduced dimensionality, an important limitation of the functional form has been the fundamental reliance on the rank-ordering of the images along the string, which needs to be known prior to calculating the progress variable $s(\mathbf{z})$. In all these methods, the images are ordered along the string, $[0, 1, \ldots, m, \ldots, M]$ in a suite

that is meant to accurately represent the progress of the transition. However, if the images are poorly ordered or scrambled, the PCVs is pathologically ill-defined. In practice, this is exceedingly difficult to do for most complex cases. As a consequence, the naive image ordering along the string is not likely to correctly represent the steady progress of the A to B transition.

The numbering of images is a direct source of inaccuracies in the construction of the PCV. [101] Essentially, the image index, m/M, is used as a surrogate indicator of the progress of the transition along the string in Eq. (3.38). When the committor has been determined, this issue is resolved by substituting (m/M) in Eq. (3.38) by $q(\mathbf{z}_m)$, the actual value of the committor in the mth Voronoy cell calculated from the basis set expansion. As the committor progresses from with $q = 0$ to $q = 1$ along the transition, this procedure naturally order the suite of images in their correct sequence. While $s(\mathbf{z})$ represents the PCV, the ancillary variable $\zeta(\mathbf{z})$ may be construed as the radius of a tube that embraces the string, [134] and confines sampling in its vicinity. Both depend on λ, which serves as a smoothing parameter that should be related to the inverse of the mean-square deviation between two consecutive images. In principle, if M is very large and the density of centroid $\mathbf{z}_m$ is very high, one may want to carry out the enhanced sampling in the limit where λ is large, localizing the weighted sum to the individual images and its committor $q(\mathbf{z}_m)$. From this perspective, the function $s(\mathbf{z}; \lambda)$ as defined by Eq. (3.38) is revealed as a simple interpolation scheme to construct an approximation to the $\mathbf{z}$=dependent committor function $q(\mathbf{z})$ based on the discrete set of values $q(\mathbf{z}_m)$, with $m = 0, \ldots, M$. Other more sophisticated scheme may be considered, although it is not necessary for the function $s(\mathbf{z})$ to be a perfect reaction coordinate to effectively support an enhanced sampling strategy based on biased simulations.

To use the enhanced sampling for calculating the correlation function, we use the configurations generated by the biased ABF simulation directly as initial conditions to initiated an ensemble of unbiased trajectories. Because of the biasing ABF potential, those config-

70

urations are uniformly distributed with respect to the order parameter s, so the unbiased correlation function can be calculated as,

$$
\begin{aligned}
C_{qq}(\tau) &= \int d\mathbf{z} \int d\mathbf{z}' \left(\int_0^1 ds\, \delta(s - s[\mathbf{z}]) \right) q(\mathbf{z}')\, q(\mathbf{z})\, \mathcal{P}_\tau(\mathbf{z}'|\mathbf{z}) \rho_{\mathrm{eq}}(\mathbf{z}) \\
&= \int_0^1 ds \int d\mathbf{z} \int d\mathbf{z}'\, \delta(s - s[\mathbf{z}])\, q(\mathbf{z}')\, q(\mathbf{z})\, \mathcal{P}_\tau(\mathbf{z}'|\mathbf{z}) \rho_{\mathrm{eq}}(\mathbf{z}) \frac{\int d\mathbf{z}\, \delta(s - s[\mathbf{z}])\, \rho_{\mathrm{eq}}(\mathbf{z})}{\int d\mathbf{z}\, \delta(s - s[\mathbf{z}]) \rho_{\mathrm{eq}}(\mathbf{z})} \\
&= \int_0^1 ds\, \rho_{\mathrm{eq}}(s)\, \frac{\int d\mathbf{z} \int d\mathbf{z}'\, \delta(s - s[\mathbf{z}])\, q(\mathbf{z}')\, q(\mathbf{z})\, \mathcal{P}_\tau(\mathbf{z}'|\mathbf{z}) \rho_{\mathrm{eq}}(\mathbf{z})}{\int d\mathbf{z}\, \delta(s - s[\mathbf{z}]) \rho_{\mathrm{eq}}(\mathbf{z})} \\
&= \int_0^1 ds\, \rho_{\mathrm{eq}}(s)\, \langle q(\tau)\, q(0) \rangle_{(s)} \\
&= \sum_k \left(\frac{e^{-w(s_k)/k_B T}}{\sum_{k'} e^{-w(s_{k'})/k_B T}} \right) \langle q(\tau)\, q(0) \rangle_{(s_k)}
\end{aligned}
\tag{3.40}
$$

where the subscript s_k means that the k-th unbiased trajectory is initiated with $\tilde{s}[\mathbf{z}(\mathbf{t})] = s_k$ at $t = 0$. In practice when computing Eq. (3.40), we only keep trajectory information at time zero and time τ. In order to sufficiently cover the desired state space, this approach would necessitate numerous unbiased trajectories, and, depending on the system studied, may become impractical. To reduce computational effort and fully utilize all data from the trajectories, we can compute an ensemble of time averages. Thus, the correlation function would consist of the time average of each k-th unbiased trajectory at a time t and later time $t + \tau$, while still taking into account the weight of the k-th starting condition

$$
C_{qq}(\tau) = \sum_k \left(\frac{e^{-w(s_k)/k_B T}}{\sum_{k'} e^{-w(s_{k'})/k_B T}} \right) \langle q(t + \tau)\, q(t) \rangle_{(s_k)}
\tag{3.41}
$$

3.5.8 Eigenvectors at saddle point

Following Berezhkovskii and Szabo [106], we represent the top of the barrier located at $\mathbf{z} \equiv (x, y) = (0, 0)$ as a quadratic potential separating the states A and B, $W/k_B T = \frac{1}{2} \mathbf{z}^t\, \mathbf{H}\, \mathbf{z}$, where $\mathbf{H}$ is the Hessian (second-derivative matrix) at the saddle point. We are interested in

determining the different possible principal axes originating from the top of the barrier that are useful for monitoring the progress of the reaction. Those include: (1) the minimum free energy path (MFEP) [36], (2) the gradient of the committor [31], (3) the reactive flux [24,106], (4) and the mean drift from string method with swarms of trajectories [37].

The simplest case is the MFEP, which is independent of the diffusion matrix $\mathbf{D}$ and is simply related to the unstable mode of the matrix $\mathbf{H}$. To incorporate the effect of diffusive dynamics, we define the set of right-eigenvectors $\mathbf{f}_i$ as

$$\lambda_i \mathbf{f}_i = (-\mathbf{DH}) \, \mathbf{f}_i \tag{3.42}$$

with $\lambda_1 > 0$ for a single unstable mode growing in amplitude with time (all other λ_i are negative and correspond to stable modes relaxing to zero with time). This eigenvector was previously identified by Berezhkovskii and Szabo [106], as the unstable model $\mathbf{f}_+$ directed along the reactive flux $\mathbf{J}_{AB}$. There is also the set of associated orthogonal left-eigenvectors

$$\lambda_i \mathbf{e}_i^t = \mathbf{e}_i^t (-\mathbf{DH}) \tag{3.43}$$

or equivalently $\lambda_i \mathbf{e}_i = (-\mathbf{HD})\mathbf{e}_i$, as the matrices are symmetric with $\mathbf{H}^t \mathbf{D}^t = \mathbf{HD}$. The set of eigenvectors obeys the orthonormalization condition, $\delta_{ij} = (\mathbf{e}_i^t \cdot \mathbf{f}_j)$. The eigenvector $\mathbf{e}_1$ was identified by by Berezhkovskii and Szabo [106], as the unstable model $\mathbf{e}_+$ directed along the gradient of the committor $\boldsymbol{\nabla} q(\mathbf{z})$. This result is confirmed by an independent analysis based on a variational analysis of the committor time-correlation function [30]. If may be further verified that $\mathbf{J}_{AB}$ points in the direction of the vector $\mathbf{f}_+$ by considering the reactive flux expressed as, $\mathbf{J}_{AB} = \mathbf{D}\boldsymbol{\nabla} q(\mathbf{z})$ [24]. From this definition, we have that $\mathbf{J}_{AB} \propto (\mathbf{De}_+) \propto \mathbf{D}(\mathbf{HDe}_+) \propto (\mathbf{DH})\mathbf{De}_+ \propto (\mathbf{DH})\mathbf{J}_{AB}$. Because $\mathbf{J}_{AB} \propto (\mathbf{DH})\mathbf{J}_{AB}$, $\mathbf{J}_{AB}$ is parallel to $\mathbf{f}_+$ as previously noted [106].

Finally, we consider the mean drift in the context of the string method with swarms of

trajectories [37]. The Brownian Dynamics (BD) equation of motion is,

$$\dot{\mathbf{z}}(t) \quad = \quad -\frac{1}{k_B T} \mathbf{D} \, \boldsymbol{\nabla} W + \xi(t) \tag{3.44}$$

where $\boldsymbol{\xi}(t)$ is a Gaussian random noise with time-correlation $\langle \boldsymbol{\xi}(t) : \boldsymbol{\xi}(0) \rangle = 2\mathbf{D}\delta(t)$. Averaging out the random noise from the equation of motion yields,

$$\langle \dot{\mathbf{z}}(t) \rangle \quad = \quad (-\mathbf{D}\,\mathbf{H}) \, \langle \mathbf{z}(t) \rangle \tag{3.45}$$

Assuming the initial condition $\mathbf{z}_0$, we can write the time-dependent solution $\langle \mathbf{z}(t) \rangle$ as,

$$\langle \mathbf{z}(t) \rangle = \sum_i (\mathbf{e}_i^t \cdot \mathbf{z}_0) e^{\lambda_i t} \mathbf{f} f_i \tag{3.46}$$

This provides the solution for the mean drift $\langle \mathbf{z}(t) \rangle - \mathbf{z}(0) = \langle \Delta \mathbf{z}(t) \rangle$ from a swarm of stochastic BD trajectories [37]. In particular, once the stable modes have decayed after a time $t \to \tau$, the mean drift is dominated by the evolution of the unstable mode,

$$\langle \Delta \mathbf{z}(\tau) \rangle \to (\mathbf{e}_+^t \cdot \mathbf{z}_0) e^{\lambda_+ \tau} \mathbf{f}_+ \tag{3.47}$$

Thus, the mean drift from a swarm of trajectories in the neighborhood of the saddle point follows the direction of the unstable mode $\mathbf{f}_+$, as does the reactive flux $\mathbf{J}_{AB}$.

3.6   Appendix: Supplementary Figures

This Appendix section contains supplementary information relevant to the results presented in Chapter 3.
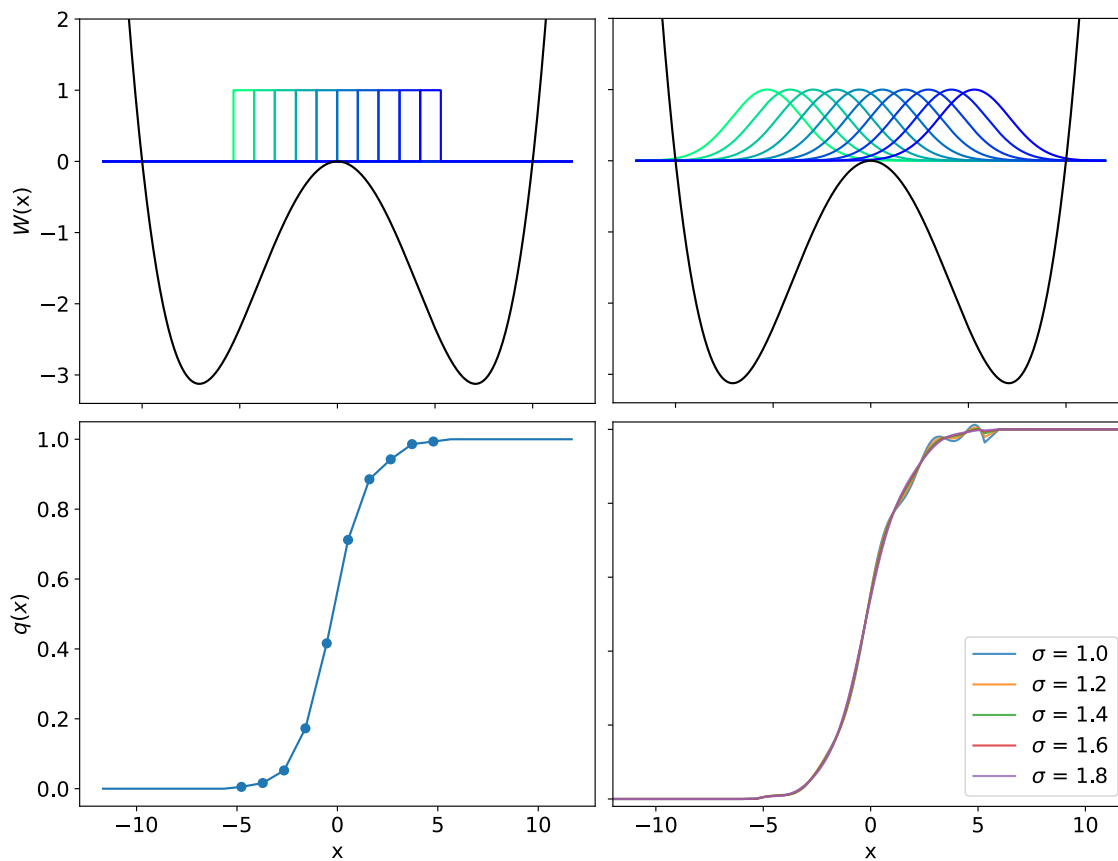
Figure 3.7: Illustration of basis set choices and committors with a 1-dimensional double well. Right column shows 10 one-hot indicator functions and the resulting committor. Left column shows 10 Gaussian functions and the estimated the committor.

To set up the committor-string method, we first define the boundary conditions for the committor and Voronoi tessellation along the string.
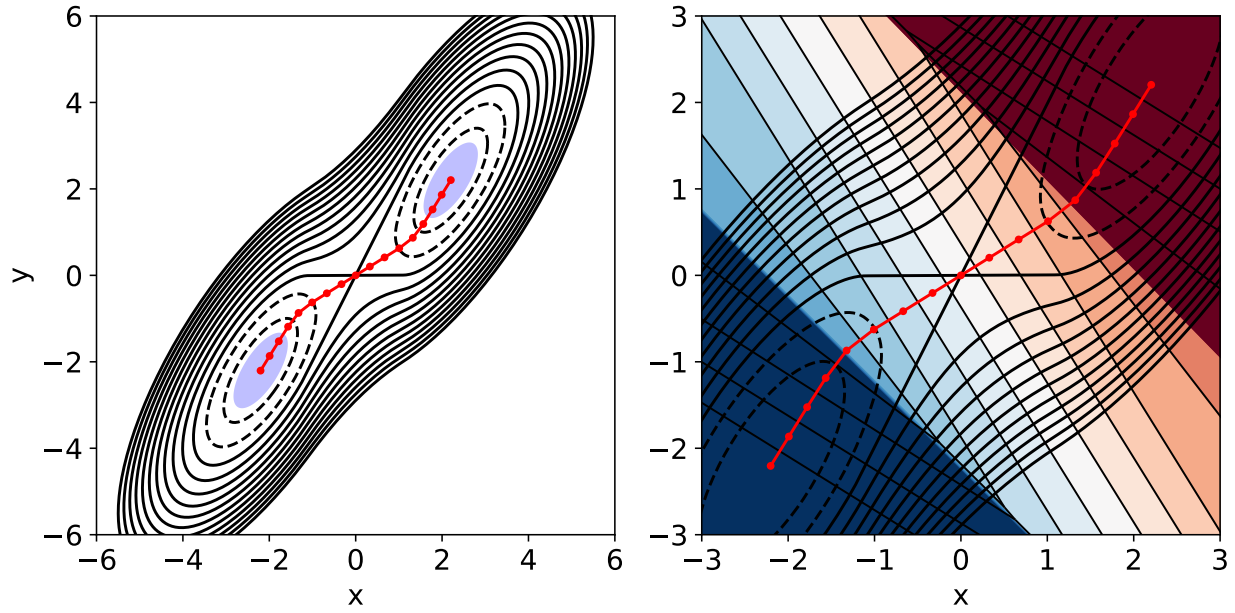
Figure 3.8: Refinement from the initial string. (a) Initial string is obtained following the local mean force. The purple shaded regions set the initial boundaries where $q = 0$ or 1. (b) Voronoi tessellation along the initial string.
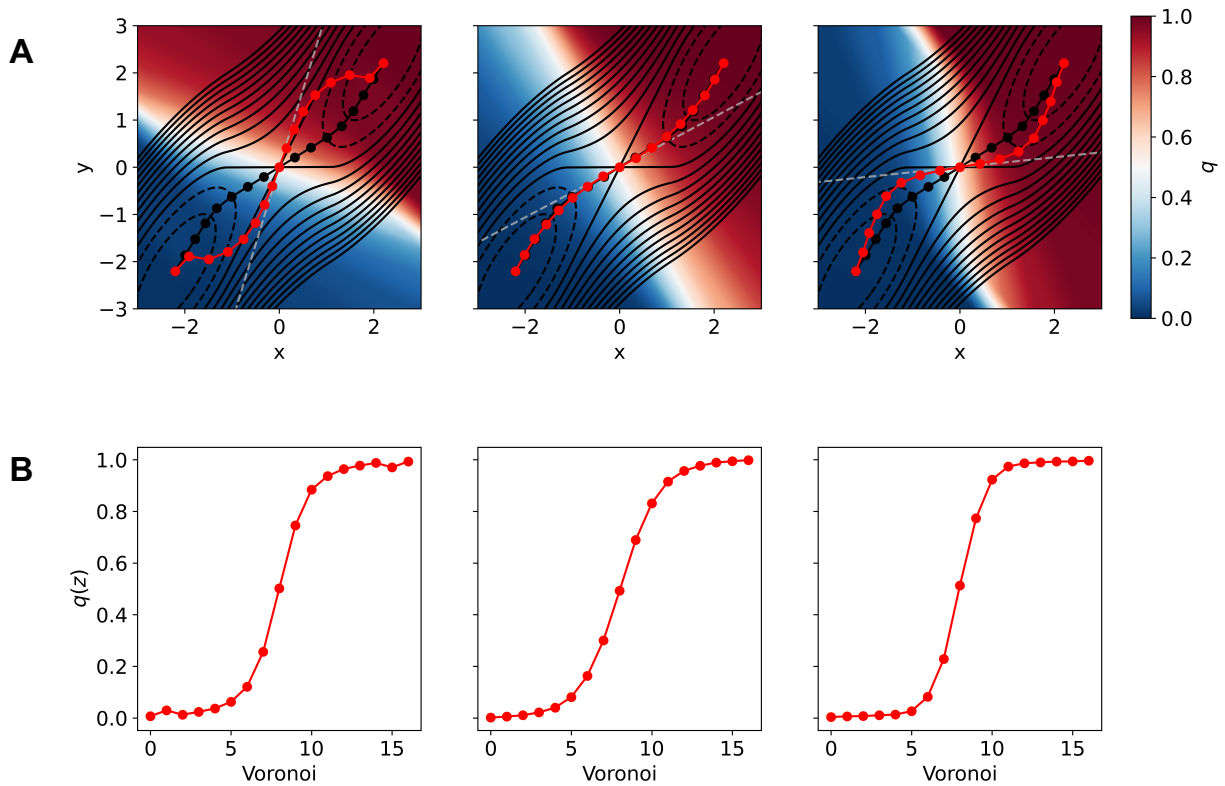
Figure 3.9: String optimized by variationally minimizing the correlation function with Monte Carlo sampling and the resulting committor probability for 3 diffusion conditions. (a) and (b) for $\delta = 0.1$, (c) and (d) for $\delta = 1$, and (e) and (f) for $\delta = 10$. For all cases, the initial string (black) follows the mean force of the potential. The final optimized strings (red) were generated by following the gradient of the committor. For comparison, also shown are the reaction coordinate paths (white dash) rotated at the best angle with respect to the x-axis that minimizes the committor correlation function.
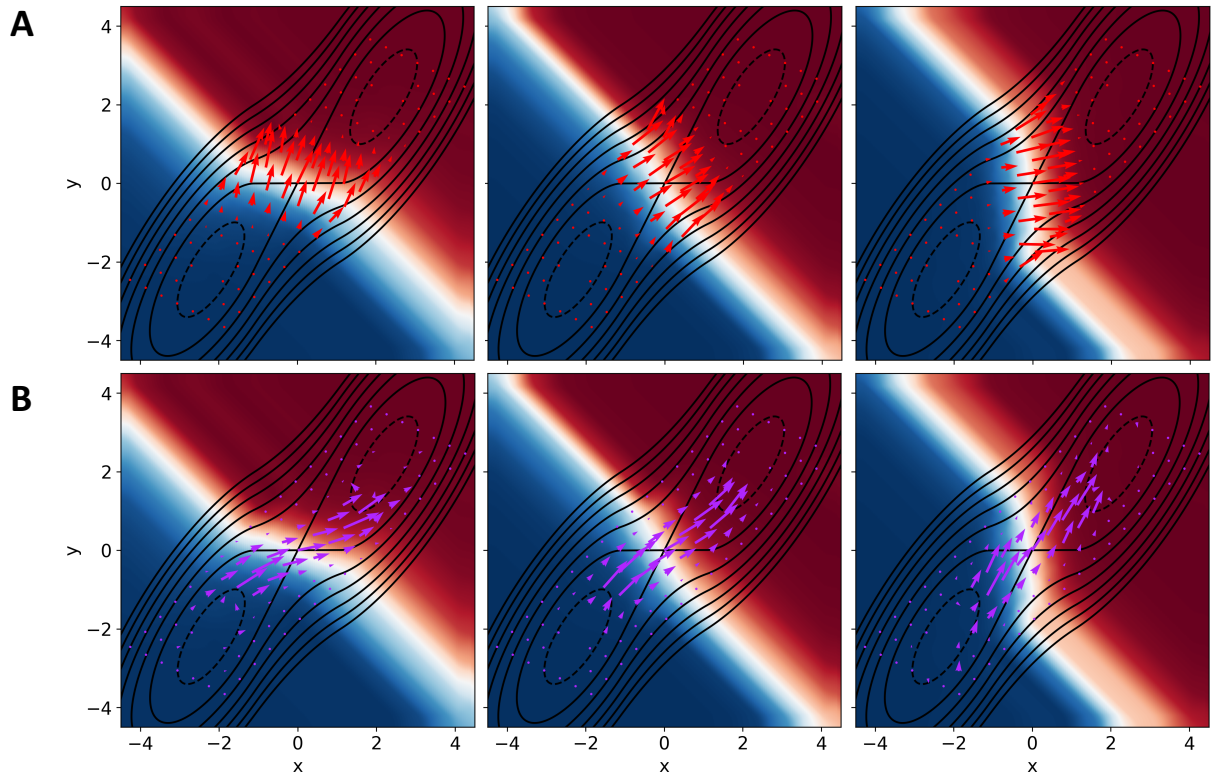
Figure 3.10: Reactive probability current density and the gradient of the committor throughout the potential. (a) $\nabla q(z)$ for $\delta = 0.1$, 1, and 10 from left to right. (b) $j_{AB}(z)$ for $\delta = 0.1$, 1, and 10.
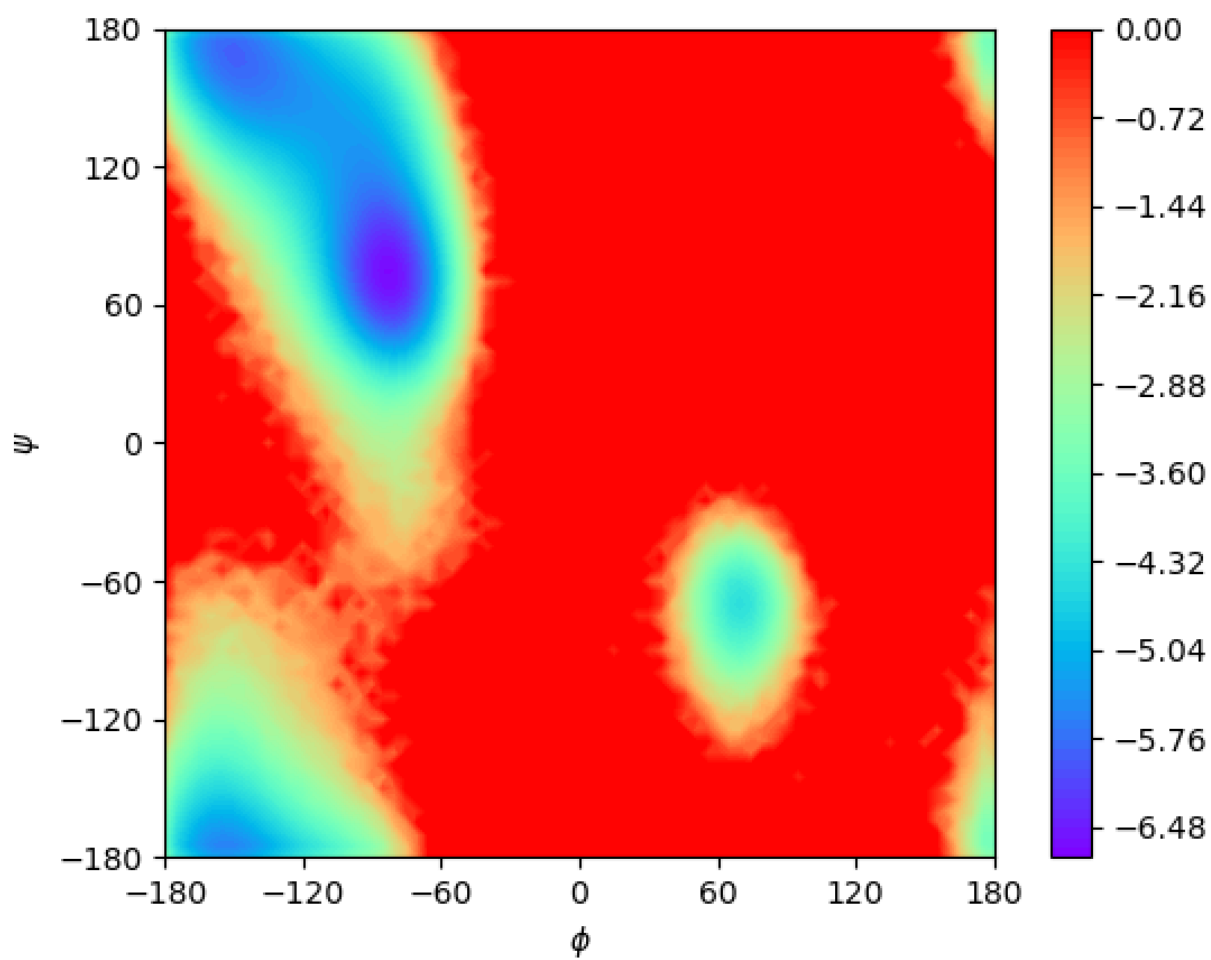
Figure 3.11: PMF of the alanine dipeptide in the ϕ, ϕ space from 5 microseconds of unbiased Langevin simulation.
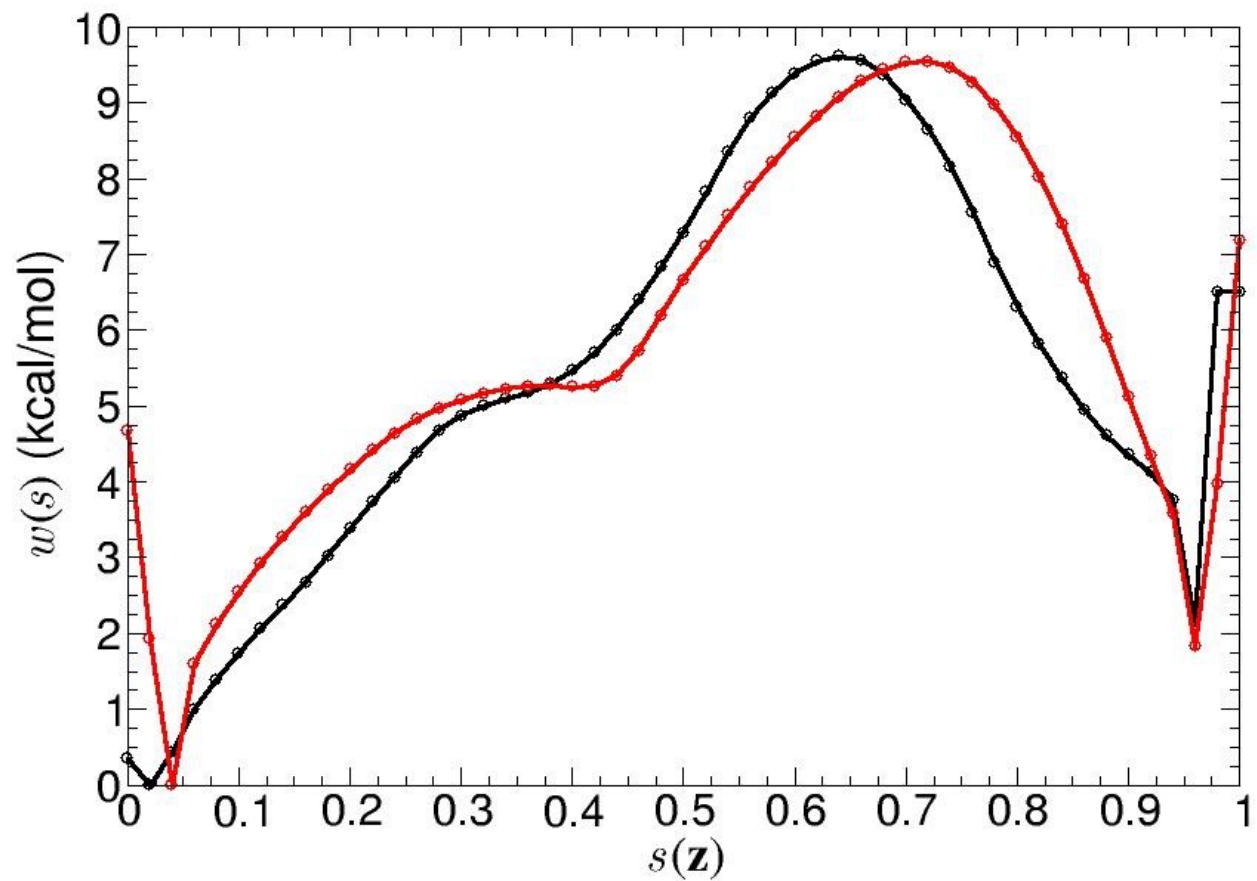
Figure 3.12: The PCV free energy calculations from two different strings. 1) Minimizing the local free energy of the $\phi - \psi$ PMF (black) and 2) the string method with swarms of trajectories (red).
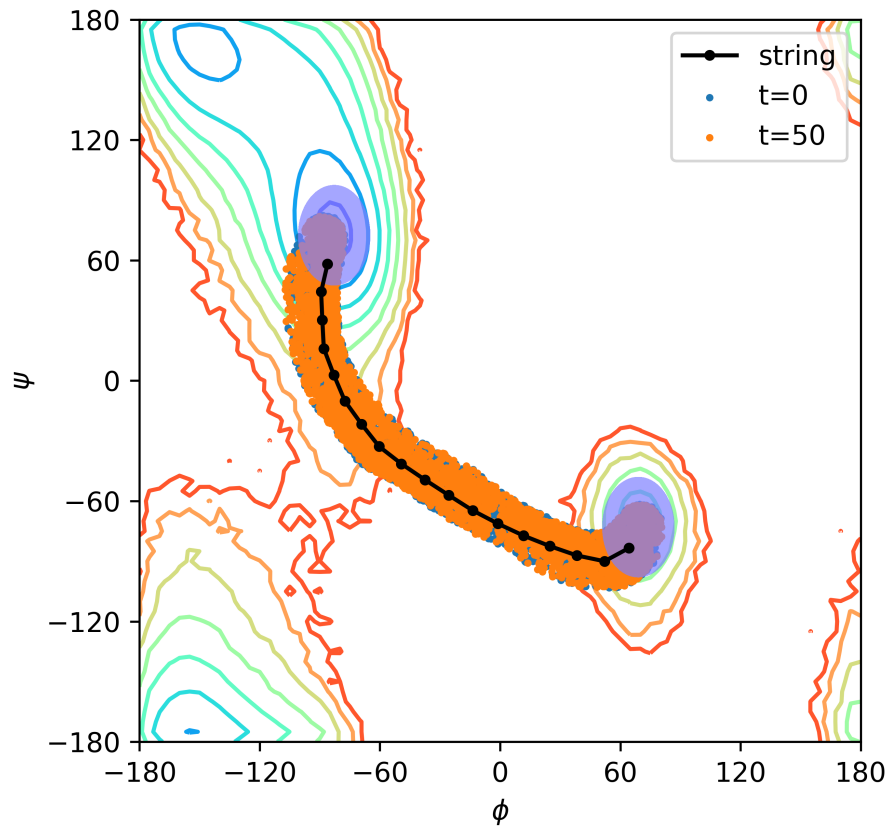
Figure 3.13: Reaction tube of 4000 trajectories with starting points generated by adaptive biasing force along the s. Blue dots are the starting positions of each trajectory, i.e., time t = 0. Orange dots are the positions at a later t = 50 steps. The purple ellipsoids are the boundary regions.
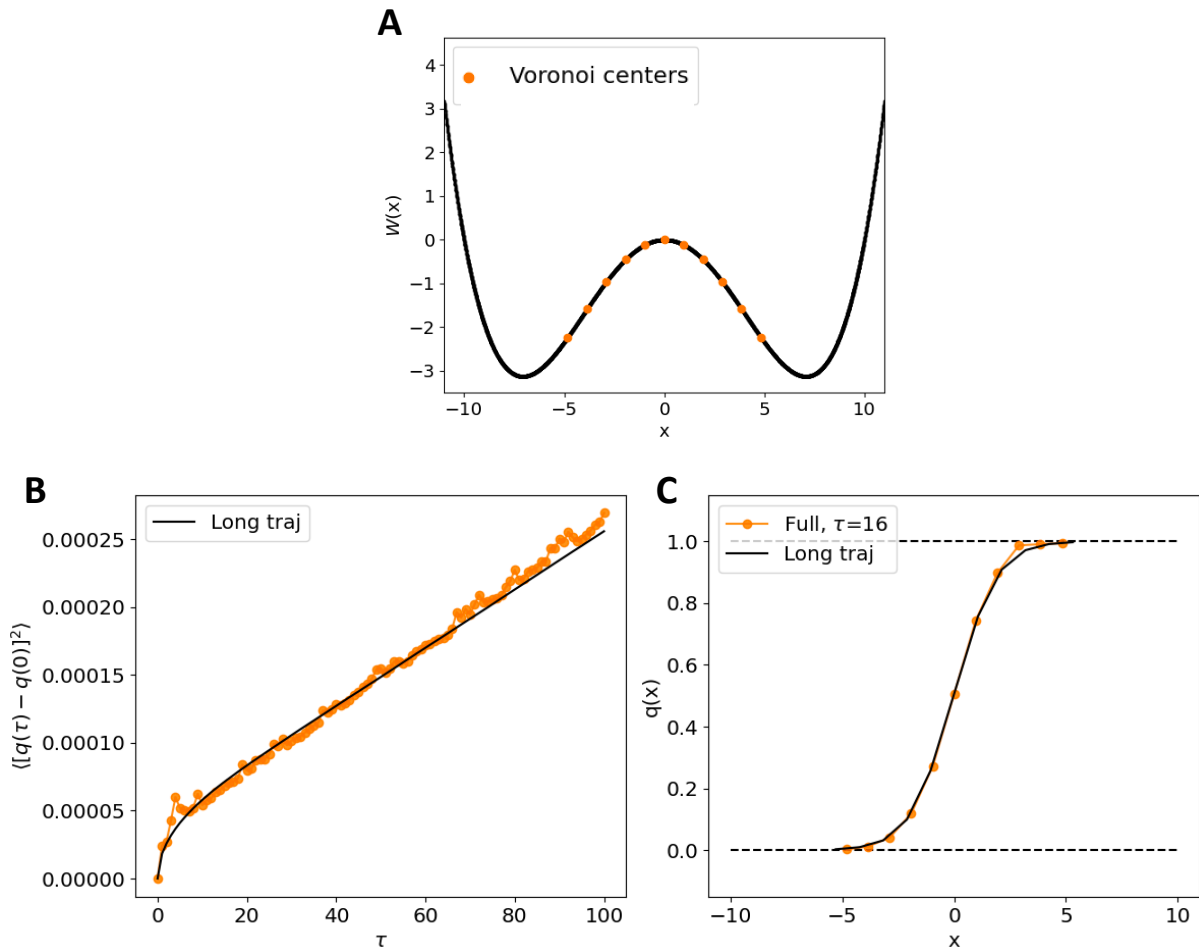
Figure 3.14: Fidelity check for the Boltzmann reweighting of the committor-correlation function with a 1-dimensional double well. (A) Double well potential in 1D. Between x = -11 and 11 at very small intervals of 0.005, many short unbiased trajectories were launched from each of the starting points. (B) The committor-correlation function committor and (C) the committor were computed by reweighting are shown in orange color. These results agree with the results for 1d example from a single long unbiased trajectory plotted in black.

Table 3.1: Comparison of the association and dissociation rates computed from MSM and the committor-consistent string method

Model	Lag time τ (ns)	k_{on} ($\times 10^{13}$ Å^3 s^{-1})	k_{off} ($\times 10^7$ s^{-1})
MSM-6D	12	2.31	2.73
MSM-2D	12	2.36	2.74
MSM-2D	15	2.20	2.53
String Method	0.1	12.63	18.24
	0.2	10.7	15.46
	0.3	9.75	14.08
	0.4	9.14	13.2
	0.5	8.66	12.51
	1	7.31	10.56
	2	6.07	8.77
	5	4.38	6.32
	7	3.73	5.39
	7.5	3.6	5.2
	9	3.27	4.72
	10	3.09	4.46
	12	2.77	4.0
	15	2.41	3.47
	20	1.97	2.85

[1] The k_{on} and k_{off} from the MSM with Perron-cluster cluster analysis (PCCA) analysis using a lag time τ of 12 ns with 6 order parameters were $2.31 \times 10^{13} Å^3 s^{-1}$ and $2.70 \times 10^7 s^{-1}$, respectively, as previously reported by He and Roux [122].
The k_{on} and k_{off} from the MSM/PCCA analysis with the same two order parameters studied in this paper (RMSD and COM) are $2.36 \times 10^{13} Å^3 s^{-1}$ and $2.74 \times 10^7 s^{-1}$, respectively, for a τ of 12 ns, and $2.20 \times 10^{13} Å^3 s^{-1}$ and $2.53 \times 10^7 s^{-1}$, respectively, for a τ of 15 ns.

CHAPTER 4

CONCLUDING REMARKS AND FUTURE OUTLOOK

Many of the critical transitions of interest in biomolecular systems take place on length-scales and timescales that are far beyond what can be attained with simple brute-force MD simulations. Consequently, in this dissertation, theoretical and computational strategies for Markov state models (MSMs) and a committor-consistent variational string method were developed and implemented to study dynamics more efficiently. In particular, a unifying theme of this dissertation is in the unique concern of being able to fully take advantage of biased simulations within these proposed frameworks.

In Chapter 2, MSMs were introduced as a powerful technique for the study of the natural dynamics of complex systems exhibiting multiple metastable states. Especially, being able to extract the kinetic and thermodynamic information from the MSMs and directly compare with experimental data makes MSMs particularly advantageous. The robustness of this MSM methodology was demonstrated by constructing and comparing various MSMs under different input parameters and simulation methods. Then, a sensitivity analysis was introduced into the MSM framework in order to pinpoint the microstates contributing the most error for the strategic addition of biased simulations in key sampling regions. This strategy maximizes the efficiency of constructing MSMs with biased simulations.

In Chapter 3, the main motivation of the study was the fact that, despite the various methods currently available for finding the most probable reaction pathway to connect metastable states, there still lacks a systematic approach stemmed fundamentally from the perspective of the committor probability, which has shown to provide information about the most kinetically optimal transition. Here, an extension of the string method was proposed based on a variational principle applied to the gradient of the committor. This approach allows the study of transitions between specific metastable states of interest and yields reaction pathways that are fundamentally of kinetic significance. Notably, this novel string

83

method is particularly useful for anisotropic systems, as demonstrated with the anisotropic diffusive cases in the Berezhkovskii-Szabo potential. Furthermore, this proposed framework was extended to allow the addition of biased simulations that are necessary in the study of larger, more complex systems with molecular processes that happen on long timescales.

A natural future direction for the MSM project is to extend the sensitivity analysis approach for biased MSMs to study all-atom proteins. For the case of the atomistic barstar-barnase, this complex is extremely "sticky" and spends a considerable amount of its lifetime bound, with an association rate of 1×10^{-1} s^{-1} and a dissociation rate of 4.8×10^{-5} to 5.0×10^{-4} s^{-1} reported by experimental studies [64, 135]. A previous computational study [51] of the all-atom barstar-barnase using brute-force MD and a hidden MSM analysis reported a large statistical uncertainty in the dissociation rate of 3×10^{-6} to 1×10^{-1} s^{-1}. While the hidden MSM in Ref. [51] was constructed from a very long simulation time of 1.7 milliseconds, the unbiased trajectory still saw very few unbinding events, hence the large uncertainty in the dissociation constant. Here, the sensitivity analysis in conjunction with biased simulations can be useful for characterizing the dissociation rate constant and reducing the computational overhead. As an illustrative example, Fig. 4.1 shows the sensitivity analysis estimated for the stationary distribution of a preliminary MSM using 4182 relevant contact pairwise distances. Relevant contacts were chosen based on degree of contact over the course of the milliseconds simulation, similar to the procedure discussed in Chapter 2. Of the 400 selected clusters plotted (out of 2000 total clusters), there are several clusters that have noticeably higher sensitivities. Then, one can initiate additional biased simulations at key regions that correspond to these highly sensitive clusters in order to improve the accuracy of the MSM. Figure 4.2 looks into selected relevant contacts mapped to each cluster and their computed sensitivities. We can see that the most sensitive clusters are the ones that have shorter contact distances corresponding to the loosely-bound transition states. The next steps would be to consider which collective variables (CVs) to bias along during

84
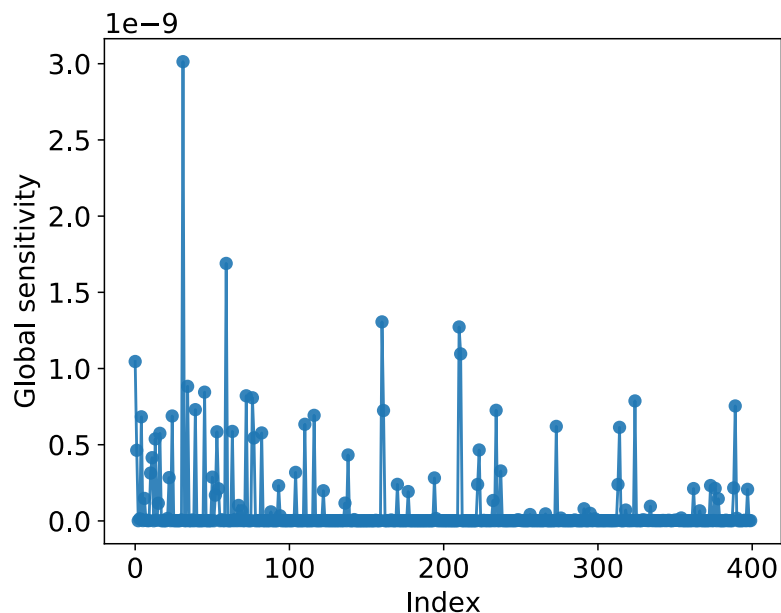
Figure 4.1: Global sensitivity computed for the stationary distribution of a preliminary MSM of the all-atom barnase-barstar complex using 4182 relevant contact pairwise distances. Of the 400 clusters shown (from 2000 clusters overall), several show noticeably higher sensitivities and correspond to the key regions to initiate additional biased simulations.
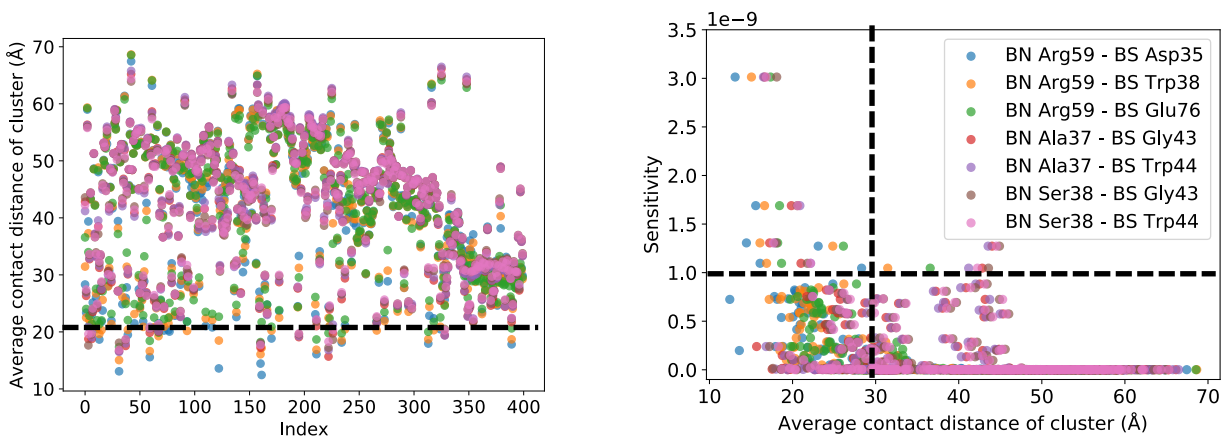
Figure 4.2: Pairwise contact distances per cluster and their sensitivities. MSM discretization distinguishes the clusters for the bound and unbound states (left), and the black dashed line indicates clusters near the intermediate states. Sensitivity analysis shows that the most sensitive microstates are have small contact distances and correspond to the loosely-bound transition states (right), with black dashed lines partitioning the clusters based on their sensitivities.

enhanced sampling simulations. In Chapter 2, we biased the coarse-grained complex along the center of mass distance between the proteins, but the all-atom system may require a more sophisticated set of CVs, e.g., including pairwise distances between key residues or minimum protein distances.

It is interesting to note that, while both MSMs and the committor-consistent variational string method have shown to be useful frameworks that produce consistent kinetic rates, one key advantage the proposed string method has over the MSM, excluding the fact of also being able to produce an optimal pathway, is that it is less likely to be influenced by undersampling and input parameters. Although MSMs can extract kinetic information from shorter pieces of trajectories compared to brute-force MD, an accurate MSM still requires fairly well-sampled simulations that may necessitate considerable computational overhead. The proposed string method algorithm, on the other hand, can work with much shorter pieces of trajectories for both unbiased and biased simulations to yield consistent results. Furthermore, a major issue for MSMs of complex, high-dimensional systems is in choosing an appropriate lag time that satisfies the Chapman-Kolmogorov equation [136], but the proposed string method is advantageous in that it generally does not assume Markovian dynamics.

Therefore, possible future direction for the committor-based string method is to extend the algorithm to higher dimensions. This direction would provide the advantage of incorporating a larger set of CVs relevant to the kinetic processes. For example, this extension would allow a more direct comparison of the barstar-barnase analyzed with two order parameters, discussed in Chapter 3, with the 6-dimensional MSM of barstar-barnase in Chapter 2. Here, machine learning techniques [130–133] have the potential to be especially useful for parameter selections, including choosing the best set of CVs, setting up an initial path, defining appropriate boundary regions, or even optimizing the multidimensional string itself. Figure 4.3 demonstrates a possible procedure using clustering and regression to optimize the
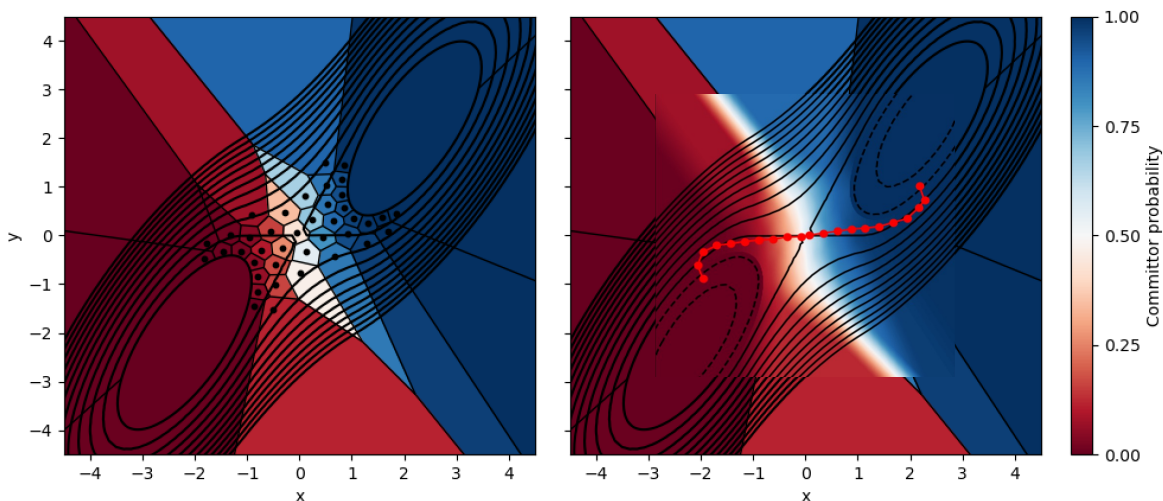
Figure 4.3: Machine learning techniques for the committor-consistent variational string method applied to higher dimensions. k-means clustering and Voronoi tessellation can be performed for a high-dimensional set of CVs, yielding a discrete committor probabilities for every Voronoi cell (left). k-nearest neighbor regression results in a smoother committor surface, from which a string path can be obtained by finite difference (right).

transition pathway. After choosing a set of CVs to study the transition, k-means clustering [70,71,137] can be performed to generate points on the CV space between the metastable states. We can then partition the space by Voronoi tessellation using the k-means centroids as the Voronoi centroids and compute discrete committor probabilities within each Voronoi cell. Then a k-nearest neighbor regression [138,139] can be implemented to produce a more continuous range of committor values. From there, a string pathway can be estimated by a finite difference to follow the gradient of the committor across the potential surface.

Another future direction for the proposed string method is for systems that exhibit more than two metastable states, as these cases are more representative of the properties of real molecules and biomolecules. For example, Figure 4.4 shows the Müller-Brown potential [140], which is a well-studied potential consisting of three long-lived states. If we start at the top left basin, an optimal string would be one that passes through the middle basin and end in the bottom right basin. Figure 4.5 shows the potential energy landscape of another three-

well model, where the coefficients are the ones originally reported by Metzner et al. [141]. This toy model also consists of three transition barriers but is a particularly interesting case for the proposed string method because the string would need to correctly predict which barrier to cross first when starting from a designated basin. Altogether, the proposed future directions are expected to greatly enhance the accuracy and range of systems that can be studied for the characterization of slow molecular processes.
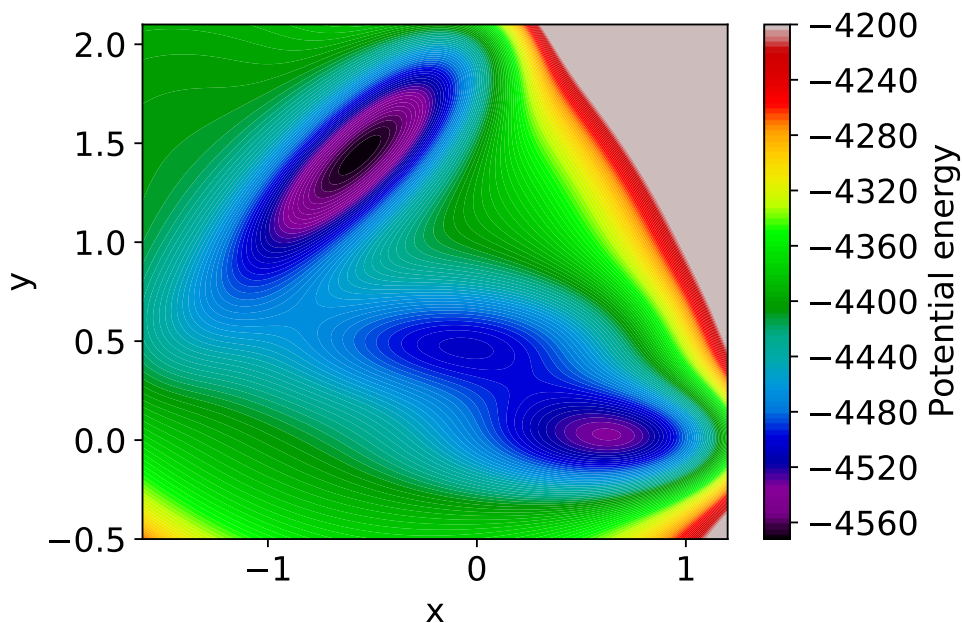
Figure 4.4: Potential energy landscape of the Müller-Brown potential in the (x, y) subspace.
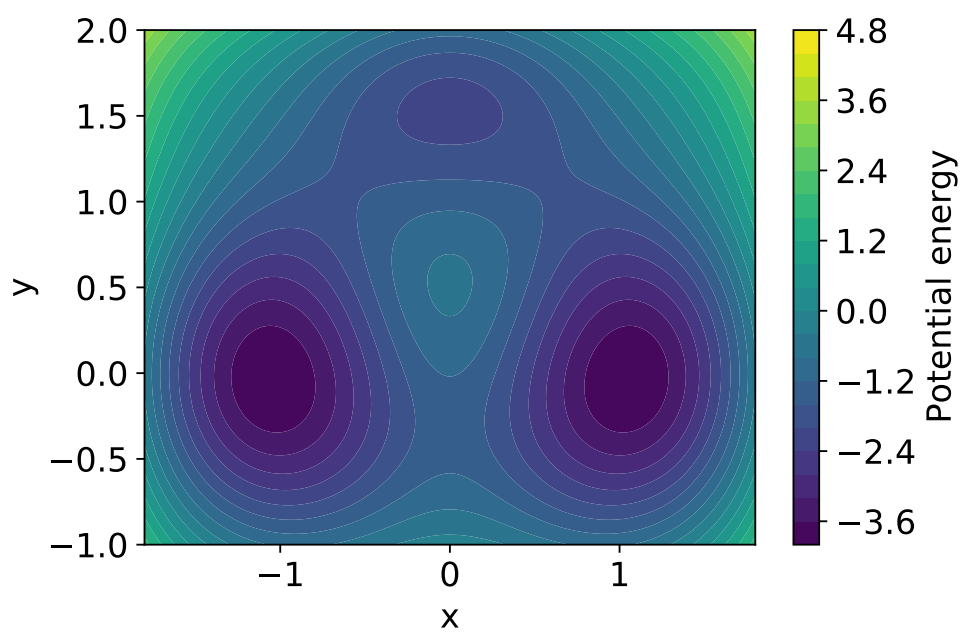
Figure 4.5: Potential energy landscape of a three well model in the (x, y) subspace.

REFERENCES

[1] Sidonia Mesentean, Sampath Koppole, Jeremy C Smith, and Stefan Fischer. The principal motions involved in the coupling mechanism of the recovery stroke of the myosin motor. *Journal of Molecular Biology*, 367(2):591–602, 2007.

[2] Marcus Jäger, Yan Zhang, Jan Bieschke, Houbi Nguyen, Maria Dendle, Marianne E Bowman, Joseph P Noel, Martin Gruebele, and Jeffery W Kelly. Structure–function–folding relationship in a WW domain. *Proceedings of the National Academy of Sciences*, 103(28):10648–10653, 2006.

[3] Andrei Yu Kobitski, Alexander Nierth, Mark Helm, Andres Jäschke, and G Ulrich Nienhaus. Mg2+-dependent folding of a diels-alderase ribozyme probed by single-molecule fret analysis. *Nucleic Acids Research*, 35(6):2047–2059, 2007.

[4] Andreas Ostermann, Robert Waschipky, Fritz G Parak, and G Ulrich Nienhaus. Ligand binding and conformational motions in myoglobin. *Nature*, 404(6774):205–208, 2000.

[5] David van der Spoel and Erik Lindahl. Brute-force molecular dynamics simulations of villin headpiece: comparison with nmr parameters. *Journal of Physical Chemistry B*, 107(40):11178–11187, 2003.

[6] Brad Van Oosten, Drew Marquardt, Ivana Komljenović, Jeremy P Bradshaw, Edward Sternin, and Thad A Harroun. Small molecule interaction with lipid bilayers: A molecular dynamics study of chlorhexidine. *Journal of Molecular Graphics and Modelling*, 48:96–104, 2014.

[7] Paweł Śledź and Amedeo Caflisch. Protein structure-based drug design: from docking to molecular dynamics. *Current Opinion in Structural Biology*, 48:93–102, 2018.

[8] Levi CT Pierce, Romelia Salomon-Ferrer, Cesar Augusto F. de Oliveira, J Andrew McCammon, and Ross C Walker. Routine access to millisecond time scale events with accelerated molecular dynamics. *Journal of Chemical Theory and Computation*, 8(9):2997–3002, 2012.

[9] Glenn M Torrie and John P Valleau. Nonphysical sampling distributions in monte carlo free-energy estimation: Umbrella sampling. *Journal of Computational Physics*, 23(2):187–199, 1977.

[10] Yuji Sugita and Yuko Okamoto. Replica-exchange molecular dynamics method for protein folding. *Chemical Physics Letters*, 314(1-2):141–151, 1999.

[11] Eric Darve and Andrew Pohorille. Calculating free energies using average force. *Journal of Chemical Physics*, 115(20):9169–9183, 2001.

[12] Eric Darve, David Rodríguez-Gómez, and Andrew Pohorille. Adaptive biasing force method for scalar and vector free energy calculations. *Journal of Chemical Physics*, 128(14):144120, 2008.

[13] Frank Noé, Illia Horenko, Christof Schütte, and Jeremy C Smith. Hierarchical analysis of conformational dynamics in biomolecules: Transition networks of metastable states. *Journal of Chemical Physics*, 126(15):04B617, 2007.

[14] Vijay S Pande, Kyle Beauchamp, and Gregory R Bowman. Everything you wanted to know about Markov state models but were afraid to ask. *Methods*, 52(1):99–105, 2010.

[15] Jan-Hendrik Prinz, Hao Wu, Marco Sarich, Bettina Keller, Martin Senne, Martin Held, John D Chodera, Christof Schütte, and Frank Noé. Markov models of molecular kinetics: Generation and validation. *Journal of Chemical Physics*, 134(17):174105, 2011.

[16] Brooke E Husic and Vijay S Pande. Markov state models: From an art to a science. *Journal of the American Chemical Society*, 140(7):2386–2396, 2018.

[17] Gregory R Bowman, Vijay S Pande, and Frank Noé. *An Introduction to Markov State Models and Their Application to Long Timescale Molecular Simulation*, volume 797. Springer Science & Business Media, 2013.

[18] Christoph Dellago, Peter G Bolhuis, Félix S Csajka, and David Chandler. Transition path sampling and the calculation of rate constants. *Journal of Chemical Physics*, 108(5):1964–1977, 1998.

[19] Peter G Bolhuis, David Chandler, Christoph Dellago, and Phillip L Geissler. Transition path sampling: Throwing ropes over rough mountain passes, in the dark. *Annual Review of Physical Chemistry*, 53:291–318, 2002.

[20] Titus S Van Erp, Daniele Moroni, and Peter G Bolhuis. A novel path sampling method for the calculation of rate constants. *Journal of Chemical Physics*, 118(17):7762–7774, 2003.

[21] Daniele Moroni, Peter G Bolhuis, and Titus S van Erp. Rate constants for diffusive processes by partial path sampling. *Journal of Chemical Physics*, 120(9):4055–4065, 2004.

[22] Gerhard Hummer. From transition paths to transition states and rate coefficients. *Journal of Chemical Physics*, 120(2):516–523, 2004.

[23] Eric Vanden-Eijnden. Towards a theory of transition paths. *Journal of Statistical Physics*, 123(3):503–523, 2006.

[24] Eric Vanden-Eijnden. Transition-path theory and path-finding algorithms for the study of rare events. *Annual Review of Physical Chemistry*, 61:391–420, 2010.

[25] Lars Onsager. Initial recombination of ions. *Physical Review*, 54(8):554, 1938.

[26] Alexander M Berezhkovskii and Attila Szabo. Committors, first-passage times, fluxes, markov states, milestones, and all that. *Journal of Chemical Physics*, 150(5):054106, 2019.

[27] Roberto Covino, Michael T Woodside, Gerhard Hummer, Attila Szabo, and Pilar Cossio. Molecular free energy profiles from force spectroscopy experiments by inversion of observed committors. *Journal of Chemical Physics*, 151(15):154115, 2019.

[28] Erik H Thiede, Dimitrios Giannakis, Aaron R Dinner, and Jonathan Weare. Galerkin approximation of dynamical quantities using trajectory data. *Journal of Chemical Physics*, 150(24):244111, 2019.

[29] John Strahan, Adam Antoszewski, Chatipat Lorpaiboon, Bodhi P Vani, Jonathan Weare, and Aaron R Dinner. Long-time-scale predictions from short-trajectory data: A benchmark analysis of the trp-cage miniprotein. *Journal of Chemical Theory and Computation*, 17(5):2948–2963, 2021.

[30] Benoît Roux. String Method with Swarms-of-Trajectories, Mean Drifts, Lag Time, and Committor. *Journal of Physical Chemistry A*, 125(34):7558–7571, 2021.

[31] Benoît Roux. Transition rate theory, spectral analysis, and reactive paths. *Journal of Chemical Physics*, 156(13):134111, 2022.

[32] Alexander Berezhkovskii, Gerhard Hummer, and Attila Szabo. Reactive flux and folding pathways in network models of coarse-grained protein dynamics. *Journal of Chemical Physics*, 130(20):205102, 2009.

[33] E Weinan, Weiqing Ren, and Eric Vanden-Eijnden. String method for the study of rare events. *Physical Review B*, 66(5):052301, 2002.

[34] E Weinan, Weiqing Ren, and Eric Vanden-Eijnden. Transition pathways in complex systems: Reaction coordinates, isocommittor surfaces, and transition tubes. *Chemical Physics Letters*, 413(1-3):242–247, 2005.

[35] E Weinan, Weiqing Ren, and Eric Vanden-Eijnden. Simplified and improved string method for computing the minimum energy paths in barrier-crossing events. *Journal of Chemical Physics*, 126(16):164103, 2007.

[36] Luca Maragliano, Alexander Fischer, Eric Vanden-Eijnden, and Giovanni Ciccotti. String method in collective variables: Minimum free energy paths and isocommittor surfaces. *Journal of Chemical Physics*, 125(2):024106, 2006.

[37] Albert C Pan, Deniz Sezer, and Benoît Roux. Finding transition pathways using the string method with swarms of trajectories. *Journal of Physical Chemistry B*, 112(11):3432–3440, 2008.

[38] Mikolai Fajer, Jérôme Hénin, Benoıt Roux, and Christophe Chipot. String method with swarms of trajectories: A tutorial for free-energy calculations along a minimum-action path. 2017.

[39] Alexander M Berezhkovskii and Attila Szabo. Diffusion along the splitting/commitment probability reaction coordinate. *Journal of Physical Chemistry B*, 117(42):13115–13119, 2013.

[40] William L Jorgensen. The many roles of computation in drug discovery. *Science*, 303(5665):1813–1818, 2004.

[41] Ozlem Keskin, Nurcan Tuncbag, and Attila Gursoy. Predicting protein–protein interactions from the molecular to the proteome level. *Chemical Reviews*, 116(8):4884–4909, 2016.

[42] Duncan E Scott, Andrew R Bayly, Chris Abell, and John Skidmore. Small molecules, big targets: drug discovery faces the protein–protein interaction challenge. *Nature Reviews Drug Discovery*, 15(8):533, 2016.

[43] Dong Guo, Thea Mulder-Krieger, Adriaan P IJzerman, and Laura H Heitman. Functional efficacy of adenosine A2A receptor agonists is positively correlated to their receptor residence time. *British Journal of Pharmacology*, 166(6):1846–1859, 2012.

[44] Alfonso Valencia and Florencio Pazos. Computational methods for the prediction of protein interactions. *Current Opinion in Structural Biology*, 12(3):368–373, 2002.

[45] Matthew P Harrigan, Mohammad M Sultan, Carlos X Hernández, Brooke E Husic, Peter Eastman, Christian R Schwantes, Kyle A Beauchamp, Robert T McGibbon, and Vijay S Pande. Msmbuilder: statistical models for biomolecular dynamics. *Biophysical Journal*, 112(1):10–15, 2017.

[46] Ignasi Buch, Toni Giorgino, and Gianni De Fabritiis. Complete reconstruction of an enzyme-inhibitor binding process by molecular dynamics simulations. *Proceedings of the National Academy of Sciences*, 108(25):10184–10189, 2011.

[47] Nuria Plattner and Frank Noé. Protein conformational plasticity and complex ligand-binding kinetics explored by atomistic simulations and markov models. *Nature Communications*, 6:7653, 2015.

[48] Stewart A Adcock and J Andrew McCammon. Molecular dynamics: survey of methods for simulating the activity of proteins. *Chemical Reviews*, 106(5):1589–1615, 2006.

[49] Guillermo Pérez-Hernández, Fabian Paul, Toni Giorgino, Gianni De Fabritiis, and Frank Noé. Identification of slow molecular order parameters for markov model construction. *Journal of Chemical Physics*, 139(1):015102, 2013.

[50] Christian R Schwantes and Vijay S Pande. Improvements in Markov state model construction reveal many non-native interactions in the folding of NTL9. *Journal of Chemical Theory and Computation*, 9(4):2000–2009, 2013.

[51] Nuria Plattner, Stefan Doerr, Gianni De Fabritiis, and Frank Noé. Complete protein–protein association kinetics in atomic detail revealed by molecular dynamics simulations and Markov modelling. *Nature Chemistry*, 9(10):1005, 2017.

[52] Albert C Pan, Daniel Jacobson, Konstantin Yatsenko, Duluxan Sritharan, Thomas M Weinreich, and David E Shaw. Atomic-level characterization of protein–protein association. *Proceedings of the National Academy of Sciences*, 116(10):4244–4249, 2019.

[53] Hao Wu, Fabian Paul, Christoph Wehmeyer, and Frank Noé. Multiensemble markov models of molecular thermodynamics and kinetics. *Proceedings of the National Academy of Sciences*, 113(23):E3221–E3230, 2016.

[54] Daniel P Loucks and Eelco van Beek. *System Sensitivity and Uncertainty Analysis*. Springer, 2017.

[55] Andrea Saltelli, Marco Ratto, Terry Andres, Francesca Campolongo, Jessica Cariboni, Debora Gatelli, Michaela Saisana, and Stefano Tarantola. *Global Sensitivity Analysis: The Primer*. John Wiley & Sons, 2008.

[56] Andrea Saltelli, Paola Annoni, Ivano Azzini, Francesca Campolongo, Marco Ratto, and Stefano Tarantola. Variance based sensitivity analysis of model output. Design and estimator for the total sensitivity index. *Computer Physics Communications*, 181(2):259–270, 2010.

[57] Ilya M Sobol. Sensitivity analysis for non-linear mathematical models. *Mathematical Modelling and Computational Experiment*, 1:407–414, 1993.

[58] Nina Singhal and Vijay S Pande. Error analysis and efficient sampling in Markovian state models for molecular dynamics. *Journal of Chemical Physics*, 123(20):204909, 2005.

[59] Gregory R Bowman, Kyle A Beauchamp, George Boxer, and Vijay S Pande. Progress and challenges in the automated construction of Markov state models for full protein systems. *Journal of Chemical Physics*, 131(12):124101, 2009.

[60] Jeffrey K Weber and Vijay S Pande. Characterization and rapid sampling of protein folding Markov state model topologies. *Journal of Chemical Theory and Computation*, 7(10):3405–3411, 2011.

[61] Ashley M Buckle, Gideon Schreiber, and Alan R Fersht. Protein-protein recognition: Crystal structural analysis of a barnase-barstar complex at 2.0-.ANG. resolution. *Biochemistry*, 33(30):8878–8889, 1994.

[62] Ronald D Hills and Charles L Brooks. Insights from coarse-grained Gō models for protein folding and dynamics. *International Journal of Molecular Sciences*, 10(3):889–905, 2009.

[63] Shoji Takada. Coarse-grained molecular simulations of large biomolecules. *Current Opinion in Structural Biology*, 22(2):130–137, 2012.

[64] Gideon Schreiber and Alan R Fersht. Interaction of barnase with its polypeptide inhibitor barstar studied by protein engineering. *Biochemistry*, 32(19):5145–5150, 1993.

[65] Sangwook Wu, Chang Jun Lee, and Lee G Pedersen. Analysis on long-range residue–residue communication using molecular dynamics. *Proteins: Structure, Function, and Bioinformatics*, 82(11):2896–2901, 2014.

[66] Hannah BL Jones, Stephen A Wells, Erica J Prentice, Anthony Kwok, Liyin L Liang, Vickery L Arcus, and Christopher R Pudney. A complete thermodynamic analysis of enzyme turnover links the free energy landscape to enzyme catalysis. *The FEBS Journal*, 284(17):2829–2842, 2017.

[67] James C Phillips, Rosemary Braun, Wei Wang, James Gumbart, Emad Tajkhorshid, Elizabeth Villa, Christophe Chipot, Robert D Skeel, Laxmikant Kale, and Klaus Schulten. Scalable molecular dynamics with NAMD. *Journal of Computational Chemistry*, 26(16):1781–1802, 2005.

[68] Bernard R Brooks, Charles L Brooks III, Alexander D Mackerell Jr, Lennart Nilsson, Robert J Petrella, Benoît Roux, Youngdo Won, Georgios Archontis, Christian Bartels, Stefan Boresch, et al. CHARMM: the biomolecular simulation program. *Journal of Computational Chemistry*, 30(10):1545–1614, 2009.

[69] William Humphrey, Andrew Dalke, and Klaus Schulten. VMD: Visual molecular dynamics. *Journal of Molecular Graphics*, 14:33–38, 1996.

[70] Hugo Steinhaus. Sur la division des corp materiels en parties. *Bulletin of the Polish Academy of Sciences*, 1(804):801, 1956.

[71] James MacQueen. Some methods for classification and analysis of multivariate observations. In *Proceedings of the Fifth Berkeley Symposium on Mathematical Statistics and Probability*, volume 1, pages 281–297. Oakland, CA, USA, 1967.

[72] Robert L Thorndike. Who belongs in the family? *Psychometrika*, 18(4):267–276, 1953.

[73] Robert T McGibbon, Kyle A Beauchamp, Matthew P Harrigan, Christoph Klein, Jason M Swails, Carlos X Hernández, Christian R Schwantes, Lee-Ping Wang, Thomas J Lane, and Vijay S Pande. MDTraj: A modern open library for the analysis of molecular dynamics trajectories. *Biophysical Journal*, 109(8):1528–1532, 2015.

[74] Martin K Scherer, Benjamin Trendelkamp-Schroer, Fabian Paul, Guillermo Pérez-Hernández, Moritz Hoffmann, Nuria Plattner, Christoph Wehmeyer, Jan-Hendrik Prinz, and Frank Noé. PyEMMA 2: A software package for estimation, validation, and analysis of Markov models. *Journal of Chemical Theory and Computation*, 11(11):5525–5542, 2015.

[75] John D. Hunter. Matplotlib: A 2D graphics environment. *Computing in Science & Engineering*, 9(3):90–95, 2007.

[76] Robert T McGibbon and Vijay S Pande. Variational cross-validation of slow dynamical modes in molecular kinetics. *Journal of Chemical Physics*, 142(12):124105, 2015.

[77] Brooke E Husic, Robert T McGibbon, Mohammad M Sultan, and Vijay S Pande. Optimized parameter selection reveals trends in Markov state models for protein folding. *Journal of Chemical Physics*, 145(19):194103, 2016.

[78] Chuankai Zhao and Diwakar Shukla. Structural basis for negative regulation of ABA signaling by ROP11 GTPase. *bioRxiv*, 2020.

[79] Derya Meral, Davide Provasi, Diego Prada-Gracia, Jan Möller, Kristen Marino, Martin J Lohse, and Marta Filizola. Molecular details of dimerization kinetics reveal negligible populations of transient μ-opioid receptor homodimers at physiological concentrations. *Scientific Reports*, 8(1):7705, 2018.

[80] Christoph Wehmeyer, Martin K Scherer, Tim Hempel, Brooke E Husic, Simon Olsson, and Frank Noé. Introduction to Markov state modeling with the PyEMMA software–v1.0. *LiveCoMS*, 1(1):1–12, 2018.

[81] Hao Wu and Frank Noé. Variational approach for learning Markov processes from time series data. *Journal of Nonlinear Science*, 30(1):23–66, 2020.

[82] Ling Wang, Shirley WI Siu, Wei Gu, and Volkhard Helms. Downhill binding energy surface of the barnase–barstar complex. *Biopolymers*, 93(11):977–985, 2010.

[83] Susanna Röblitz and Marcus Weber. Fuzzy spectral clustering by PCCA+: Application to Markov state models and data classification. *Advances in Data Analysis and Classification*, 7(2):147–179, 2013.

[84] Frank Noé, Hao Wu, Jan-Hendrik Prinz, and Nuria Plattner. Projected and hidden Markov models for calculating kinetics and metastable states of complex molecules. *Journal of Chemical Physics*, 139(18):184114, 2013.

[85] Ilya M Sobol. Global sensitivity indices for nonlinear mathematical models and their Monte Carlo estimates. *Mathematics and Computers in Simulation*, 55(1-3):271–280, 2001.

[86] William George Noid. Perspective: Coarse-grained models for biomolecular systems. *Journal of Chemical Physics*, 139(9):090901, 2013.

[87] Marc Baaden and Siewert J Marrink. Coarse-grain modelling of protein–protein interactions. *Current Opinion in Structural Biology*, 23(6):878–886, 2013.

[88] Marissa G Saunders and Gregory A Voth. Coarse-graining methods for computational biology. *Annual Review of Biophysics*, 42:73–93, 2013.

[89] Yuji Sugita and Yuko Okamoto. Replica-exchange multicanonical algorithm and multicanonical replica-exchange method for simulating systems with rough energy landscape. *Chemical Physics Letters*, 329(3-4):261–270, 2000.

[90] Fabian Paul, Christoph Wehmeyer, Esam T Abualrous, Hao Wu, Michael D Crabtree, Johannes Schöneberg, Jane Clarke, Christian Freund, Thomas R Weikl, and Frank Noé. Protein-peptide association kinetics beyond the seconds timescale from atomistic simulations. *Nature Communications*, 8(1):1095, 2017.

[91] Stephen K. Burley, Charmi Bhikadiya, Chunxiao Bi, Sebastian Bittrich, Li Chen, Gregg V. Crichlow, Jose M. Duarte, Shuchismita Dutta, Maryam Fayazi, Zukang Feng, Justin W. Flatt, Sai J. Ganesan, David S. Goodsell, Sutapa Ghosh, Rachel Kramer Green, Vladimir Guranovic, Jeremy Henry, Brian P. Hudson, Catherine L. Lawson, Yuhe Liang, Robert Lowe, Ezra Peisach, Irina Persikova, Dennis W. Piehl, Yana Rose, Andrej Sali, Joan Segura, Monica Sekharan, Chenghua Shao, Brinda Vallat, Maria Voigt, John D. Westbrook, Shamara Whetstone, Jasmine Y. Young, and Christine Zardecki. RCSB Protein Data Bank: Celebrating 50 years of the PDB with new tools for understanding and visualizing biological macromolecules in 3D. *Protein Science*, 31(1):187–208, 2022.

[92] Bryan A Krantz, Robin S Dothager, and Tobin R Sosnick. Discerning the structure and energy of multiple transition states in protein folding using ψ-analysis. *Journal of Molecular Biology*, 337(2):463–475, 2004.

[93] Jérôme J Lacroix, Stephan A Pless, Luca Maragliano, Fabiana V Campos, Jason D Galpin, Christopher A Ahern, Benoît Roux, and Francisco Bezanilla. Intermediate state trapping of a voltage sensor. *Journal of General Physiology*, 140(6):635–652, 2012.

[94] Diwakar Shukla, Yilin Meng, Benoît Roux, and Vijay S Pande. Activation pathway of src kinase reveals intermediate states as targets for drug design. *Nature communications*, 5(1):1–11, 2014.

[95] R Elber and M Karplus. A method for determining reaction paths in large molecules: Application to myoglobin. *Chemical Physics Letters*, 139(5):375–380, 1987.

[96] Stefan Fischer and Martin Karplus. Conjugate peak refinement: An algorithm for finding reaction paths and accurate transition states in systems with many degrees of freedom. *Chemical Physics Letters*, 194(3):252–261, 1992.

[97] J. Schlitter, M. Engels, P. Krüger, E. Jacoby, and A. Wollmer. Targeted molecular dynamics simulation of conformational change-Application to the T ↔ R transition in insulin. *Molecular Simulation*, 10:291, 1993.

[98] Hannes Jónsson, Greg Mills, and Karsten W Jacobsen. *Nudged Elastic Band Method for Finding Minimum Energy Paths of Transitions*, chapter 16, page 385. Classical and Quantum Dynamics in Condensed Phase Simulations. World Scientific, Singapore, 1998.

[99] Barry Isralewitz, Mu Gao, and Klaus Schulten. Steered molecular dynamics and mechanical functions of proteins. *Current Opinion in Structural Biology*, 11:224, 2001.

[100] Baron Peters and Bernhardt L Trout. Obtaining reaction coordinates by likelihood maximization. *Journal of Chemical Physics*, 125(5):054108, 2006.

[101] Davide Branduardi, Francesco Luigi Gervasio, and Michele Parrinello. From A to B in free energy space. *Journal of Chemical Physics*, 126(5):054103, 2007.

[102] Arjan van der Vaart and Martin Karplus. Minimum free energy pathways and free energy profiles for conformational transitions based on atomistic molecular dynamics simulations. *Journal of Chemical Physics*, 126:164106, 2007.

[103] Haijun Yang, Hao Wu, Dawei Li, Li Han, and Shuanghong Huo. Temperature-dependent probabilistic roadmap algorithm for calculating variationally optimized conformational transition pathways. *Journal of Chemical Theory and Computation*, 3:17, 2007.

[104] Thomas F. Miller and Cristian Predescu. Sampling diffusive transition paths. *Journal of Chemical Physics*, 126(14):144102, 2007.

[105] Wolfgang Lechner, Jutta Rogal, Jarek Juraszek, Bernd Ensing, and Peter G Bolhuis. Nonlinear reaction coordinate analysis in the reweighted path ensemble. *Journal of Chemical Physics*, 133(17):174110, 2010.

[106] Alexander Berezhkovskii and Attila Szabo. One-dimensional reaction coordinates for diffusive activated rate processes in many dimensions. *Journal of Chemical Physics*, 122(1):14503, 2005.

[107] Sergei V. Krivov. On Reaction Coordinate Optimality. *Journal of Chemical Theory and Computation*, 9(1):135–146, 2013.

[108] Polina V. Banushkina and Sergei V. Krivov. Nonparametric variational optimization of reaction coordinates. *Journal of Chemical Physics*, 143(18), 2015.

[109] Kei-ichi Okazaki, David Wöhlert, Judith Warnau, Hendrik Jung, Özkan Yildiz, Werner Kühlbrandt, and Gerhard Hummer. Mechanism of the electroneutral sodium/proton antiporter PaNhaP from transition-path shooting. *Nature Communications*, 10(1):1742, 2019.

[110] Pratyush Tiwary and BJ Berne. Spectral gap optimization of order parameters for sampling complex molecular systems. *Proceedings of the National Academy of Sciences*, 113(11):2839–2844, 2016.

[111] Zachary Smith, Debabrata Pramanik, Sun-Ting Tsai, and Pratyush Tiwary. Multi-dimensional spectral gap optimization of order parameters (SGOOP) through conditional probability factorization. *Journal of Chemical Physics*, 149(23):234105, 2018.

[112] Wei Chen and Andrew L Ferguson. Molecular enhanced sampling with autoencoders: On-the-fly collective variable discovery and accelerated free energy landscape exploration. *Journal of Computational Chemistry*, 39(25):2079–2102, 2018.

[113] Luigi Bonati, Yue-Yu Zhang, and Michele Parrinello. Neural networks-based variationally enhanced sampling. *Proceedings of the National Academy of Sciences*, 116(36):17641–17647, 2019.

[114] Sun-Ting Tsai, En-Jui Kuo, and Pratyush Tiwary. Learning molecular dynamics with simple language model built upon long short-term memory neural network. *Nature Communications*, 11(1):5115, 2020.

[115] Luigi Bonati, GiovanniMaria Piccini, and Michele Parrinello. Deep learning the slow modes for rare events sampling. *Proceedings of the National Academy of Sciences*, 118(44), 2021.

[116] Shashank Pant, Zachary Smith, Yihang Wang, Emad Tajkhorshid, and Pratyush Tiwary. Confronting pitfalls of AI-augmented molecular dynamics using statistical physics. *Journal of Chemical Physics*, 153(23):234118, 2020.

[117] Sun-Ting Tsai, Zachary Smith, and Pratyush Tiwary. SGOOP-d: Estimating Kinetic Distances and Reaction Coordinate Dimensionality for Rare Event Systems from Biased/Unbiased Simulations. *Journal of Chemical Theory and Computation*, 17(11):6757–6765, 2021.

[118] Eric Vanden-Eijnden. *Transition path theory*, volume 2 of *Computer Simulations in Condensed Matter: From Materials to Chemical Biology*, page 439. Springer, 2006.

[119] Grisell Díaz Leines and Bernd Ensing. Path finding on high-dimensional free energy landscapes. *Physical Review Letters*, 109(2):020601, 2012.

[120] Ladislav Hovan, Federico Comitani, and Francesco L Gervasio. Defining an optimal metric for the path collective variables. *Journal of Chemical Theory and Computation*, 15(1):25–32, 2018.

[121] Pratyush Tiwary and BJ Berne. Predicting reaction coordinates in energy landscapes with diffusion anisotropy. *Journal of Chemical Physics*, 147(15):152701, Oct 2017.

[122] Ziwei He, Fabian Paul, and Benoît Roux. A critical perspective on Markov state model treatments of protein-protein association using coarse-grained simulations. *Journal of Chemical Physics*, 154(8):084101, Feb 2021.

[123] Wenjin Li and Ao Ma. Recent developments in methods for identifying reaction coordinates. *Molecular Simulation*, 40(10-11):784–793, 2014.

[124] James S Langer. Statistical theory of the decay of metastable states. *Annals of Physics*, 54(2):258–275, 1969.

[125] Baron Peters, Peter G. Bolhuis, Ryan G. Mullen, and Joan-Emma Shea. Reaction coordinates, one-dimensional Smoluchowski equations, and a test for dynamical self-consistency. *Journal of Chemical Physics*, 138(5), 2013.

[126] Baron Peters. Reaction coordinates and mechanistic hypothesis tests. *Annual Review of Physical Chemistry*, 67:669–690, 2016.

[127] Ao Ma and Aaron R Dinner. Automatic method for identifying reaction coordinates in complex systems. *The Journal of Physical Chemistry B*, 109(14):6769–6779, 2005.

[128] Ao Ma, Ambarish Nag, and Aaron R Dinner. Dynamic coupling between coordinates in a model for biomolecular isomerization. *Journal of Chemical Physics*, 124(14):144911, 2006.

[129] Jie Hu, Ao Ma, and Aaron R Dinner. A two-step nucleotide-flipping mechanism enables kinetic discrimination of dna lesions by agt. *Proceedings of the National Academy of Sciences*, 105(12):4615–4620, 2008.

[130] Christopher M Bishop. Information science and statistics. *Pattern Recognition and Machine Learning. Springer*, 2006.

[131] Mary A Rohrdanz, Wenwei Zheng, and Cecilia Clementi. Discovering mountain passes via torchlight: Methods for the definition of reaction coordinates and pathways in complex macromolecular reactions. *Annual Review of Physical Chemistry*, 64:295–316, 2013.

[132] Hendrik Jung, Roberto Covino, and Gerhard Hummer. Artificial intelligence assists discovery of reaction coordinates and mechanisms from molecular dynamics simulations. *arXiv preprint:1901.04595*, 2019.

[133] Hythem Sidky, Wei Chen, and Andrew L Ferguson. Machine learning for collective variable discovery and enhanced sampling in biomolecular simulation. *Molecular Physics*, 118(5):e1737742, 2020.

[134] Ruijun Zhao, Juanfang Shen, and Robert D Skeel. Maximum flux transition paths of conformational change. *Journal of Chemical Theory and Computation*, 6(8):2411–2423, 2010.

[135] Gideon Schreiber and Alan R Fersht. Energetics of protein-protein interactions: Analysis of the barnase-barstar interface by single mutations and double mutant cycles. *Journal of Molecular Biology*, 248(2):478–486, 1995.

[136] Ernesto Suárez, Rafal P Wiewiora, Chris Wehmeyer, Frank Noé, John D Chodera, and Daniel M Zuckerman. What Markov state models can and cannot do: Correlation versus path-based observables in protein-folding models. *Journal of Chemical Theory and Computation*, 17(5):3119–3133, 2021.

[137] Stuart Lloyd. Least squares quantization in PCM. *IEEE Transactions on Information Theory*, 28(2):129–137, 1982.

[138] Evelyn Fix and Joseph Lawson Hodges. Discriminatory analysis. nonparametric discrimination: Consistency properties. *International Statistical Review/Revue Internationale de Statistique*, 57(3):238–247, 1989.

[139] Naomi S Altman. An introduction to kernel and nearest-neighbor nonparametric regression. *The American Statistician*, 46(3):175–185, 1992.

[140] Klaus Müller and Leo D Brown. Location of saddle points and minimum energy paths by a constrained simplex optimization procedure. *Theoretica Chimica Acta*, 53(1):75–93, 1979.

[141] Philipp Metzner, Christof Schütte, and Eric Vanden-Eijnden. Illustration of transition path theory on a collection of simple examples. *Journal of Chemical Physics*, 125(8):084110, 2006.